Laser-Directed Self-Organization and Reaction Control in Complex Systems

Kumulative Dissertation

Zur Erlangung des Doktorgrades der Naturwissenschaften

(Dr. rer. nat.)

dem

Fachbereich Chemie

der Philipps-Universität Marburg

vorgelegt von

Hendrik Martin Reinhardt

aus

Dresden

Marburg an der Lahn, 2013

The Mystery of Life isn't a

Problem to Solve but a

Reality to Experience.

Frank Herbert

Contents

1   Motivation

In an isolated system the entropy can only increase. This sentence, stating the second law of thermodynamics, appears to be in contradiction with empirical observations of living systems in which individual building blocks arrange spontaneously into patterns. The second law of thermodynamics is a statistical rule and thus not excluding local decreases of entropy as long as the total entropy in a system increases. By the fact that living systems resemble only a minor part of the total system, they do not violate this law directly; however, they twist probability with a conspicuous regularity that raises profound questions. The mystery of life is a subject that has piqued human curiosity since time immemorial. Inspired by the concept of nature to create complex and highly ordered systems with outmost efficiency, precision and speed, scientists around the world are seeking to understand this power of creation. At the present state of knowledge, two phenomena appear to be of fundamental importance. *Self-assembly* describes a process of pattern formation that can be observed in all organisms. It proceeds under near-equilibrium conditions and is essentially driven by the strive for a more favorable state of energy. In contrast to this, *self-organization* is a non-equilibrium process that is triggered by a certain type of stimulus. While *self-assembly* is well-understood, the principles behind *self-organization* remain nebulous. The reason for this is the ubiquity of self-organization across systems and dimensional scales. Attempts at a structured investigation of this phenomenon are further impeded by its unmanageable flexibility in pattern formation. Confronted with such overwhelming complexity, a debate arose about the question whether *self-organization* is to be classified as a universal principle at all. The issue at hand demands particular attention since latest results indicate that pattern formation in living systems is not entirely based on *self-assembly*. Richard Jones, the author of *Soft Machines,* summarized the present level of knowledge commenting: *"Viruses self-assemble, but elephants (perhaps) self-organise."* Considering this situation, the need for research in the field of *self-organization* becomes obvious. Improved understanding of the phenomenon is definitely not only of academic interest. Against the background of limited raw materials and energy resources on earth, sustainable technologies for production and

regeneration become increasingly important. Human technology is characterized by a one-directional flow of resources from being concentrated to becoming dispersed. In contrast to that, the concept of nature is cyclic processing with utmost efficiency and sustainability. The ever-increasing exploitation of recourses on earth and its ominous side effects induce a pressing need for change whilst currently lacking technological alternatives. To this end, the most reasonable approach to meet this challenge is to learn from nature.

This study is concerned with the possibility to imitate nature's low-effort-high-outcome-principle of pattern formation in complex systems. The term *complex* refers to any system that incorporates a multitude of entities in various states of energy and order. Especially organisms are encompassed by this definition but also nearly all materials that surround us. When a complex system is stimulated, this provokes a scenario of reactions, which proceeds under boundary conditions defined by the degrees of freedom of the system and the type of stimulus. Due to the fact that complexity is inherent to the system, nature's power of creation is thought to be the result of perfect stimulus control. In order to comply with this, lasers were utilized to trigger specific reorganizations in complex systems. Their potential to create stimuli that impart energy, timing and patterns makes lasers ideal tools for studies on self-organization. Chapter 2 provides specific information about the benefits of lasers for stimulus design and elucidates the physical backgrounds of laser-induced self-organization phenomena that form the basis of this study. Compared to the state of the art in this field of research, the novelty of the thesis is characterized by the investigation of self-organization processes that lead to pattern formation in complex systems. An overview of the results is presented in chapter 3. Detailed information is provided in publications that accompany this thesis.

Key questions of this investigation are:

1   Is it generally possible to imitate nature's low-effort-high-outcome-principle of pattern formation in complex systems?

2   Are laser-stimulated transformations in complex systems predictable and controllable thus giving the opportunity to fabricate materials by design?

3   Can functional materials be created following nature's example?

2   Laser-directed Self-Organization and Pattern Formation

Compared to the 20th century, in which the electron stood in the focus of science and technology, the 21th century is the age of the photon. Light has always inspired human imagination and features a radiant fascination. The crucial basis that eventually enabled modern light technologies was established by Albert Einstein already in 1917. However, his theory of *spontaneous emission* was perceived to be a more hypothetical than probable paradigm of theoretical physics at that time. For this reason about 40 years passed until Gordon, Zeiger and Townes adopted his fundamental idea to build a device that emitted electromagnetic waves in a frequency range not accessible up to this point. Due to its generation principle of *microwave amplification by stimulated emission of radiation* it was given the name *maser*. Convinced of this concept, Schawlow und Townes explored the possibilities to expand the emission spectrum of such a device into the visual range. Finally, in 1960 Maiman succeeded with the first demonstration of *light amplification by stimulated emission of radiation* – the *laser* was born. This was the starting point of a turbulent era of innovations that improves our capabilities to control photons consistently. The first continuously emitting device, the helium-neon laser, found its way into a wide variety of scientific, technical and medical applications. Lasers based on gaseous media are constantly in use. Prominent examples include the CO_2 laser, which is typically found in processes like welding or cutting, and the excimer laser whose primary fields of application are photolithography and micromachining of materials. The growing demand for adjustable laser wavelengths led to the development of the dye lasers at the end of the 1980s. This accomplishment provided access to laser-spectroscopy, which in turn promoted rapid advances in fields like elementary physics, physical chemistry and chemical analytics. In the same decade just another novel laser concept was introduced that should ascend to the most popular and widely applied laser types. The solid-state laser, which uses crystals for light amplification was the first laser that met the demands for high robustness and low cost of operation. Especially active laser media like Nd:YAG and Nd:YVO$_4$ are enjoying great popularity up until now. Advanced solid-state media such as titanium-sapphire crystals built the basis for a laser technology that covers an ever wider spectrum of applications. The high gain bandwidth

of titanium-sapphire crystals opened the opportunity to generate ultra short and highly intense laser pulses, which is the reason this laser type is commonly referred to as femtosecond laser. It introduced time-dependent spectroscopy, thus enabling us to investigate rapidly progressing reactions and processes. In addition to this, femtosecond lasers increased the speed of world-wide communication networks tremendously and set new standards in material processing, time measurement, reaction control and medicine. Due to the short time span and high intensity of their pulses tightly focused femtosecond lasers are able to subject materials to conditions that are similar to those in the center of stars. Still, these lasers can be controlled with such precision that even eye surgery belongs to their repertoire of applications. Compared to other technologies, the *domestication of light* advanced to an unparalleled level of power and control. This combination provides a comprehensive basis for the investigation on self-organization phenomena since those depend largely on the type of stimulus applied to a system. The application of lasers provides the advantage to trigger selective reorganizations thus directing self-organization into utile channels. Figure 2.1 outlines available parameters.
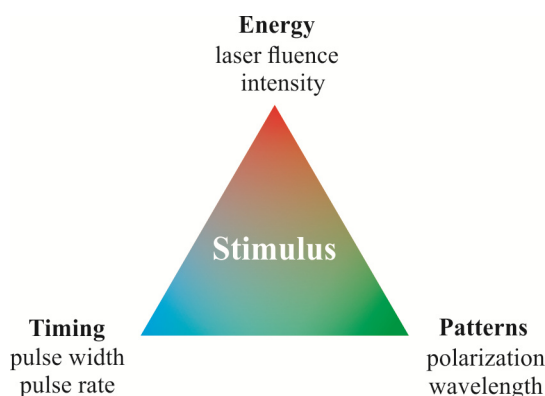
Fig. 2.1: The nature of light.
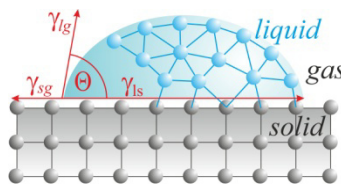
Energy is a parameter that is characterized by the laser fluence, a measure for energy input per unit area into a system. It is correlated to the timing parameter via pulse variables that control the duration and recurrence of this event. The feature that most distinguishes lasers from conventional techniques for reaction control is their capability to impart patterns into a system. This gives the opportunity to trigger site-specific self-organization – a concept that was found to be very prolific when applied to complex systems. Detailed information concerning phenomena that were utilized to trigger self-organization in the systems under investigation are provides in the chapters 2.1 - 2.6.

2.1   Pulsed Laser-induced Dewetting (PLiD)

Pulsed laser-induced dewetting (PLiD) is an emerging technique that facilitates nanostructure formation starting from solid materials. The self-organization process is distinctive in its precision, flexibility, and sustainability thus representing a promising concept of modern nanotechnology. As the name suggests, PLiD is based on dewetting, a phenomenon that is manifested in the tendency of liquid thin films to break up into droplets. The fundamental reason for this behavior is the striving of liquid thin films for a more favorable state of energy. The phenomenon of dewetting is strongly connected with wettability, a complex quantity that describes the interaction between solids and liquids. Wettability belongs to the well-investigated phenomena since it affects numerous aspects in everyday life and technology. Even more importantly it forms the basis of essential processes in living systems. For example, biological processes like liquid transport, separation and nutrient uptake are based on hydrophilic interactions whereas hydrophobic interactions are crucial for protein folding and formation of lipid bilayers to only name a few. Improved knowledge about liquid-solid interactions resulted in the perception that wettability is a universal principle and thus expandable to arbitrary systems. A general approach for the determination of interactions between liquid and solid media was introduced by Thomas Young already in 1805.

Fig. 2.1.1: Young`s equation and schematic illustration of wetting.

Young's equation takes cohesive and adhesive forces into account to determine the contact angle between a liquid and a solid under consideration of respective surface energies. If the surface energies of the involved media are accurately known, the equation returns reliable predictions. Unfortunately, Young's approach is limited to macroscopic interactions, which is the reason its application for the prediction of PLiD is prohibited. This can be explained by the fact that nanostructures feature much larger

specific surface areas compared to macrostructures. As a consequence, interfacial effects have a considerably stronger influence on the outcome of PLiD-stimulated nanostructure formation processes that must be accounted for with a specialized theory. The predictability of PLiD is further complicated by the fact that the process is characterized by a very fast and nonlinear progressing scenario of surface liquefaction, dewetting and resolidification. Figure 2.1.2 illustrates the PLiD process schematically.
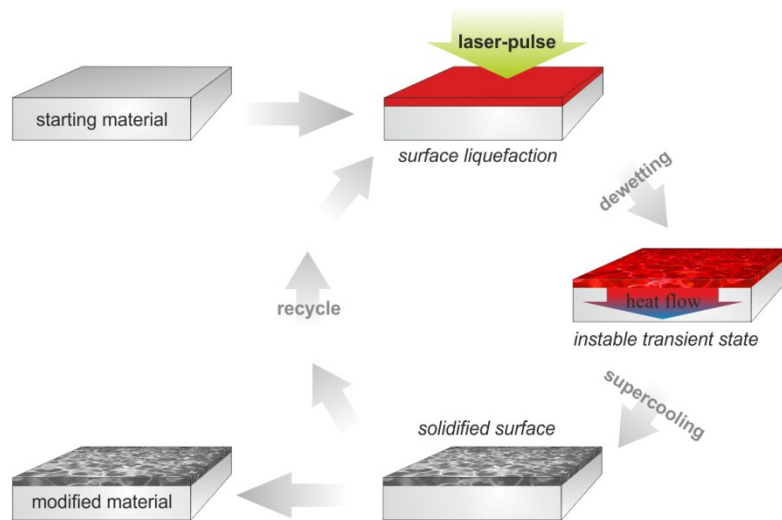
Fig. 2.1.2: Schematic illustration of the PLiD process.

PLiD is initiated by intense photo-thermal heating, which liquefies the outmost surface of a solid almost instantaneously. Due to intrinsic instability, liquid thin films encounter competing energy loss mechanisms that induce surface oscillations and rupture. Depending on the number of PLiD cycles applied to a material, this initially leads to the formation of holes, which then expand to a reticular intermediate that finally breaks up into nanoparticles. Fig. 2.1.3 visualizes this scenario as it is typically observed.
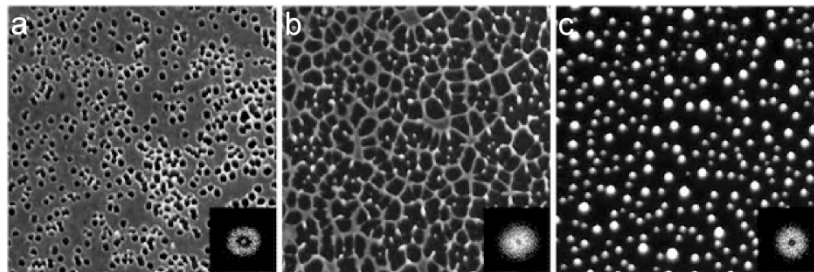
Fig. 2.1.3: Silver thin film subjected to increasing numbers of dewetting cycles.[1]
(a) formation of holes, (b) reticular intermediate, (c) break up into particles

2.2 Theoretical Background of PLiD

When an intense laser pulse impinges on a surface, specifically a metal, it is partially reflected and partially absorbed. Reflection is generally caused by fast absorption-reemission processes on free electrons, whereas absorption is a result of momentum transfer from photons to fermions. The penetration depth δ of electromagnetic waves in metals is given by the equation

$$\delta = \frac{\lambda}{4\pi k},$$

where the absorption constant k resembles the complex index of refraction and λ the wavelength of the impinging electromagnetic wave.[2] In an ideal metallic lattice the amplitude E of an electromagnetic wave progressing in direction z is exponentially damped according to the function [3]

$$E(z) = e^{\frac{-z}{\delta}}.$$

Accordingly, photons affect an outmost layer with a thickness of a few nanometers. In this volume free electrons absorb photons and are thereby excited into empty states above the Fermi level E_F. Assuming a single-photon absorption process, this raises the initial energy of affected electrons by an amount of energy equal to *hv*. Electron-electron scattering leads to rapid thermalization of excited electrons, which returns in the generation of heat. Depending on the excitation density, which is typically high when lasers are used to induce the process, thermalization takes about 1 ps in metals.[4] As a result, a thin film of metal is nearly instantaneously liquefied and therefore meets the initial condition for dewetting.

Liquid thin films feature intrinsic instabilities that originate from collective mechanisms of energy minimization. Two mechanisms, the *Rayleigh-Plateau instability* and *spinodal dewetting,* are commonly accepted to be the major driving forces that lead to thin film dewetting.

The *Rayleigh-Plateau instability* describes the tendency of a fluid jet or a static cylinder of a fluid to break up into droplets.[5] Striving for a more favorable state of energy, liquids break the cylindrical geometry to form spheres because this geometry features the lowest surface-to-volume-ratio. The process starts with perturbations of various curvatures of which some grow with time while others decay. Modes that exhibit

curvatures larger than the radius of the cylinder grow exponentially and become predominant with time. The fastest growing mode is a perturbation with the wavelength $\lambda \cong 9.02\ R_0$, where R_0 is the radius of the cylinder. Figure 2.2.1 sketches how perturbations in a liquid cylinder grow over time and eventually collapse into droplets.
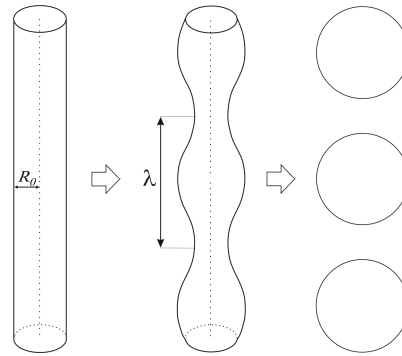
Figure 2.2.1: The Rayleigh-Plateau instability.

From a geometrical point of view the *Rayleigh-Plateau instability* appears to be an inappropriate model for the prediction of laser-induced self-organization on surfaces. Nevertheless, J. Fowlkes et al. demonstrated that PLiD-stimulated dewetting scenarios can be described using this theory.[6,7] The group studied the dewetting behavior of lithographically patterned nickel strips on silicon and found that the mechanism of nanoparticle formation in this system conforms with the theory of Rayleigh and Plateau.
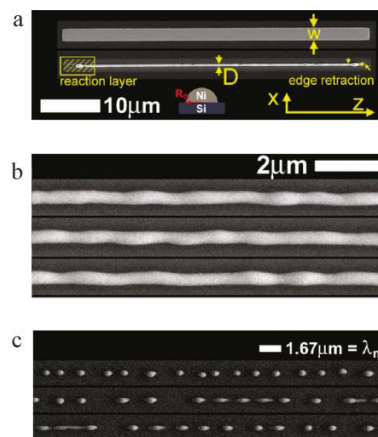
Figure 2.2.2: Experiment conducted by J. Fowlkes et. al. [6]

(a) Patterned nickel thin film strips on silicon illustrated by SEM; width W = 2 μm, thickness D = 23 nm. (b) Nickel strips after laser-induced fluid retraction. The rivulets feature a radius R_0 of about 165 nm. (c) Result of PLiD stimulated by 20 laser pulses at a laser fluence of ϕ = 380 mJ/cm^2. The scale bar equals the fastest growing mode as it was predicted using a modified approach based on the theory of Rayleigh and Plateau for simulation.

In a first step the metallic thin film strips were converted into semi-cylindrical rivulets utilizing an effect called *self-perfection by liquefaction* (SPEL).[8] In a second step these rivulets were subjected to PLiD yielding an array of nanoparticles. The *Rayleigh-Plateau instability* was found to describe the main features of the dewetting process given that system specific effects like liquid-solid interactions are considered in the simulation. These findings are rather impressive since they demonstrate that the *Rayleigh-Plateau instability* applies to nanoscopic systems as well. Unfortunately, this approach is not generally applicable since patterned metallic thin films are not typically employed as starting materials for PLiD-stimulated self-organization. For this reason, a universal model is needed to predict dewetting on standard precursor materials. Currently a theory called spinodal dewetting holds the promise of achieving this goal.

Spinodal dewetting belongs to the spontaneous self-organization processes, which means that it occurs in the absence of boundary creating effectors such as seeds or contaminations. The theory considers interfacial forces to be the origin of local thickness fluctuations and spontaneous ruptures in liquid thin films.[9,10] The term *spinodal dewetting* is adopted from the theory of *spinodal decomposition*, which describes fluctuations in the composition of solid solutions as a function of the mixing ratio (2.2.3)
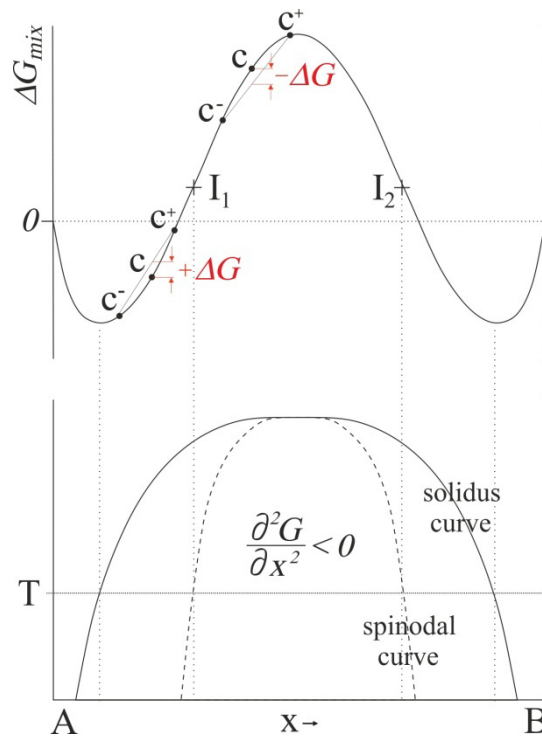

Fig. 2.2.3: Spinodal decomposition of a binary mixture.[inspired by 11]

9

The course of free energy ΔG_{mix} in a binary mixture, in which the enthalpy of mixing is positive, shows two inflexion points I_1 and I_2. Between these points fluctuations in the bulk composition c, indicated as c⁻ and c⁺, result in a decrease of free energy $(-\Delta G)$ thus favoring separation into the components x_A and x_B. As a consequence, *spinodal decomposition* progresses in any region in which the second derivate of $G(x)$ satisfies the condition

$$\frac{\partial^2 G}{\partial x^2} < 0.$$

Continuous minimization of the total free energy supports spontaneous decomposition until a stable coexisting composition is reached, which is defined by a tangent to the minima of the free energy curve.

The theoretical basis of *spinodal decomposition* was adopted by A. Vrij in order to establish the theory of *spinodal dewetting.* He assumed that *spinodal dewetting* will occur in any system that satisfies the basic condition

$$\frac{\partial^2 G}{\partial h^2} < 0,$$

where h is the thickness of the liquid thin film and G the interfacial free energy per unit area.[9] Changes in the free energy per unit area result from fluctuations on the surface of a liquid thin film, as illustrated in Fig. 2.2.4.
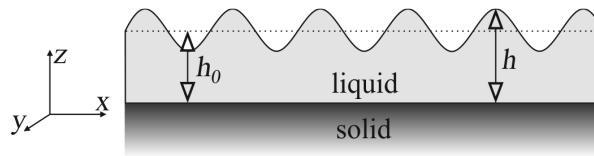
Fig. 2.2.4: Schematic illustration of spinodal dewetting.

For the evaluation of perturbation heights in a liquid thin film subject to dewetting, Vrij employed a Fourier component of the type

$$h - h_0 = \sum_{\rho=-\infty}^{+\infty} \sum_{\sigma=-\infty}^{+\infty} H_{\rho\sigma} \cdot e^{[ip(\rho x + \sigma y)]},$$

where $p = \frac{2\pi}{a}$ and a^2 is the unit area of a square expanding in x and y direction. The Fourier coefficients were connected in pairs since h is a real quantity:

$$H_{-\rho,-\sigma} = H_{\rho\sigma}^* \qquad H_{\rho,-\sigma} = H_{-\rho,\sigma}^* \qquad H_{-\rho,\sigma} = H_{\rho,-\sigma}^*.$$

Each Fourier component contributes independently to the change of free energy that is associated with perturbations in the interface of a liquid thin film. For instance, the Fourier component $H_{\rho\sigma}$ gives the contribution

$$a^2 H_{\rho\sigma} H_{\rho\sigma}^* \left[\frac{1}{4} \gamma p^2 (p^2 + \sigma^2) + \frac{1}{2} \left(\frac{\partial^2 G}{\partial h^2} \right)_0 \right],$$

where γ is the surface tension. Provided that the basic condition $\frac{\partial^2 G}{\partial h^2} < 0$ is satisfied, this component will continuously decrease the free energy in a liquid thin film if

$$\lambda_c = \sqrt{\left[\frac{-2\pi^2 \gamma}{\left[\left(\frac{\partial^2 G}{\partial h^2} \right)_0 \right]} \right]},$$

where λ_c is the critical perturbation wavelength. The equation defines the spinodal curve of thin film dewetting. When $\lambda < \lambda_c$ the thin film will remain stable, whereas perturbations with $\lambda > \lambda_c$ will lead to spontaneous dewetting driven by a continuous decrease of free energy.

Vrij's theory of spinodal dewetting is a carefully designed approach that bears the potential to simulate or rather predict dewetting in real systems. However, practical applications are complicated by a number of physical quantities that must be accounted for in order to obtain viable results. Aware of this problem, Vrij took interfacial forces into consideration as one of the major influencing factors for thin film dewetting. This was achieved by an integration of nonretarded Lifshitz – van der Waals forces into the term for excess free energy per unit area represented as

$$G = \frac{-A}{12\pi h^2},$$

where A is the Hamaker constant for interactions in binary systems. When this equation is used for the calculation of $\frac{\partial^2 G}{\partial h^2}$ the critical wavelength can be expressed as:

$$\lambda_c = h_0^2 \sqrt{\left(\frac{4\pi^3 \gamma}{A} \right)}.$$

Provided that the Hamaker constant and the surface tension are known for a respective system, the calculation of λ_c provides a basis to predict the average particle spacing and

size that will result from spinodal dewetting. Prior to doing this, the stability of the respective thin film should be evaluated in order to determine its general tendency for dewetting. This is performed by calculations of the free energy per unit area as a function of film thickness $G(h)$ and its second derivative. Fig. 2.2.5 exemplifies this procedure schematically.
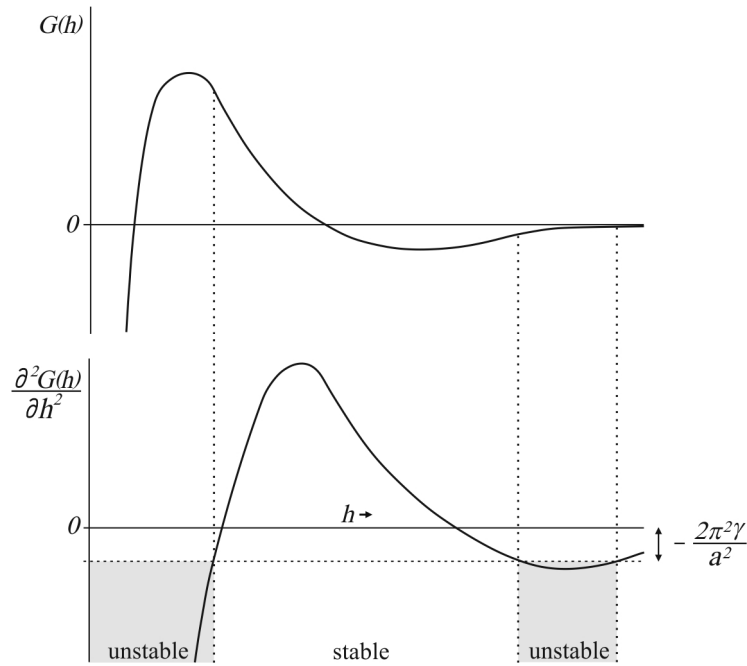
Fig. 2.2.8: Schematic illustration of $G(h)$ and its second derivative as a function of h. [adopted from 9]

The graph indicates that thin films in two thickness ranges will be unstable. The highest tendency for spinodal dewetting can be assumed for thin films in right-bended regions of $G(h)$ where the curvature peaks, because there the decrease in free energy associated with height perturbations reaches its maximum. Naturally, such perturbations can only exist in thin films that feature a minimum lateral dimension of $a > \lambda_c$. As a consequence, instability will only occur in systems satisfying the condition

$$\frac{\partial^2 G}{\partial h^2} < -\frac{2\pi^2 \gamma}{a^2}.$$

Since this term is always negative for thin films, the instability regions are slightly narrowed due to border suction.

2.3 State of the Art in the Field of PLiD

Although Vrij's theory of spinodal dewetting provides a general framework for the description of dewetting in thin films, it was initially not designed to account for phenomena that occur under special conditions like those emergent during PLiD. In contrast to polymer thin films, which have been the primary subject of Vrij's studies, PLiD is utilized to modify metals, dielectrics and semiconductors. Due to the high melting points of these materials, conventional annealing techniques, like those applied to stimulate dewetting in polymer thin film, are inadequate in terms of practical application. Lasers present the ultimate solution for this problem because they offer the potential for selective surface heating of a broad variety of materials. The growing availability of highly intense laser sources led to dynamic progress in the field of laser-induced self-organization on surfaces. In 1996, Bischof et al. investigated the effects of PLiD on substrate supported metallic thin films.[12] The group deposited Au, Ni and Cu with film thicknesses in the range of 25 to 50 nm on fused silica substrates and subjected those to intense pulses of a nanosecond Nd:YAG laser emitting at 532 nm wavelength. Surface analyses resulted in the finding that the dewetting behavior of liquefied metallic thin films follows spinodal instability characteristics, which was once again confirmed by Herminghaus et al. two years later.[13] Investigating the dewetting behavior of Co films in the thickness range from 1 to 8 nm, Farvazza et al. demonstrated in 2006 that nanoparticle formation by PLiD is a robust and scalable process.[14] He found that repeated photo-thermal cycling induced by nanosecond laser pulses leads to a subsequent optimization of spatial order and homogenization of nanoparticle size. The latter is scalable by the thickness (h) of the precursor thin film and shows a dependency of $\sim h^2$ to the nanoparticle diameter, which is once more in agreement with the theory of spinodal dewetting. However, slight deviations from theoretical expectations were found in almost every study. The reason for this was identified by Trice and coworkers in 2008.[15] They found that the transversal temperature profile in thin films subjected to PLiD is a discrete function of h which peaks at a certain thickness h^* in the thin film volume. This characteristic is attributed to nonlinear optical absorption and thermocapillary effects in metal thin films. As a consequence, h^* is considered to be the effective film thickness for simulations rather than h.

2.4   Laser-induced Periodic Surface Structures (LIPSS)

When intense laser pulses impinge on the surface of solid materials, they may leave periodic structures on laser-affected areas. As a result of that, the phenomenon became known by the name Laser-induced Periodic Surface Structures (LIPSS). The first observation of LIPSS was reported by M. Birnbaum already in 1965, soon after lasers had become available.[16] He conducted experiments using a pulsed ruby laser that emitted a wavelength of 694.3 nm. With the objective to determine optical damage thresholds of semiconductor materials he subjected single crystalline germanium to a power density between 10^4 and 10^5 W/cm^2. Surface examination of the irradiated specimen revealed the interesting result illustrated in Fig. 2.4.1.
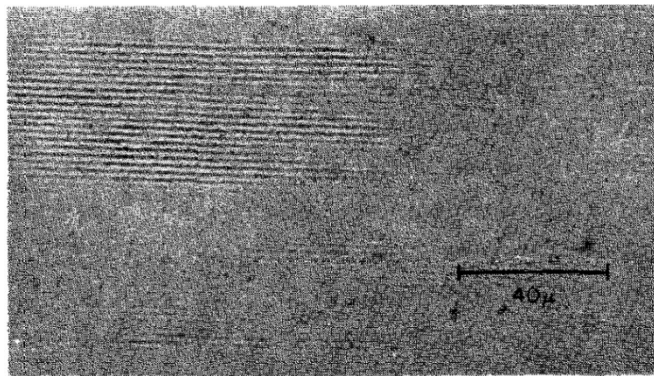
Fig. 2.4.1: Original picture taken form a germanium specimen after pulsed laser irradiation under an incidence angle of about 75°.[16]

Birnbaum remarked the following about his observation: *"The damage is seen as a series of parallel grooves localized in patches on the semiconductor surface. The direction of the grooves runs parallel to the projection of the laser light onto the surface of the sample. This was verified by noting that the direction of the grooves was unaffected by rotation of the sample around an axis perpendicular to the surface."* Birnbaum was also the first one who considered diffraction effects to be the origin of this phenomenon. Based on theoretical models describing the intensity distribution in the focal plane of a focused laser beam he derived the equation

$$d_v = 2\lambda \left(\frac{f}{a}\right)^2,$$

where d_v is the distance between successive maxima in the observed pattern, λ the laser wavelength, f the focal length of the lens used to focus the laser beam and $2a$ the lens' aperture. Even though Birnbaum's equation was quickly refuted, his basic idea of LIPSS being a result of light diffraction was taken up and continued.

2.5 Theoretical Background of LIPSS

In 1973 Emmony, Howsen and Willis reported on laser-induced damages on optical components of a TEA CO_2 laser. Similar to Birnbaum's observations, they found regular structures on several germanium etalons and output mirrors after intense laser irradiation. The periodicity of these structures was determined to be about 10.6 μm and correlates with the emission wavelength of the TEA CO_2 laser. In search for an explanation they established a theory which became known as the *surface scattered wave model*.[17] It is based on the assumption that propagating wave fronts are scattered at contaminations and defects localized on the surface of optical components. Interferences between incoming wave fronts and scattered wave fronts provoke the formation of interference fringes. The assumed mechanism is sketched in figure 2.5.1.
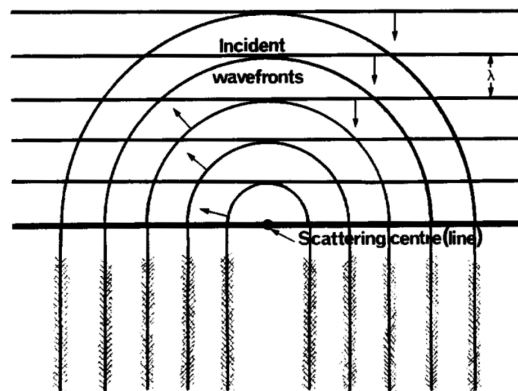
Fig. 2.5.1: Original picture illustrating the surface scattered wave model.[17]

Scattered wave fronts propagate radially from a scattering center thus interfering with non-scattered wave fronts incoming under normal angle of incidence in a way that creates an interference pattern with a spacing that correlates to the laser wavelength. As a result of emergent interference fringes the surface of the optical component is subjected to a regular pattern of locally varying photon densities. When optical intensities in the peak regions of this fringe pattern exceed the damage threshold of the component this will persistently change the surface of the material due to the emergence

of LIPSS. The model can also be employed to estimation LIPSS periodicities that result from non-normal incident angles of the laser beam (Fig. 2.5.2).
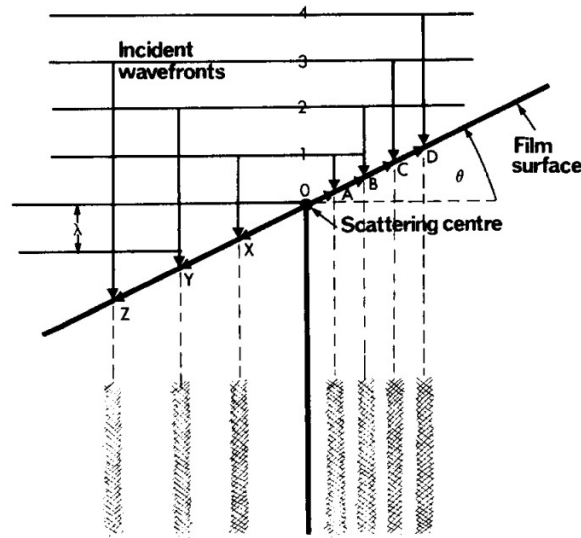
Fig. 2.5.2: Schematic illustration of fringe pattern formation on an inclined.[17]
surface with respect to the direction of laser pulse propagation.
0, 1, 2, 3, 4 sketches the wavefronts of the incident beam
A, B, C, D and X, Y, Z resembles radiation components
scattered towards or away from the laser source.

When 0X = 1X, 0Y = 2Y, etc., interference will occur in the forward scattering direction whilst for 0A = 1A, 0b = 2B, etc., in the backward direction. Accordingly, the periodicity d of LIPSS generated by constructive interference between scattered wavefronts and incident wavefronts propagating in an angle θ with respect to the surface normal is given by:

$$d = \frac{\lambda}{1 \pm sin\theta} \qquad\qquad\qquad d = \frac{\lambda}{cos\theta}$$

for incident wavefronts with p-polarization   for incident wavefronts with s-polarization

The equations show that the surface scattered wave model is based on a classical trigonometric approach. Despite its simplicity, it actually provides accurate predictions of LIPSS periodicities even if only for so-called low spatial frequency LIPSS (LSFL) generated up to a critical angle of incidence. Figure 2.5.3 shows a comparison between theoretical prediction and experimental observation of LSFL.
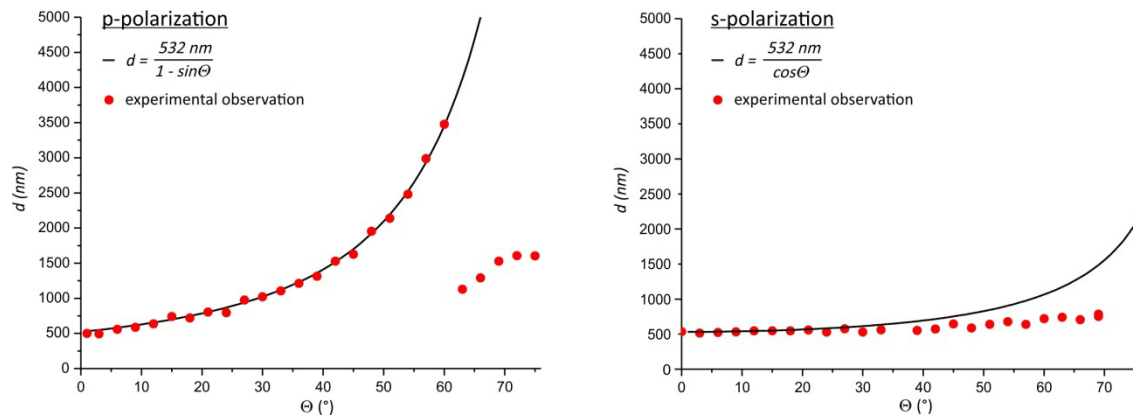
Fig. 2.5.3: Theoretical expectations of LIPSS periodicity versus experimental observation.

LIPSS patterns were generated on stainless steel EN 1.4301 (AISI 304) using a nanosecond pulsed laser emitting a wavelength of 532 nm. The left graph opposes the angular dependence of LSFL-periodicity generated under p-polarized irradiation (red dots) to that derived by the surface scattered wave model. The right graph illustrates the same comparison for LFSL generated under s-polarized irradiation.

As the left graph shows, the surface scattered wave model is agrees with experimental results for LSFL generated under p-polarized irradiation. If, however, a critical incidence angle (greater than 60° in the case of stainless steel) is exceeded, substantial deviations between theory and observation become apparent. In fact, this sudden change in LIPSS periodicity at the critical angle is only one peculiarity not covered by the surface scattered wave model. Another is the LIPSS orientation, which is typically perpendicular to the laser polarization for semiconductors and metals, but flips into parallel orientation with respect to the polarization as soon as a critical angle of incidence is exceeded. In the case of LSFL generation by s-polarized irradiation, discrepancies between theory and observation are clearly notable. The model overestimates angle dependent increases in pattern periodicity starting from incident angles of approximately 30°. It must be concluded that the surface scattered wave model is not consistent and thus limited in its performance to predict LSFL patterns with satisfying accuracy. Nonetheless, it indicates that interference effects may have an influence on the LSFL generation process. Due to these limitations several other theories were proposed particularly in the 1970's. Maracas et al. brought standing acoustic waves into consideration and Isenor argued that plasma oscillations might be the essential driving force for LIPSS generation.[18,19] Van Vechten assumed LIPPS to be a consequence of plasmon condensation, which was taken up by Keilmann and Bai who actually provided some evidence for the occurrence of surface polaritons during LIPSS generation.[20,21] However, none of these hypotheses have left the stage of speculation so far. Finally, in 1983 Sipe et al. introduced a promising concept that

17

contributed significantly to the understanding of LIPSS formation on surfaces.[22] It is known as the *efficacy factor model,* which is due to the fact that it primarily accounts for the influences of surface roughness to the spatial deposition of irradiated energy on surfaces. The basic idea behind this approach was inspired by the results of Emmony and Oron who recognized the influence of surface roughness on the symmetry breaking in homogeneous light fields.[23,24] With that in mind, Sipe attempted to implement this factor in a model that provides a mathematical basis for the prediction of LIPSS. His approach was very ambitious since the surface condition of materials is not a physical quantity and thus not easy to determine. Accepting that surface acquisition or simulation in real space is practically impossible, Sipe circumvented the problem by studying LIPSS formation processes in the Fourier domain. This was put into practice by projecting scattering patterns of surfaces to a screen. Fourier analysis enabled the assessment of surface conditions as a manageable set of specific values. Now that a method for surface acquisition was available Sipe, integrated all essential variables into an idealized model that is sketched in Fig. 2.5.4.
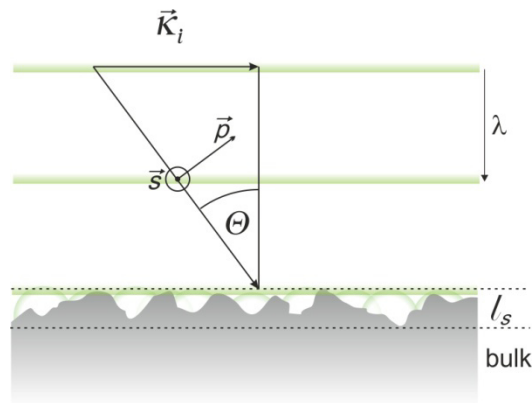
Figure 2.2.1.4: The efficacy factor model.[inspired by 22]

He abstracted the laser beam as a plane wave with a wave vector of magnitude $\tilde{\omega} = 2\pi/\lambda$ that approaches a surface from vacuum. The surface is considered to be a microscopically rough texture, also referred to as *selfedge,* that features a texture depth of l_s, where $l_s \ll \lambda$. When a wave approaches the selfedge, its vector component $\vec{\kappa}_i$, which is parallel to the surface, is scattered into the components $\vec{\kappa}_i$ and $\vec{\kappa}$. Assuming that both components interfere with incident wavefronts, this leads to inhomogeneous absorptions with a magnitude of $\eta(\vec{\kappa}, \vec{\kappa}_i) \, |\, b(\vec{\kappa})|$ just below the interface between the *selfedge* and the vacuum. In this term $b(\vec{\kappa})$ is the Fourier component that describes the surface roughness and $\eta(\vec{\kappa}, \vec{\kappa}_i)$ is the efficacy factor quantifying the efficacy with which

inhomogeneous absorptions emerge at the selfedge. The efficacy factor contains the shape factor s, which is an expression for the aspect ratio of the surface texture, and the form factor f as a measure for the texture volume fraction in the selfedge region. Sipe assumes that LIPSS formation starts at a location in the selfedge region where maximum inhomogeneous absorption occurs, thus giving rise to the prediction $I(\vec{\kappa}) \propto \eta(\vec{\kappa}, \vec{\kappa}_i) \mid b(\vec{\kappa})\mid$. This is most likely to happen at a location satisfying the condition $\mid \vec{\kappa}_i \pm \vec{\kappa} \mid = \widetilde{\omega}$, which is characterized by a peak in the efficacy factor. Sipe conducted simulations of this complex framework using fundamental theories like the Maxwell equations and implemented the influences of laser polarization and oblique angles of incidence to his model. He was the first who established a model that predicts LSFL patterns originating from a variety of irradiation conditions. His model allows for accurate predictions of pattern formation on well absorbing materials, like metals or semiconductors, stimulated by nanosecond lasers. Although the efficacy factor model is the most advanced approach to date, imperfections can still be found in this theory. For instance, transient changes of the materials properties that occur during a laser pulse are not considered in the theory. This leads to discrepancies between theoretical prediction and experimental observation. Another important factor that is hardly tangible is the influence of the laser pulse length to the pattern periodicity. The effect becomes obvious when LIPSS is generated using lasers pulses in the pico- or femtosecond time domain. Resulting pattern periodicities are by far smaller than the efficacy model predicts. These so called high spatial frequency LIPSS (HSFL) are currently not fully understood and controversially discussed in literature.

2.6 State of the art in the field of LIPSS

LIPSS is under research for nearly 50 years now but particularly in recent years increasing numbers of publications indicate a rapidly growing interest in this self-organization phenomenon (fig. 2.6.1).
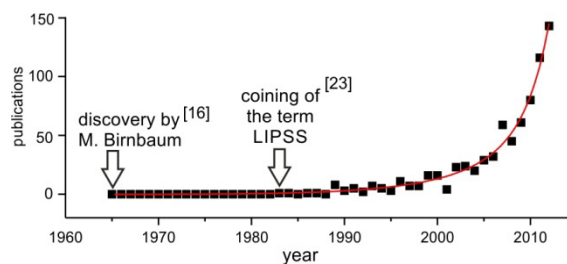

Fig. 2.6.1: Publication statistic of LIPSS. [data based on google scholar]

19

Besides continuous efforts to elucidate the physical background of LIPSS, a growing trend towards application-oriented research is notable. Affordable laser technique and the perception that the implementation of self-organization processes bears great potential for technological applications may by the reasons for this initiative. Its simplicity and flexibility make LIPSS truly attractive for applications. Addressable pattern periodicities span the micro-to-nano-gap thus providing a high degree of adaptability to respective requirements. The opportunities are further enhanced by the possibility to control the pattern shape. Depending on the type of laser polarization LIPSS generates dot- and cross-patterns,[25,26] circles and spirals[27,28] and even hierarchical patterns.[29] The self-constructing nature of periodic light intensity patterns was demonstrated on metals, dielectrics, semiconductors and polymers.[30-33] One of the major differences compared to conventional pattern formation techniques is the fact that LIPSS is in essence a feedback mechanism of light-matter interaction. Hence, the clear allocation of roles between tool and workpiece becomes indistinct. Material characteristics and surface quality have a large influence on the pattern formation process. For instance, LSFL form patterns perpendicular to the laser polarization on semiconductors and metals but parallel on dielectrics and polymers. This difference is attributable to material-specific characteristics of light interaction. Pattern formation on metals and semiconductors is believed to be the result of surface plasmon polariton excitation [34,35] while nonradiative interactions referred to as *radiation remnants* are thought to initiate patterns on dielectrics and polymers.[36] The formation of LIPSS patterns stimulated by femtosecond lasers is even more interesting since transient changes of optical properties must be taken into account. A promising approach in this field is the implementation of the Drude model into the Sipe theory. Originally designed for the description of charge transfer processes in metals, the Drude model was modified to account for transient intrapulse changes in the optical properties of solids subjected to femtosecond laser pulses.[37,38] This gives the opportunity to predict laser-stimulated pattern formation on a variety of materials. Most notably, experiments indicate pulse-shaping to be a very promising approach for highly controlled LIPSS generation.

3   Cumulative Part

This thesis pursues the goal of expanding the knowledge in the field of self-organization by investigating the possibility to imitate nature's principle of pattern formation in complex systems. As an introduction to the subject the scientific approach is described and put into relation with regard to its relevance for the basic objective of this thesis: *learning from nature*. Scientific results that address particular key questions are evaluated and discussed in separate sections. The main question concerning the general feasibility of self-organization and reaction control in complex system is evaluated in section 1, *Learning from Nature*. Section 2, *Materials by Design*, is devoted to the question to which extent the outcome of self-organization processes in complex systems can be predicted. This is an important criterion to meet the demand for purposeful fabrication of materials on the one hand and an indicator for the level of control achievable via directed self-organization on the other hand. Section 3, *Functional Materials,* demonstrates the potential of laser-directed self-organization as a fabrication technique for materials of practical applicability.

In order to prevent confusion or misunderstanding, it is hereby declared that this study is not concerned with the investigation of living systems but with the general phenomenon of self-organization apparent across systems. The systems under investigation comprise composite materials of which one is a well known alloy and thus to be categorized as an inorganic composite whilst the other is a hybrid system containing inorganic components as well as organic ones.

The investigative approach of the study is characterized by a stimulus-response-strategy, which aims at the disclosure of subsequent changes that occur in complex systems as a result of iteratively stimulated self-organization. The prerequisite for practical implementations of this approach is a high degree of stimulus control. Due to unparalleled precision and stability, lasers are excellent tools for this task and were thus employed for the stimulation of self-organization processes in complex systems throughout this study (see chapter 2 for details).

One of the basic effects that may arise when a laser pulse impinges on the surface of a solid material is named pulsed laser-induced dewetting (PLiD). It occurs when the irradiated energy is sufficiently high to induce photo-thermal heating above the melting point of an affected material. As a consequence, the surface is nearly instantaneously liquefied and thus encounters a variety of destabilizing forces that provoke a fast progressing scenario of transformations. After a few nanoseconds heat dissipation into the underlying bulk puts a stop to these transformations due to rapid resolidification. In order to create selective surface modifications, PLiD is typically performed in an iterative manner. The potential of this method for controlled nanostructure formation on surfaces is documented in several studies. Section 2.1 outlines the state of knowledge in this field. Most of these studies are focused on PLiD-stimulated nanostructure formation starting from well-defined model systems like substrate supported metallic thin films. However, nature's concept of self-organization is essentially characterized by a low-effort, high outcome principle that leads to order formation in complex systems. Consequently, the question of whether PLiD provides the potential to imitate nature to some extent must demand some attention. First of all an appropriate model system had to be selected. The choice fell on stainless steel grade EN 1.4301 (AISI 304), one of the most versatile and widely applied grades of stainless steel worldwide. Beyond its abundance, an important criterion for selection was the fact that this alloy is well-investigated and understood. This provides a solid basis for the interpretation of PLiD-induced changes. Most notably, the alloy contains a plurality of species including four transition metals, one half metal and several trace elements. Table 3.1 shows an overview of its composition.

Fe	Cr	Ni	Mn	Si	N	C	S
balance	18	10	2	1	< 0.1	< 0.07	< 0.015

Tab. 3.1: Composition of stainless steel grade EN 1.4301; all figures in weight per cent.

Compared to previous studies concerning PLiD, the model system investigated in this thesis is by far more complex from a compositional point of view. Furthermore, PLiD modifications were performed in ambient air. Considering that surface liquefaction of stainless steel EN 1.4301 requires temperatures exceeding 1450 °C, the oxidation of alloy components is to be expected as an additional pathway for reactions thus further enhancing the degrees of freedom of the model system.

The mechanisms of PLID-stimulated self-organization in the model system were investigated using the iterative stimulus-response-strategy mentioned above. Practically, this was conducted by subjecting stainless steel samples to different numbers of recurring PLiD events followed by in depth analysis of the resulting changes. PLiD stimulation of stainless steel was performed using a nanosecond pulsed laser with a pulse width of 5 ns and a wavelength of 532 nm. Each pulse delivered a laser fluence of 2.88 J/cm^2 thus heating affected surface areas to liquefaction. At a given pulse frequency of 30 kHz this event repeated itself every 33 μs and is referred to as *dewetting cycle* (DC) in the following.

Compared to nature's concept of order formation in complex systems, the approach deployed in this study represents an abstract interpretation of the basic principle behind stimulated self-organization. Both, the model system and the harsh conditions it is subjected to, have no counterpart in nature but this is actually irrelevant since self-organization is understood as a phenomenon apparent across systems. Taking this into account, the attempt to implement its basic principle to the system under investigation is a step towards *learning from nature*.

3.1 Learning from Nature

When a laser pulse train impinges on the surface of stainless steel this stimulates recurrent dewetting scenarios. Since the process features certain similarities to the gradual development of specific features in living systems, it can be understood as a fast progressing evolution scenario. Using PLiD as a stimulus, diverse stages of pattern maturity are traversed in time spans well below one second. This makes real-time studies of selective maturity stages considerably difficult. In order to circumvent this problem, 24 stainless steel samples were generated, of which each was subjected to an individual number of dewetting cycles in the range between 10 and 589 DC. This procedure permitted the tracing of PLiD-stimulated transformation within a broad range of evolutionary states. Examinations of modified steel samples revealed that PLiD actually provides the potential to stimulate evolutionary developments. Oxidation products on the surface of stainless steel feature a series of patterns that change their face depending on the number of DC applied Fig. 3.1.1.
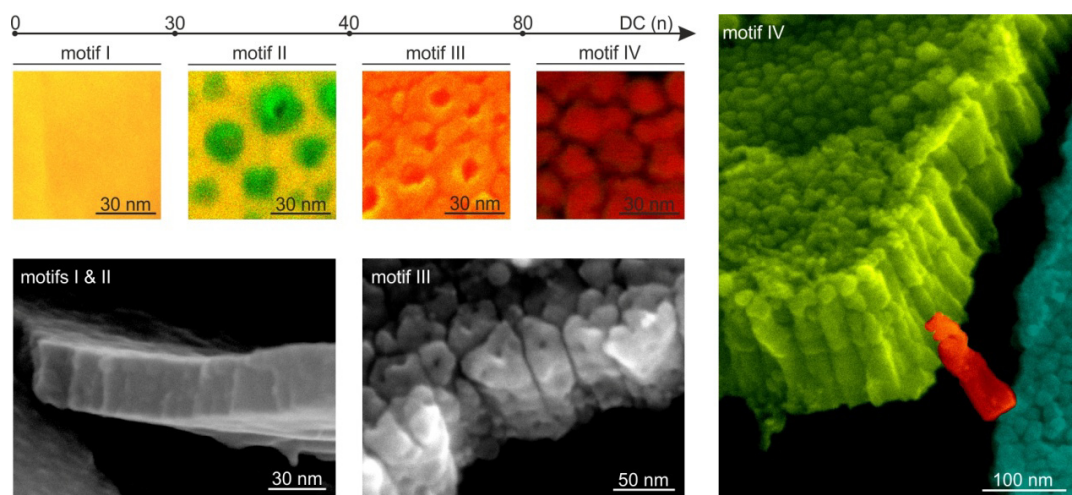
Fig. 3.1.1: DC-dependent evolution of metal-oxide structures on stainless steel visualized by SEM.

Recurrent PLiD-stimulations lead to a scenario of pattern evolution that can best be illustrated by means of typical structure motifs as shown in the top left corner of fig. 3.1.1. The coloration of these SEM pictures results from interpolations of morphological images (green) with mappings of material specific information (red). This technique allows for the visualization of segregations that obviously occur in the formerly homogeneous passivation film of stainless steel (motif I) as soon as a number of 30 DC is exceeded. Recurring photothermal stimulations lead to gradual transformations in composition and morphology, which are characterized by the formation of core-shell nanostructures (motif III) beginning at 40 DC. When exceeding 80 DC these merge into nanoparticles (motif IV), which continuously increase in size when stimulation is further progressed. SEM investigations on breaking edges of structure motif III and IV show closely packed arrays of vertically alligned nanostructures. This demonstrates that PLiD stimulated pattern formation progresses into the depth of materials if this dimensional degree of freedom is available. Commonly applied precursor systems like substrate supported metallic thin films do not support such dimensional freedom as they resemble quasi-2D-systems (see chapter 2.3). This, however, constrains the feasibility to generate anisotropic patterns like those observed in this study. The dimensionalty was thus identified to be an important factor that contributes to the complexity of a precursor system and therefore determines the general capacity of a sysem to form complex patterns. Considering the high degree of order and the shape anisotropy of motif III and IV nanostructures, this poses the question by which mechanism such patterns are formed. The answer to this lies hidden beyond the steel surface (Fig. 3.1.2).
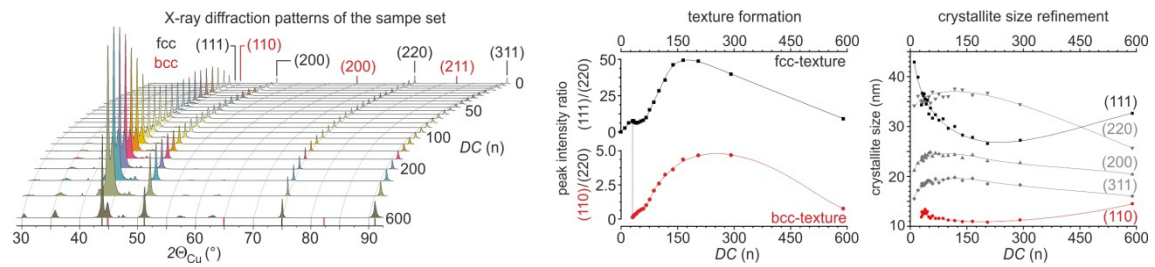
Fig. 3.1.2: Crystal structure analyses of steal samples subjected to increasing numbers of DC.

Investigations using X-ray diffraction revealed that PLiD treatments subsequently transform stainless steel into a nanocrystalline and textured material. The observed crystallite size refinement is a consequence of high cooling rates that occur during PLiD cycles. Rapid heat dissipation into the bulk quenches the growth of maturing crystallites in a stage of nucleation. Simultaneously, oriented crystallite growth is promoted along the vector of heat flow. When PLiD stimulation is steadily repeated this leads to a stepwise optimization of oriented crystal growth and thus texture evolution. A schematic illustration of this process is given in Fig. 3.1.3.
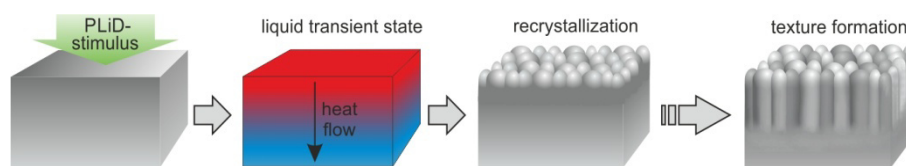
Fig. 3.1.3: PLiD-stimulated texture evolution in stainless steel.

From a thermodynamic point of view the pattern formation process must be accompanied by a reduction of entropy. The fact that photothermal heating initially increases the entropy of the system is not in contradiction with this statement because entropy is withdrawn from the system in the process of heat dissipation. As a consequence, oriented crystal growth is directed by the vector of heat flow. The disclosure of texture development is an essential prerequisite to understand the formation process of vertically aligned metal-oxide nanostructures like those illustrated in fig. 3.1.1. As mentioned in the introduction, PLiD stimulation of stainless steel was performed in ambient air and is thus accompanied by oxidation of reactive species like Fe, Cr, Ni, Mn, and Si. Hence, the mechanism that leads to the formation of anisotropic metal oxide structures can be understood as a template assisted oxidation process. Recurring photothermal stimuli support texture formation on the one hand but also simultaneous oxidation of nanocrystallites on the other hand thus replicating the emergent texture consistently into a pattern of vertically aligned metal-oxide nanostructures, as schematized in fig. 3.1.4.
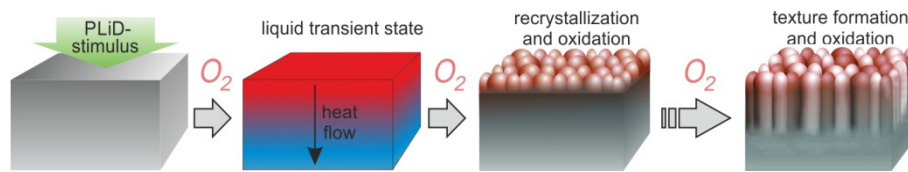
Fig. 3.1.4: Model of template assisted pattern formation in stainless steel.

The model of template assisted pattern formation is supported by good dimensional compliance between PLiD-generated nanocrystallites in stainless steel and metal-oxide nanostructures on its surface. Template assisted pattern formation represents a fundamental principle of structure development in living systems. Its occurrence in a laser-stimulated self-organization process is thus particularly interesting.

In conclusion, it can be stated that laser-stimulated self-organization in complex systems provides the potential to imitate nature to some extent. PLiD was not expected to perform comparable to nature's perfection but it demonstrated that nature's concept of pattern formation in complex systems can be imitated in its principles.

3.2 Materials by Design

One of the most promising trends in modern material science is the design of complex materials. Complexity is the key to materials with vastly enhanced properties whilst at the same time it poses major problems with regard to material synthesis. Structure and composition control at the nanoscale and beyond are the challenges that must be met before specific designs can be translated into materials. Currently available fabrication techniques are either unable to cope with this task or inefficient from an economic point of view. Self-organization in complex systems could be the answer to this problem provided that its outcome was predictable and controllable. The following section is concerned with the identification of trends and regularities that occur upon self-organization in the system under investigation. Conclusions drawn from empirical findings are also envisaged as a basis for predicting of laser-stimulated self-organization in other complex systems.

As mentioned in section 3.1, the morphology of laser-induced oxidation products on stainless steel is governed by the crystalline structure of the underlying bulk. This allows for the deduction that structure control is achievable throughout the system provided that crystal structure formation can be intentionally directed into specific channels. The current state of knowledge in this field allows for predictions of laser-

induced transformations of crystal structure with satisfying resemblance to empirical observation. Applied models are based on numerical simulations that also include material-specific and stimulus-specific parameters. Calculations of heat gradients and associated cooling rates that occur upon laser stimulation form the basis for the prediction of structural changes in a certain material. Yang et al. implemented this approach for the determination of laser-induced nanocrystallite formation in stainless steel.[39] Accordingly, the crystallite size shows a logarithmic relationship to the cooling rate, which in turn depends on the irradiated energy density. This finding provides a basic level of structure prediction; however, a problem that remains with the existing model are transient changes of the material properties that already occur in the duration of the very first laser pulse but particulary when a material is repeatedly stimulated. The influence of this quantity has not been considered in theory so far because it is hardly tangible and nonlinear. In the system under investigation the effects of transient changes reflect in the unsteady development of texture and crystallite size evolution (cp. fig. 3.1.2). This shows that accurate stucture prediction will remain a challenge, especially for systems that undergo severe changes when stimulated. Even if this problem could be solved the fact remains that structure prediction does not amount to structure control. Practically speaking, structure formation is not arbitrarily controllable but depends on boundary conditions, which are inherent to the system in most instances. In the present example the pool of accessible crystallite sizes is limited by the thermal conductivity of stainless steel. Moreover, the direction of heat flow is not intentionally controllable but obeys to the laws of thermodynamics. By the fact that heat flow predetermines the direction of crystal growth, the orientation of the resulting texture is beyond control. To this end, it must be concluded that high-level structure control cannot be achived at the moment.

In order to evaluate the potential of PLiD for compositional control in a complex system, the oxidation products that build up on the surface of stainless steel were examined according to the stimulus-response strategy. This was put into practice by surface sensitive mass spectrometry, a technique that allows for compositional depth profiling with high transversal resolution. It is essentially based on layer-by-layer ablation via a scanned antimony ion beam and subsequent analysis of ionized fragments by time-of-flight secondary-ion-mass-spectrometry (ToF-SIMS). Figure 3.2.1 shows the layering structure of stainless steel samples subjected to different numbers of DC.
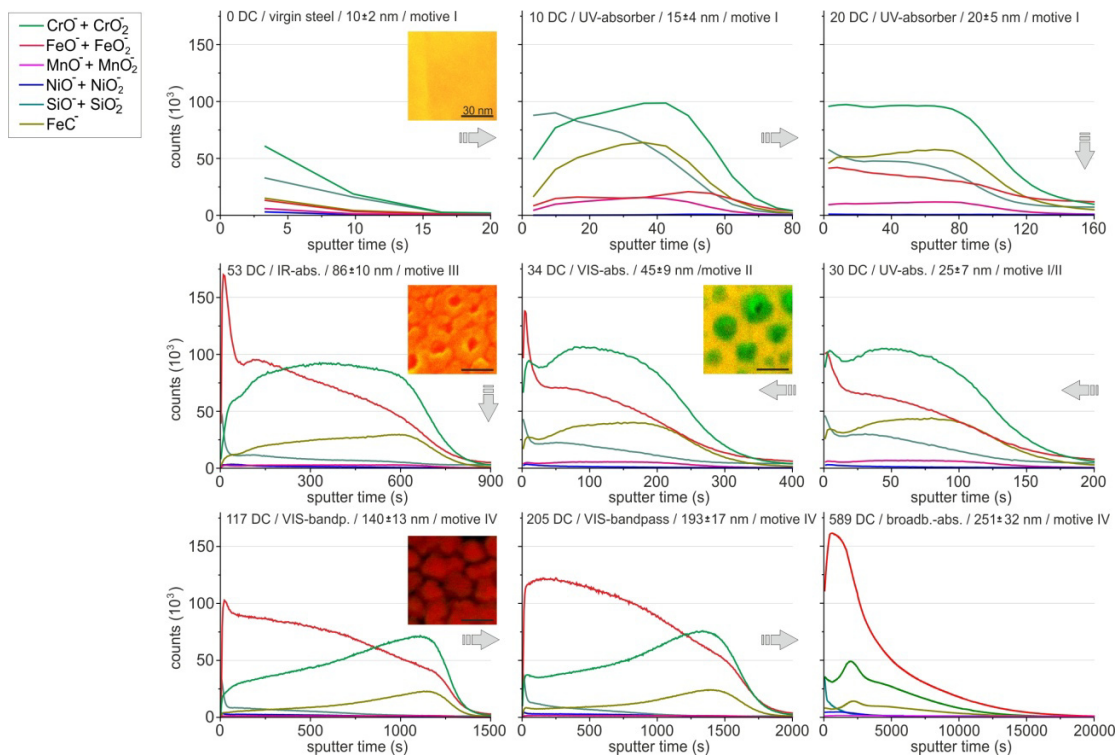
Fig. 3.2.1: ToF-SIMS depth profiles of oxidation products on PLiD-modified stainless steel.
Arrows guide through an evolution of compositional depth profiles obtained from samples subjected to increasing numbers of DC. A species assignement is given in the legend (top left). The number of PLiD cycles applied to a certain sample, as well as its affiliation to a structure motif and the layer thickness of the oxide scale, accompany each depth profile.

Compositional screenings of the sample set reveal a DC-dependent evolution of layering structures in PLiD-generated oxidation products. Prior to laser treatment stainless steel is covered by a natural passivation film composed of Cr- and Si-oxides to the most part. Even a number of 10 DC is enough to induce Fe-carbide accumulation in the passivation film. This is to be taken as an indicator for oxygen deficiency in areas affected by photothermal heating. Recurring stimulations activate iron species on the surface of stainless steel that diffuse more and more into the passivation film, eventually penetration it (at about 30 DC) on their way towards oxidation sites. Cr- and Fe-oxide contents in the film gradually increase while Si-, Mn- and Ni-oxides are more and more diminished. Between 34 and 53 DC the thin film enrichment with Cr-oxide passes a maximum while Mn- and Ni-oxide contents fall into a minimum. PLiD modifications exceeding 53 DC are characterized by excessive Fe-oxide accumulation in the film. Finally, a pervasive stream of thermally activated iron-species inverts the former layering structure completely. The overall segregation scenario can be understood from a thermodynamic point of view; fig. 3.2.2 demonstrates this.
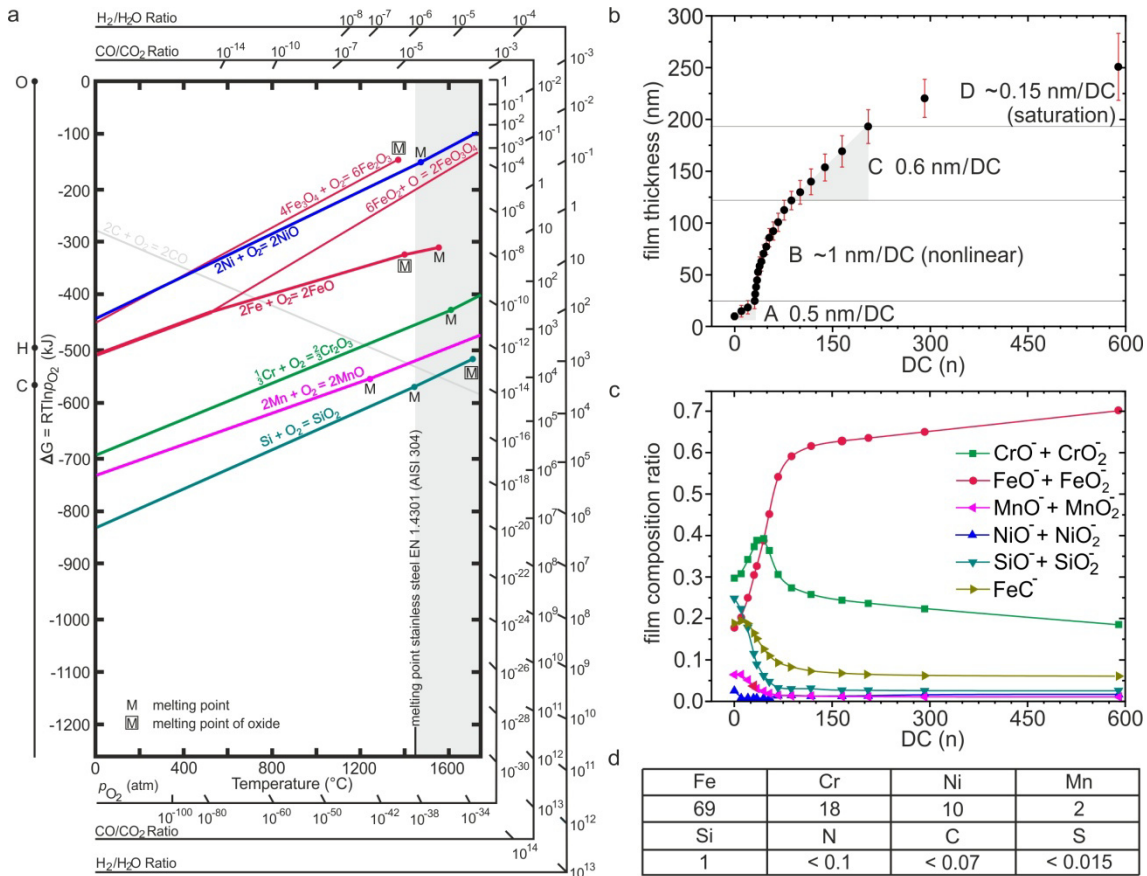
Fig. 3.2.2: Theory and observation of PLiD-induced oxide segregation on stainless steel EN 1.4301. (a) Ellingham diagram for stainless steel EN 1.4301 (AISI 304). Thermodynamic parameters were extracted from D. R. Gaskell.[40] (b) DC-dependent metal-oxide growth on EN 1.4301. (c) DC-dependent metal-oxide composition on EN 1.4301. (d) Alloy composition of EN 1.4301 in weight per cent (wt%).

As the Ellingham diagram shows, Si features the highest decrease of free Gibbs energy upon oxidation and Ni the lowest. Practically speaking, this means that Si scavenges oxygen much more efficiently than any other element contained in stainless steel even though it belongs to the minor alloying elements (1 wt%). The observed course of thin film composition indicates a strong influence of the thermodynamic reactivity sequence Si>Mn>Cr>>Fe>Ni on the metal-oxide segregation scenario. Adherence to this sequence results from the fact that thin film growth is governed by oxygen deficiency, as indicated by Fe-carbide contents observed in all passivation films. Increasing numbers of DC initially result in progressive oxidation of Si and Mn, according to the given reactivity sequence. The Cr-oxide ratio does not rises until those minor alloying elements suffer local depletion. Although Cr is the major alloying element (18 wt%), its feedstock in the laser affected zone is still limited. Consequently, Fe is consistently oxidized for DC numbers exceeding 48 because the content of Cr subsequently depletes in the laser-affected zone. As the basic component of steel, Fe virtually never depletes

thus leaving low reactive Ni in a nearly unoxidized state. Evidently, the observed oxide segregation scenario is in good agreement to thermodynamic expectations. A result like this could not be assumed necessarily since PLiD-stimulated reactions proceed under non-equilibrium conditions. The results show that PLiD stimulated segregations in a stainless steel are not arbitrarily controllable. Nevertheless, the findings also demonstrate that PLiD-induced oxide segregations are predictable by means of thermodynamic considerations. This may give the opportunity to forecast segregation scenarios in other complex systems as well.

3.3 Functional Materials

Nature creates functional materials using the concept of self-organization in complex systems. Controlled by specific stimuli a system is rearranged in a way that yields certain functionality. The question what functionality essentially is or rather what it defines is actually difficult to answer. In living systems it is the property of materials required to fit specific needs of an organism. The palette ranges from optical diversification, which is important for photosynthesis or camouflage, over mechanical and tribological aspects that destine shape, robustness and locomotion of an organism, to catalytic, magnetic and electrical specializations that form the basis for metabolism, sensing and signal processing, just to name a few. The following chapter outlines the opportunities to create functional materials using the concept of laser-directed self-organization and reaction control in complex systems.

As demonstrated above, recurrent PLiD stimulation of the model system stainless steel induces evolutionary developments of structure and composition. Treatments like this affect the properties of the material in two ways: Firstly, structure formation on the nanometer scale is known to evoke unusual properties distinctly different from those of the same bulk material. Associated effects are basically a result of quantum confinement that occurs as soon as the nanostructure length scale is less than the characteristic wave function in bulk matter. Secondly, changes in the composition of nanostructures create additional effects. In the present example, nanostructures observed on stainless steel include transition metal oxides (TMOs), which belong to the most diverse and richest classes of materials in terms of optical, electrical, thermal, magnetic and catalytic properties. The combined effects of structural and compositional transformations to the properties of stainless steel can already be perceived with the naked eye (3.3.1).
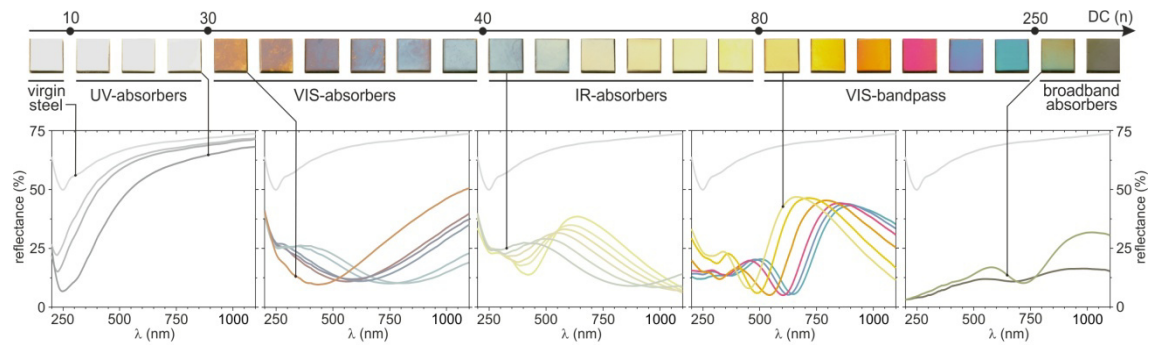
Fig. 3.3.1: DC-dependent changes of the optical properties of PLiD-modified stainless steel
Pictures of all 24 steel samples are given at the top. The sample reffered to virgin steel represents a mirror polished steel sheet (10 x 10 x 0.8 mm) prior to PLiD modification (DC = 0). Integrating sphere measurements of all samples are given below. A spectrum of virgin steel accompanies all spectra as a reference. The spectra are color coded with respect to the visual appearance of each sample.

When visually inspecting the sample set, a series of vivid colors resulting from PliD-stimulations in the range from 80 to 205 DC immediately draws attention. Apart from that, the majority of surface modifications are less eye-catching but by no means less interesting. Integrating sphere measurements reveal a wide variety of optical diversity that covers the spectral range from ultraviolet (UV) to near-infrared (NIR). Gradual thickenings of the natural passivation film on stainless steel from 10 nm to about 25 nm (cp. fig. 3.2.2 b) lead to an increase in UV absorption, which can be observed for steel samples subjected to 10 – 30 DC. If, however, 30 DC are exceeded, this causes nanostructure development in formerly homogeneous TMO thin films thus evoking quantum effects. The strong impact of structural transformations is evident by an abrupt change of the optical properties from UV to VIS absorbers. Motif II structures, which are responsible for this, can be understood as matrix-embedded nanoparticles that constitute grain boundaries in TMO films (cp. fig. 3.1.1). TMOs feature strong electronic coupling to vibrations of the local environment; hence, even marginal variations in composition or structure induce explicit shifts in the bandwidth of d-d electronic transitions. This makes optical spectroscopy a sensitive probe for the tracing of PLiD-stimulated changes. A close correlation between structural motifs and optical effects is clearly evident. The transition from motif II to motif III is characterized by a shift from VIS broadband absorption to IR absorption. Exceeding 80 DC, motif III transforms into motif IV, a structure that constitutes even sharper interfaces in the solid solution of TMOs thus evoking explicit electronic transitions located in the VIS region of the optical spectrum. The influence of interfaces on the optical properties of TMO nanocomposites is demonstrated in fig. 3.3.2.
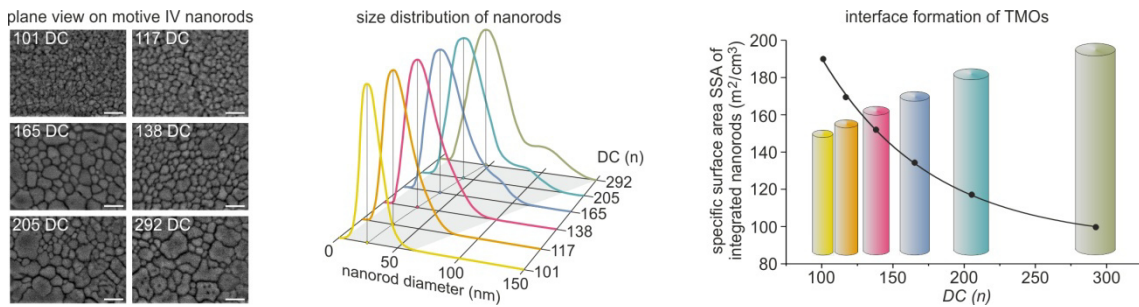
**Fig. 3.3.2: DC-dependent size distributions of motif IV nanostructures**
The picture on the left shows SEM plan views on motif IV nanorod arrays resulting from PLiD modifications in the range between 101 and 292 DC. The scale bar is 100 nm. A statistical evaluation of nanorod size distributions is displayed in the center. Based on these data the selective surface area (SSA) of integrated nanorods was calculated and pottet versus DC (right). The averaged dimensions of nanorods resulting from respective numbers of DC are sketched for comparative purpose.

Considering that the composition of motif IV nanostructures is not subject to significant fluctuations (cp. fig. 3.2.2 c) this gives rise to the assumption that optical effects observed for VIS bandpass absorbers are primarily a result of the nanorod size distribution. By fact that the size distribution of motif IV structures is DC-dependent this enables optical tuning throughout the color spectrum and beyond. The correlation between structure and DC can best be illustrated by the total area of interfaces generated in TMO nanocomposites. The selective surface area (SSA) of integrated nanorods was found to decrease exponentially with increasing DC. A self-organizaton process allowing for selective adjustment of optical properties, is certainly attractive for application. However, more interesting is the fact that PLiD-stimulated optical shifts represent changes in the electronic structure of TMOs. It can thus be expected that integrated TMO nanostructures of such complexity and order hold hidden functionalities. Still, the exploration of system specific details is not the primary scope of this study but rather the identification of general effects that can be utilized for laser-stimulated self-organization in complex systems.

PLiD is essentially based on liquefaction and subsequent resolidification of solids. This raises the question whether traversed phase transitions have a lasting effect on the phase composition of an affected system. In fact, phase separation was observed in the model system even though the alloy under investigation is generally not susceptible to this type of transformation. X-ray diffraction patterns obtained from stainless steel samples subjected to increasing numbers of DC indicate a phase separation to occur when 30 DC are exceeded (see fig. 3.1.2). The face centered cubic phase (fcc), which is commonly found in austenitic steels like EN 1.4301, is intermixed with a body centered cubic

phase (bcc) characterized by emerging peaks at 44.42 ± 0.01 ° $2\theta_{CuKa}$. It is also salient to note that fcc crystals cover a size distribution from 15 to 43 nm whereas the bcc phase features smaller crystals with a narrow size distribution ranging from 11 to 14 nm. According to a study by Yang et al., cooling rates between $10^6 - 10^7$ K/s are nessesary for the formation of fcc nanocrystals wheras the formation of bcc nanocrystals requires cooling rates of about 10^8 K/s.[41] Since the size of PLiD-generated nanocrystals depends on the cooling rate, it can be deduced that bcc crystals originate from an earlier stage of structure maturity than fcc crystals. For the model system this is given by the fact that bcc is the initial phase that occurs at the solidification contour of austenitic steel melts.[42] The retransformation from bcc to fcc is a diffusion process and thus time dependent, which makes it accessible for processes like PLiD that control liquid lifetimes on the nanosecond time scale. Evidently, cooling rates that occur during a PLiD cycle are too fast for a complete retransformation into the thermodynamically favored fcc-phase, thus capturing bcc intermediates in a non-equilibrium state. Depending on the precursor system, phase separations offer the potential to enrich the pool of controllable material properties. In the present example, PLiD-stimulated bcc precipitations transform formerly paramagnetic stainless steel EN 1.4301 subsequently into a ferromagnetic material (fig. 3.3.3).
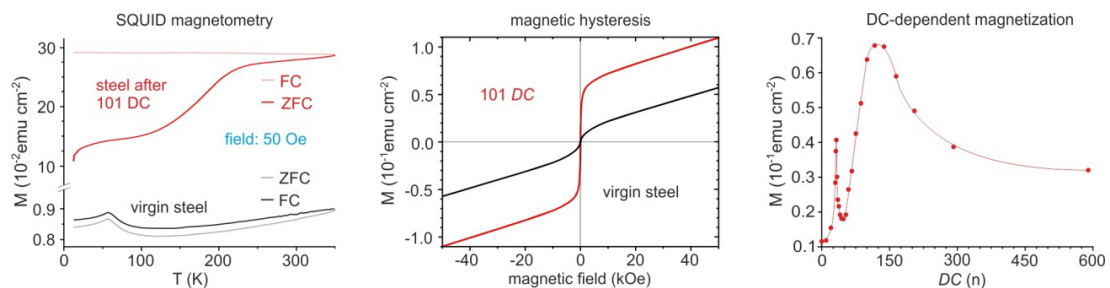
Fig. 3.3.3: Magnetic properties of stainless steel before and after PLiD modification.
The magnetic characteristics of untreated and PLiD-modified steel are shown on the left and in the center. ZFC-FC measurements at a field of 50 Oe indicate that untreated steel behaves similar to a Pauli paramagnet which, orders antiferromagnetically at approximately 60 K. In contrast to that, PLiD-modified steel features sharply enhanced magnetization that increases with temperature. The graph on the right shows the course of DC-dependent saturation magnetization. The degree of magnetization is taken as an indicator for the amount of PLiD-induced bcc-precipitates.

Magnetometric measurements indicate that recurrent PLiD-stimulation generates a ferritic phase that superimposes the paramagnetic properties of stainless steel. The coercivity of PLiD modified steel ranges between 37 and 65 Oe, which is rather low for a ferromagnetic material. This tendency to superparamagnetic behavior is supposed to be attributed to very small magnetic domain sizes in the range of 6.1 to 8.4 nm.

As the DC-dependent magnetization of stainless steel shows (fig.3.3.3 right) recurrent PLiD-stimulation leads to a stepwise increase of saturation magnetization that reaches a maximum between 100 and 150 DC. Excessive thermal cycling was found to reduce the saturation magnetization of PLiD-modified steel. The effect is supposed to be a consequence of bcc to fcc retransformation due to thermal equilibration. Interestingly, the course of PLiD-stimulated magnetization shows an additional peak at 33 DC. This singularity in saturation magnetization was found to be accompanied by a special magnetic profile on the surface of the affected steel sample (fig. 3.3.4).
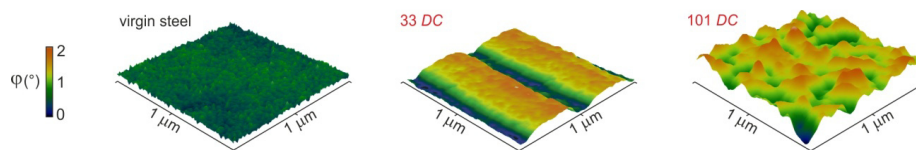

Fig. 3.3.4: Magnetic profile analysis by magnetic force microscopy (MFM).

The figure shows that PLiD-stimulated bcc precipitations resulting from 101 DC change the initially faint magnetic profile of virgin stainless steel into an isle-like profile with a roughness on the nanometer scale. Compared to this, the steel sample subjected to 33 DC features a regular magnetic pattern with a periodicity of about 500 nm. The formation of this pattern is attributed to a phenomenon named laser-induced periodic surface structures (LIPSS); details are provided in chapter 2.4. LIPSS is commonly accepted to occur as a consequence of light-matter feedback mechanisms, which create temporary instabilities in an initially homogeneous spatial state. When specific irradiation conditions are met, those temporary instabilities swing up to a standing wave thus creating a photonic fringe pattern that subjects the underlying solid to periodic intensity fluctuations. As the results show, irradiation conditions suitable for the stimulation of LIPSS lie within the PLiD parameter space. This is particularly interesting since LIPSS and PLiD have been regarded as separate phenomena so far. The gradual transition between both phenomena provides the opportunity to induce self-organization processes similar to those stimulated by PLiD with spatial selectivity. Due to the fact that LIPSS is very flexible in terms of pattern creation this bears great potential for the generation of functional surfaces. Addressable patterns periodicities span the micro-to-nano-gap and depend on parameters such as the laser wavelength, the angle of incidence, the pulse width, the refractive index of the irradiated system and the laser polarization. A linearly polarized nanosecond laser, as it is utilized here, produces a line pattern with a periodicity close to the laser wavelength (fig. 3.3.5).
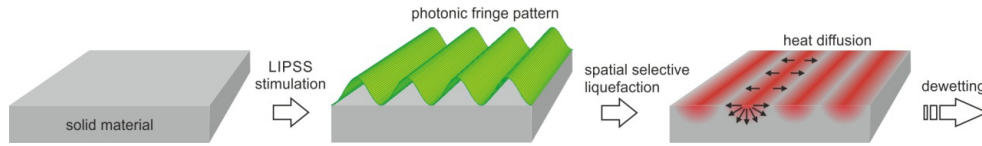
**Fig. 3.3.5: Schematic illustration of LIPSS-stimulated pattern formation.**

When a photonic fringe pattern, as it is generated by LIPSS, impinges on a solid, this event will induce localized liquefaction according to the fringe pattern intensity profile. Subsequent dewetting scenarios can thus be assumed to proceed similarly to PLiD-stimulated self-organization processes but in spatial confinement. The formation of a regular magnetic profile on steel subjected to LIPSS is thus the result of spatial selective phase separation restricted to regions where maximum cooling rates occur. This is most likely the case in zones subjected to maximum fringe pattern intensity because in those areas massive thermal gradients rapidly diffuse due to multidirectional heat dissipation. Hence, bcc nanocrystals precipitate in zones predetermined by the intensity distribution of the fringe pattern (fig. 3.3.6).
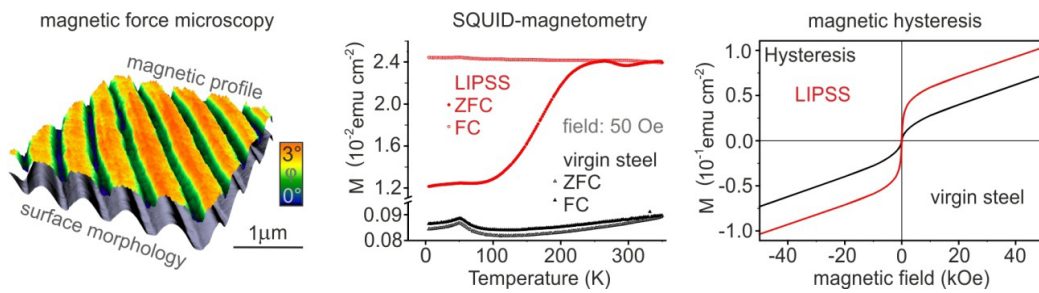
Figure 3.3.6: Magnetic characteristics of stainless steel stimulated by LIPSS.
The magnetic functionalization of LIPSS-modified stainless steel is shown on the left. ZFC-FC curves (center) recorded at a field of 50 Oe indicate a change from paramagnetic to ferromagnetic behavior as a result of LIPSS-stimulation. A tendency to superparamagnetic behavior can be deduced from a slight deblocking at about 240 K and a low coercivity of 80 Oe measured at room temperature (right).

As expected, the magnetic behavior of LIPSS-modified steel is similar to that resulting from PLiD. A weak deblocking at about 240 K in the ZFC curve and a low coercively of the magnetic hysteresis emphasize the tendency to superparamagnetic behavior. This is attributable to the formation of slightly smaller magnetic domain sizes of about 6 nm due to faster cooling rates that result from multidirectional heat dissipation. Well-defined magnetic patterns on the surface of stainless steel visualize the zones in which bcc precipitation took place. Evidently, zones of maximum magnetization coincide with morphological peak regions, thus indicating a close correlation between structural and morphological transformations. Surface examinations using AFM and SEM provide deeper insights into LIPSS stimulated morphology formation (fig. 3.3.7).
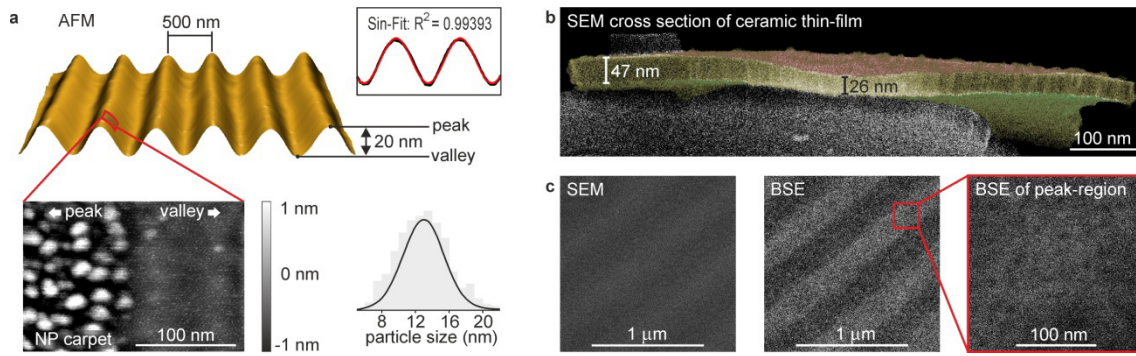
Fig. 3.3.7: Morphological inspection of LIPSS-modified stainless steel.
(a) The topographical analysis by atomic force microscopy (AFM) shows a nearly sinusoidal waveform with a peak-to-valley amplitude of about 20 nm and a periodicity of 500 nm. High resolution scans on a single wave section revealed closely spaced nanoparticles located exclusively in peak regions. The nanoparticles feature a Gaussian size distribution peaking at 13 nm. (b) The thickness of LIPSS-generated oxide films was determined to be between 19 and 52 nm using cross sectional SEM inspections. (c) Plan view SEM inspection shows a slightly patterned surface. Backscattered electron imaging (BSE) visualize LIPSS patterns clearly thus indicating material contrast between peak- and valley-regions.

As AFM measurements show, LIPSS transforms the surface of steel into a sinusoidal topography with a periodicity close to the laser wavelength and an amplitude of about 20 nm. It can thus be suspected that the fringe pattern, which created this pattern, featured a sinusoidal intensity profile. Closely spaced nanoparticles located on morphological peak regions bear witness to site-selective dewetting. Considering that bcc nanocrystals in a size range between 5.4 and 12.8 nm (estimated using the Scherrer equation) undergo a volume increase of about 30 % when oxidized this makes a direct connection between structural and morphological transformations obvious. Increased oxidation in peak regions is considered to be a reinforcing effect on the formation the hierarchical morphology. This can be deduced from PLiD experiments concerning the correlation between oxide film thicknesses and irradiated total intensity (cp. fig. 3.2.2 b). Accordingly, maximum oxide film thickness is to be expected in regions subjected to maximum fringe pattern intensity and vice versa. SEM-inspections on breaking edges of LIPSS-generated thin films show variances in the film thickness; however, a reliable differentiation between peak and valley regions could not be achieved with this method. The analytical problem was solved by conductive atomic force microscopy (CAFM), a technique that allows for nanoelectrical surface examinations. The approach is based on the deduction that a metal-oxide coating with periodically varying film thickness features a periodically varying dielectric strength. Since this quantity is basically a function of film thickness, a pattern of periodically varying resistance is to be expected on LIPSS-modified steel (3.3.8).
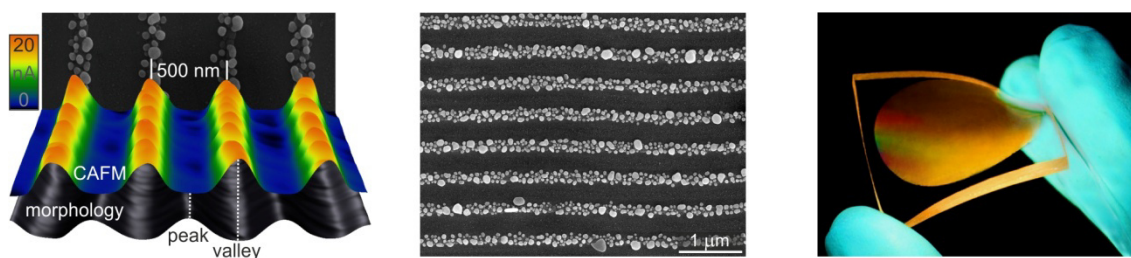
Fig. 3.3.8: Nanoelectrical properties of LIPSS-modified stainless steel.
The surface examination of LIPSS-modified steel by conductive atomic force microscopy is shown on the left. Contact scans with a tip bias of 3 V revealed increased current flow in morphological valley regions compared to peak regions. An example for the application of LIPSS-modified steel as a patterned electrode is given in the center. Electrochemical reduction of Ag^+ yielded site-specific deposition of silver nanoparticles in morphological valley regions. Deposited Ag nanoparticle patterns can be transferred to secondary substrates like PDMS, as the picture on the right demonstrates.

This assumption was confirmed as the CAFM mapping of LIPSS-modified steel demonstrates. Contact scans with a biased tip inflicted electrical breakdowns exclusively in valley regions. Surfaces with spatially varying conductivity on the submicron scale are attractive for electrochemical applications as they provide spatial reaction control. For demonstrative purposes, LIPSS-modified steel was employed as a electrochemical template. Reduction of Ag^+ from an aqueous electrolyte yielded site specific deposition of silver nanoparticles in valley regions of the LIPSS template. The implementation of deposited materials into functional systems is possible via pattern transfer to secondary substrates like PDMS, as it is demonstrated in fig. 3.3.8 on the right. This opportunity combined with the diversity of materials accessible by electrochemical deposition prospects a broad application potential for templates generated by LIPSS.

In account to the above mentioned effects of PLiD to the chemical composition of oxide films on stainless steel, chemical patterning is to be expected as yet another effect resulting from a stimulus that features a locally varying intensity profile. Unfortunately, the lateral resolution of ToF-SIMS was found to be insufficient for chemical diversification between peak and valley regions of LIPSS patterns. In order to circumvent this problem, a model was established that allows for the prediction of chemical patterns on stainless steel. The approach is based on the finding that the composition of laser-generated oxidation products on stainless steel depends largely on the irradiated intensity. When this correlation is determined for a system, this knowledge can be utilized to predict the type of chemical patterning that is to be expected after fringe pattern impact. The procedure is demonstrated in fig. 3.3.9.
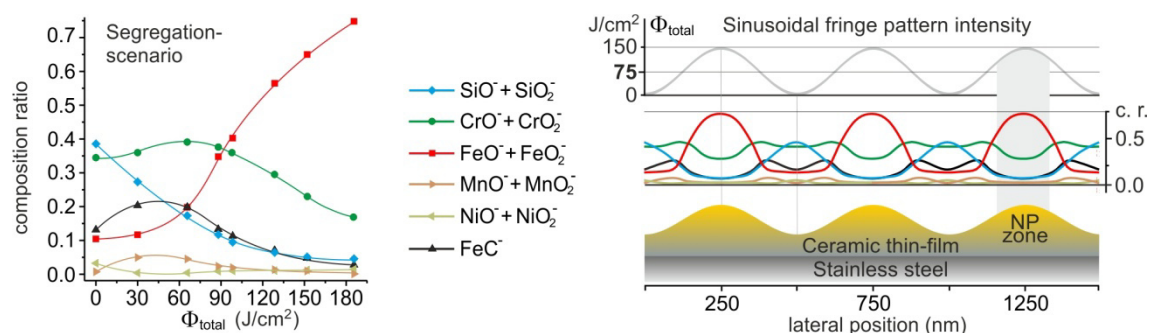
Fig. 3.3.9: Prediction of chemical patterning on the example of LIPSS-modified stainless steel.
The correlation between surface composition and irradiated intensity, denominated as Φ_{total}, is given on the left. Mass spectra obtained from the surface of eight stainless steel samples irradiated at different intensities were analyzed and combined to this graph. Mass fragments used for species assignment are given in the legend aside. The composition model on the right illustrates the chemical surface patterning on stainless steel after fringe pattern impact.

Assuming a sinusoidal fringe pattern intensity profile, which seems appropriate with regard to a sinusoidal surface morphology determined by AFM (cp. fig.3.3.7 a), the chemical patterning can be predicted by the assignment of data correlating irradiated intensity and surface composition (left graph) to the spatial intensity profile of the fringe pattern. The graph on the right presents the outcome of this procedure. Accordingly, peak regions of LIPSS-modified steel are primarily composed of Fe-oxide in solid solution with Cr-oxide, while valley regions consist of Cr-oxide and silica for the most part. The prediction is in good agreement with the material contrast of LIPSS visualized by BSE (cp. fig. 3.3.7 c) that indicates a lower effective atomic number Z_{eff} in valley regions compared to peaks. By the fact that the atomic number is almost equal for Cr and Fe ($Z_{Cr} = 24$ and $Z_{Fe} = 26$), a decrease of Z_{eff} must be entailed by Si ($Z_{Si} = 14$), which, according to the model, predominantly exists in valleys regions. Another validation for the model is based on its prediction that nanoparticles observed in peak regions consist of Fe-oxide to the most part and thus represent a catalyst that promotes the growth of carbon nanotubes (CNTs). The result of chemical vapor deposition on LIPSS-modified stainless steel is illustrated in fig. 3.3.10.
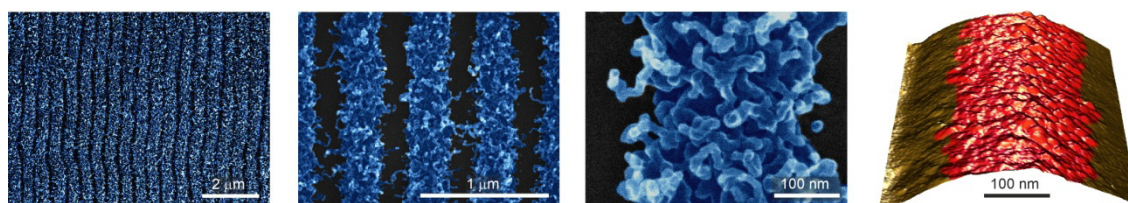

Fig. 3.3.10: Catalytic properties of LIPSS-modified stainless steel.
Patterned CNT growth in a periodicity of 500 nm accounts for the site-selective catalytic activity of LIPSS-modified steel. The AFM topography on the right shows the catalytically active peak region.

In fact, patterned CNT growth on LIPSS-modified stainless steel was achieved. High site-selectivity to the peak region substantiates the validity of the established model thus making it attractive for the prediction of LIPSS-stimulated chemical patterning on other composite materials as well. Most notably, the example introduces LIPSS as a process, which enables the fabrication of surfaces with special catalytic properties.

The introduced concept of self-organized pattern formation in complex systems is evidently very prolific. Nonetheless, a major hurdle that needs to be taken on the way to practical implementations is up-scaling, or in other words, LIPSS formation over large surface areas. Regrettably, it is in the nature of laser-based processes to affect only small surface areas of several square micrometers in size. Homogeneous LIPSS formation over extended surface areas is challenging but not impossible, as fig. 3.3.11 shows.
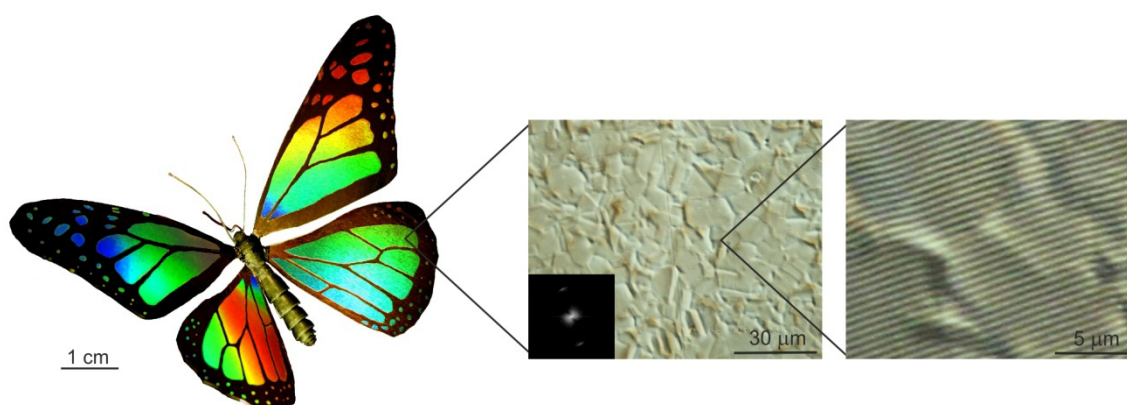
Fig. 3.3.11: LIPSS-formation over extended surface areas of stainless steel EN 1.4301.

Besides the functionalities previously described, LIPSS formation on steel causes significant changes of the optical surface properties. The colorful appearance of LIPSS-modified steel is attributed to a regular morphology of sinusoidal waves that feature diffraction characteristics. The effect is a good quality indicator for successful LIPSS-generation, as the butterfly demonstrates. It is made from LIPSS-modified steel foil and features a wing span of 7.5 cm. Industrial grade stainless steel appears to be a rather unsuitable material for controlled nanostructure generation as its surface features various defects and inhomogeneities. Nonetheless, the laser process developed for large area LIPSS-formation encounters this challenge with a high degree of robustness. As the magnifications show, the process transforms extended surface areas into well-ordered LIPSS, irrespective of grain boundaries or defects.

In conclusion, it can be stated that the concept of laser-directed self-organization and reaction control in complex systems provides the potential to fabricate a variety of functional materials that feature attractive properties. Compared to conventional fabrication techniques the applied process is in essence quite simple but also sur-prisingly productive and flexible, as the following process diagram outlines (fig. 3.3.12)
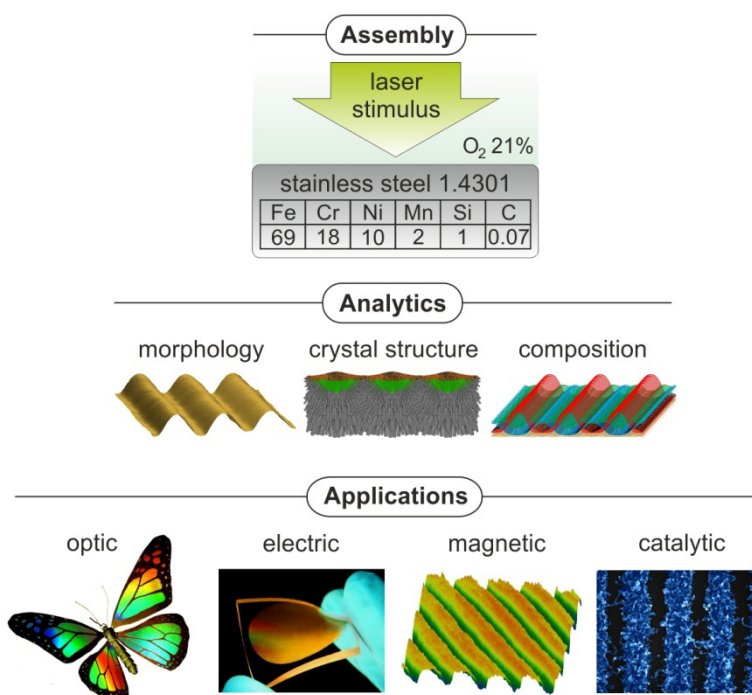
Fig. 3.3.l2: Laser-directed self-organization and reaction control in complex systems.

The pyramidal shape of this diagram reflects the performance that could be achieved when natur's low-effort-high-outcome-principle of order formation in complex systems was sucessfully adoptable for fabrication purposes. However, industrial production lines in use today rely on a multitude of subsequent processing stages that eventually converge into a product. This strategy ensures a high level of process control thus facilitating purposeful production but it is also time-consuming and costly. The concept of self-organization in complex system is inversely related to the conventional strategy. On the one hand, it features convincing efficiency but on the other hand it is barely controllable and understood. The need for predictability and purposeful design currently impedes practical applications of self-organization. Consequently, more fundamental research is needed to fill the numerous gaps of knowledge in this field.

In the previous sections photothermal stimulation was demonstrated to be a promising approach for the direction of self-organization processes in complex systems. It is thus an interesting question whether laser-stimulated pattern formation can also be achived

using photochemical reaction control. Non-thermal stimulation provides the opportunity to expand the applicability of laser-directed self-organization to temperature-sensitive materials. The large variety of accessible effects makes photochemistry particulary attractive for the fabrication of functional materials. Photochemical reactions types include bond cleavage, rearrangement and polymerization, just to name a few.

In the following, a short proof-of-concept experiment is presented that demonstrates the viability of laser-directed self-organization and reaction control using photochemical reaction pathways. The model system comprises anodic aluminium oxide (AAO) as a carrier material for a reaction mixture. This includes 7-hydroxycoumarin, a photoexcitable molecule, acting as mediator for the photoreduction of Ag^+ on the one hand and structure forming precursor for as-generated Ag^0 on the other hand. The experimental setup is illustrated in fig. 3.3.13.

reaction mixture:
0.19 M 7-hydroxycoumarin
0.19 M $AgNO_3$
in water/acetone/ethanol 2:4:1
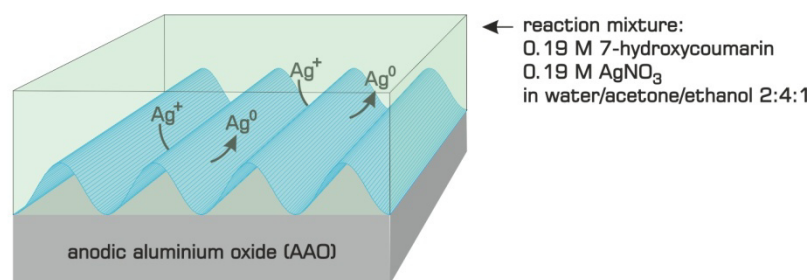
3.3.13: Principle of phtotochemical pattern formation by LIPSS

Photonic fringe patterns originating from the LIPSS phenomenon are utilized as a photochemical reaction template for the site-selective generation of Ag nanoparticles and their simultaneous fixation. The reaction is stimulated by a nanosecond pulsed laser operating at a wavelength of 355 nm. Excitation of 7-hydroxycoumarin by a 355 nm photon produces a phenoxy radical [43,44] which undergoes electron transfer reactions thus reducing present Ag^+ to Ag^0. The process also triggers polymerization [45] thus capturing Ag^0 in a polymer matrix (fig. 3.3.14).
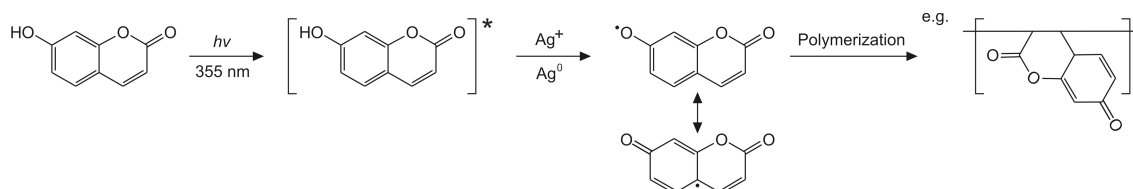
3.3.14: Reaction scheme of photochemically induced hybrid structure formation.

When lineary polarized laser pulses of appropriate energy vertically impinge into the interface between AAO and the reaction mixture, a photonic fringe pattern with a

periodicity in the range of the laser wavelength is formed. Photochemical reactions are preferably triggered in zones subjected to high fringe pattern intensity; hence, in these zones Ag^+ is rapidly reduced to Ag^0, which causes the concentration of Ag^+ to drop. This loss is compensated by diffusion of Ag^+ from less illuminated zones thus promoting Ag nanoparticle growth. Equally, 7-hydroxycoumarin is consumed by polymerization and fixes as-generated Ag nanoparticles in reaction zones. The overall process results in the formation of regular hybrid nanostructures as shown in fig. 3.3.15.
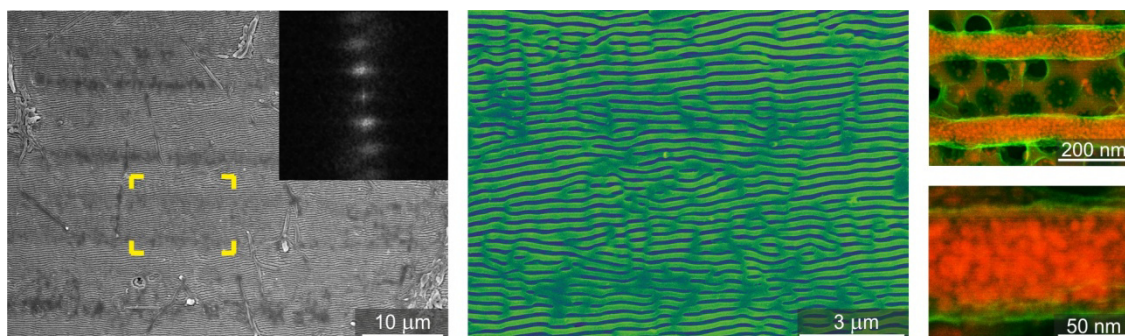
Fig. 3.3.15: Formation of regular hybrid nanostructures on AAO via LIPSS.
Long range ordered nanostructures are shown on the left. A magnification of the yellow marked section is shown in the center. Two pictures on the right visualize the hybrid nanostructures via dual sensor interpolation (SE/BSE). Ag nanoparticles are contrasted in red and the polymer matrix in green.

Pattern formation works well over extended surface areas. The periodicity of the ripples and the ripple width were measured to be about 285 nm and 133 nm, respectively. This is in good agreement with the expected periodicity of 264 nm which was calculated using the equation $\Lambda = \lambda \cdot [n \cdot (1 - sin\theta)]^{-1}$ under inclusion of the refractive index of water, which is 1.34 at 355 nm.[46-48] The structure of these hybrid patterns could be disclosed by backscattered electron imaging (BSE). Ag nanoparticles are visualized as bright red spots mainly located inside fiber-like jackets consisting of organic matter (green). Those organometallic hybrid nanowires resemble an array of parallel electrical conductors on an insulator (AAO). Macroscopic electrical conductivity measurements resulted in a resistance of about 8 kΩ along the ripple structure whereas a resistance exceeding 100 MΩ was found perpendicular to the ripple structure. Evidently, the formerly isolating AAO surface was functionalized with anisotropic conductivity.

The demonstrated concept breaks away former limitations of LIPSS-stimulated pattern formation by involving photochemistry into its portfolio of capabilities. This opens the door to laser-directed self-organization and reaction control in a vast variety of systems.

4   Conclusion and Outlook

Pulsed lasers proved to be advantageous tools for the stimulation of pattern formation in complex systems. Their capability to support thermodynamic, kinetic and spatial control facilitates the direction of self-organization processes into selective channels. The short lifetime of laser-stimulated processes was identified to be the key aspect that enables for the synthesis of functional materials starting from complex systems. When self-organization is abruptly stopped after a few nanoseconds, this creates materials present in a non-equilibrium state, which are known to exhibit special properties. A prominent example is the distinctively different behavior of gold nanoparticles compared to bulk gold. Repeated laser stimulation was demonstrated to be a powerful method that enables selective adjustments of material properties emergent in the course of self-organized pattern formation in complex systems. This includes a broad spectrum of optical, electrical, magnetic and catalytic properties, which are not found in the starting materials prior to laser modification. The capability of lasers to trigger self-organization processes with spatial control was identified to be an interesting feature because it bears the potential to create materials with advanced functionality. In particular, the utilization of a phenomenon called laser-induced periodic surface structures (LIPSS) proved to be very efficient. LIPSS transformed the surface of stainless steel into hierarchical structures thus equipping this everyday material with a multifunctional surface. Considering the simplicity of the generation process this demonstrates the viability of nature's low-effort-high-outcome-principle of order formation in complex systems. In addition to that, the application breath of laser-stimulated pattern formation was successfully expanded to temperature sensitive materials by including photochemistry into the concept. The large variety of reaction types accessible via photochemistry opens an even wider field of potential applications.

In conclusion, it can be stated that the concept of nature to trigger selective reorganizations and pattern formation in complex systems can be imitated in its principles. The introduced concept of laser-directed self-organization and reaction control in complex systems prospects a large application potential. Presented insights into laser-stimulated reaction pathways and pattern formations processes provide a

valuable basis for future studies in this field. Overall, the major challenge that must be met on the way to beneficial applications is the need for purposeful design of materials, which requires a thorough understanding of the fundamental principles behind self-organization.

# 5	Zusammenfassung und Ausblick

Pulslaser eignen sich hervorragend zur Stimulation von Musterbildung in komplexen Systemen. Ihr Potential thermodynamische, kinetische und spatiale Kontrolle gleichermaßen ausüben zu können ermöglicht die gezielte Steuerung von Selbstorganisationsprozessen. Die kurze Lebensdauer laserstimulierter Reorganisationen ist ein maßgeblicher Aspekt, der zur Generierung funktioneller Materialien durch Selbstorganisation in komplexen Systemen führt. Aufgrund des rapiden Wärmeflusses in den Volumenkörper werden laserstimulierte Oberflächenprozesse nach wenigen Nanosekunden abrupt beendet, was zur Bildung von Materialien führt, die im Nicht-Gleichgewichtszustand vorliegen. Solche Materialien besitzen spezielle Eigenschaften, die im Gleichgewichtszustand nicht auftreten. Ein prominentes Beispiel ist die starke Veränderung der Eigenschaften von Gold, sobald es in Form von Nanopartikeln vorliegt. Die schrittweise Reinitiierung von Selbstorganisationsprozessen durch erneute Laserstimulation erwies sich als ergiebige Methode zur Einstellung spezifischer Oberflächeneigenschaften, die aus unterschiedlichen Stadien der Musterreife hervorgehen. Eine breite Palette von optischen, elektrischen, magnetischen und katalytischen Eigenschaften kann auf diese Art und Weise erzeugt werden. Im Verlauf der Musterevolution tritt zudem ein Phänomen auf, das als *laser-induced periodic surface structures* (LIPSS) bekannt ist. Die dadurch hervorgerufene Erzeugung von hierarchischen Strukturen transformiert die Oberfläche von Edelstahl in ein multifunktionales Material mit attraktiven Eigenschaften. LIPSS kann relativ einfach auf diversen Oberflächen erzeugt werden und demonstriert damit die praktische Umsetzbarkeit des Prinzips der Natur mit geringem Aufwand großen Nutzen zu erzielen. Es konnte zudem gezeigt werden, dass sich LIPSS nicht nur zur photothermischen, sondern auch zur photochemischen Prozessführung einsetzen lässt. Dies erweitert zum einen den Anwendungsbereich laserinduzierter Musterbildungsprozesse auf temperaturempfindliche Materialien und eröffnet zum anderen die Möglichkeit, eine Vielzahl von photochemischen Reaktionstypen in laserinduzierten Selbstorganisationsprozessen zu nutzen.

Zusammenfassend kann festgestellt werden, dass grundlegende Prinzipien der natürlichen Musterbildung bis zu einem gewissen Grad nachgeahmt werden können. Das vorgestellte Konzept der laserdirigierten Selbstorganisation und Reaktionskontrolle in komplexen Systemen birgt großes Anwendungspotential. Einsichten in Prozesse, die zur Musterbildung in komplexen Systemen führen, stellen eine wertvolle Basis für zukünftige Studien dar. Bisher sind Selbstorganisationsprozesse aufgrund ihrer geringen Vorhersagbarbeit und Kontrollierbarkeit kaum in praktischer Anwendung zu finden. Das Gebiet muss entsprechend weiter beforscht werden, um dieses überzeugende Prinzip der Natur für technische Prozesse nutzbar zu machen.

6   Acknowledgements

First and foremost, I would like to thank Prof. Norbert Hampp, for providing me with an excellent atmosphere for doing research and for his guidance and support over the past years.

I deeply appreciate Prof. Bernd Harbrecht, for his support and contribution in my research and Clemens Pietzonka, for countless hours of magnetic measurements and data analyses.

My sincere thanks also go to Prof. Bernhard Roling, for providing access to special scientific equipment and to Dr. Julia Siebert-Krümpelmann, for her support in nanoelectrical surface examination.

Special thanks go to Dr. Hee-Cheol Kim, for many fruitful discussions, for teaching me to keep an open eye for details, and for being such a good friend.

I also give special thanks to all members of my workgroup, past and present, for a great time, amusing coffee breaks and not exclusively academic discussions.

My sincere thanks also go to all the department staff members for their help and support during my Ph.D. study. In particular, all workshop members shall be thanked for the great work they did.

Finally, I want to say thanks, from the bottom of my heart, to all my family members, and Katrin, for their love and encouragement in all my good and tough times throughout my life.

7   Bibliography

[1]   H. Krishna, N. Shirato, C. Favazzaa and R. Kalyanaraman
Phys. Chem. Chem. Phys. (11) 8136-8143, **2009.**

[2]   J. H. Weaver et al.
Fachinformationszentrum Karlsruhe, Physics Data, **1981**.

[3]   M. Fox
Optical Properties of Solids, Oxford, New York, **2001**.

[4]   W. S. Fann, R. Storz, H. W. K. Tom, J. Bokor
Phys. Rev. B (46) 13592-13595, **1992**.

[5]   J. A. F. Plateau, *Gauthiers-Villars*, Paris **1873**.
L. Rayleigh, *Philos. Mag*. (34) 145-154, **1892**.

[6]   J. D. Fowlkes, L. Kondic, J. Diez, Y. Wu, and P. D. Rack
Nano Lett. (11) 2478-2485, **2011**.

[7]   Jason Fowlkes, Scott Horton, Miguel Fuentes-Cabrera, and Philip D. Rack
Angew. Chem. (124) 8898-8902, **2012.**

[8]   S. Y. Chou, Q. F. Xia
Nat. Nanotechnol. (3) 369-369, **2008.**

[9]   A. Vrij
Discuss. Faraday Soc. (42) 23-27, **1966**.

[10] A. Vrij, J. T. G. Overbeek
J. Am. Chem. Soc. (90) 3074-3078, **1968.**

[11] A. Putnis
Introduction to mineral sciences, Cambridge University Press, **2008.**

[12] J. Bischof, D. Scherer, S. Herminghaus, P. Leiderer
Phys. Rev. Lett. (77) 1536-1539, **1996.**

[13] S. Herminghaus et al.
Science (282) 916.919, **1998.**

[14] C. Favazza, R. Kalyanaraman, and R. Sureshukumar
Nanotechnology (17) 4229-4234, **2006.**

[15] J. Trice, C. Favazza, D. Thomas, H. Garcia, R. Kalyanaraman, and R. Sureshkumar,
Phys. Rev. Lett., (101) 017802, **2008.**

[16] M. Birnbaum
J. Appl. Phys. (36) 3688-3689, **1965.**

[17]   D. C. Emmony, R. P. Howson L. J. Willis
        Appl. Phys. Lett. (23) 598-600,**1973.**

[18]   G. N. Maracas, G. L. Harris, C. A. Lee, R. A. McFarlane
        Applied Physics Letters (33) 453-455, **1978**.

[19]   N. R. Isenor
        Applied Physics Letters (31) 148-150, **1977.**

[20]   J. A. Van Vechten
        Solid State Communications (39) 1285, **1981.**

[21]   F. Keilmann, Y. H. Bai
        Applied Physics a-Materials Science & Processing (29) 9, **1982.**

[22]   J. E. Sipe, J. F. Young, J. S. Preston, H. M. van Driel
        Phys. Rev. B (27) 1141, **1983.**

[23]   J. F. Young, J. S. Preston, H. M. Van Driel and J. E. Sipe
        Phys. Rev. B (27) 1155, **1983.**

[24]   M. Oron, G. Sorensen
        Appl. Phys. Lett. (35) 782, **1979.**

[25]   K. Nishioka, S. Horita
        Appl. Phys. A, (91) 235-240, **2008.**

[26]   M. Rohloff, et al.
        Appl. Phys. (110) 014910-1-014910-4, **2011.**

[27]   K. Lou, S-X. Qian, Z-C. Ren, X-L. Wang, Y. Li, C. Tu, H-T. Wang
        J. Opt. Soc. Am. B (29) 2282-2287, **2012.**

[28]   J-T. Chen, W. C. Lai, Y. J. Kao, Y. Y. Yang, J. K. Sheu
        Opt. Express (20) 5689-5695, **2012.**

[29]   J. Z. P.Skolski et al.
        Phys. Rev. B (85) 075320-1-075320-9, **2012.**

[30]   J. F. Yong, J. S. Preston, H. M. van Driel, J. E. Sipe
        Phys. Rev. B, (27) 1155-1172, **1983.**

[31]   J. Vincenc Obona
        Appl. Surf. Sci. (258) 1555-1560, **2012.**

[32]   G. Miyaji, K. Miyazaki, K. Zhang, T. Yoshifuji, J. Fujita
        Opt. Express (20) 14848-14856, **2012.**

[33]   E. Rebollar et al.
        Langmuir (27) 5596-5606, **2011.**

[34] J. Bonse, A. Rosenfeld, and J. Krüger
      J. Appl. Phys. (106) 104910, **2009.**

[35] M. Huang, F. L. Zhao, Y. Cheng, N. Xu, and Z. Xu,
      ACS Nano (3) 4062, **2009.**

[36] J. F. Young, J. E. Sipe, and H. M. van Driel,
       Phys. Rev. B (30) 2001, **1984.**

[37] Jörn Bonse, Arkadi Rosenfeld and Jörg Krüger
      J. Appl. Phys. (106) 104910, **2009.**

[38] S. Höhm, A. Rosenfeld, J. Krüger, J. Bonse
      Applied Surface Science (278) 7-12, **2013.**

[39] J. Yang, J. Lian, Q. Dong, Z. Guo
      Applied Surface Science (229) 2–8, **2004.**

[40] D. R. Gaskell
      Introduction To The Thermodynamics Of Materials, 4th ed, **2003.**

[41] J. Yang, J. Lian, Q. Dong, Z. Guo
      Appl. Surf. Sci. (229) 2-8, **2004.**

[42] A. S. C. M. d'Oliveira, R. S. C. Paredes, F. P. Weber, R. Vilar
      Materials Research (4) 93-96, **2001.**

[43] Y. Chen , K.-H. Chen
      J. Polym. Sci. Part A: Polym. Chem. (35) 613-624, **1997.**

[44] S. Härtner, H.-C. Kim, N. Hampp
      J. Photochem. Photobiol. A: Chemistry (187) 242-246, **2007.**

[45] A. Z. Abyshev , S. S. Krylov
      Chem. Nat. Compd. (20) 35-39, **1984.**

[46] J. Siegel et al.
      Appl. Surf. Sci. (256) 2205-2209, **2010.**

[47] E. Rebollar et al.
      Langmuir (27) 5596-5606, **2011.**

[48] K. Nishioka, S. Horita
      Appl. Phys. A (91) 235-240, **2008.**

8   Publications

A   Laser-Directed Self-Organization and Reaction Control in Complex Systems - A Facile Synthesis Route for Functional Materials.

Hendrik M. Reinhardt, Clemens Pietzonka, Bernd Harbrecht, Norbert Hampp

submitted

B   Self-Organization of Multifunctional Surfaces - The Fingerprints of Light on a Complex System.

Hendrik M. Reinhardt, Hee-Cheol Kim, Clemens Pietzonka, Julia Krümpelmann, Bernd Harbrecht, Bernhard Roling, Norbert Hampp

Adv. Mater. (25) 3257, **2013.** DOI: 10.1002/adma.201370155

C   Photochemical Preparation of Sub-Wavelength Heterogeneous Laser-Induced Periodic Surface Structures.

Hee-Cheol Kim, Hendrik M. Reinhardt, Pierre Hillebrecht, Norbert Hampp

Adv. Mater. (24) 1994, **2012.** DOI: 10.1002/adma.201200534

D   Transformation of anodic aluminum oxide to nanoporous α-Al_2O_3, Ruby and Ti-sapphire micropatterns.

Hendrik M. Reinhardt, Hee-Cheol Kim, Norbert A. Hampp

*JECS* (33) 1281, **2013.** DOI: 10.1016/j.jeurceramsoc.2013.01.005

Laser-Directed Self-Organization and Reaction Control in Complex Systems –

A Facile Synthesis Route for Functional Materials

Hendrik M. Reinhardt[1], Clemens Pietzonka[1], Bernd Harbrecht[1,2], Norbert Hampp[1,2]*

[1] Department of Chemistry, Philipps-University of Marburg
   Hans-Meerwein-Str., 35032 Marburg, Germany
[2] Material Science Center, 35032 Marburg, Germany

In recent years, the principles of nanostructure formation via pulsed-laser-induced dewetting (PLiD) were extensively studied. Here we demonstrate the potential of PLiD for order formation and reaction control in systems that contain a plurality of components and reactive species. Higher system complexity facilitates additional transformations such as phase separations, segregations and texture formation to occur beyond nanostructure formation. A versatile bottom-up concept for synthesis and tuning of functional materials is introduced.
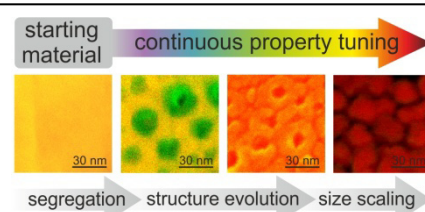
Self-organization provides great opportunities for simple and cost-efficient fabrication of nanomaterials and is therefore a key technology for beneficial implementations of nanoscience.[1,2] Dewetting phenomena belong to a class of self-organization processes that rely on the concept of nature to trigger system reorganizations by a specific stimulus.[3-9] In recent years, pulsed-laser-induced dewetting (PLiD) attracted considerable attention as it facilitates controlled nanostructure formation starting from diverse precursor materials.[10-12] PLiD is based on rapid thermal cycling of surfaces by subjecting those to extreme heating and cooling rates of up to 10^{10} K/s.[13] The initial stimulus for self-organization is surface liquefaction by an intense laser pulse. Striving for a more favorable state of energy, liquefied thin-films encounter Rayleigh-Plateau instability and undergo spinodal dewetting. A certain combination of driving forces eventually leads to ruptures in the films thus initiating a fast progressing scenario of nucleation, particle formation and ripening.[14-16] Diverse states of structure maturity are traversed in a few nanoseconds until one is captured in a metastable state due to rapid resolidification.[17] The basic principles behind PLiD-stimulated nanostructure formation were thoroughly investigated in recent years. Studies on well defined reaction systems like patterned metallic thin films provided deep insights into the physics behind PLiD-stimulated self-organization.[13,18-23] Anyway, nature`s concept of self-organization is essentially characterized by a low-effort, high outcome principle that leads to order formation in systems that contain a plurality of reactive species. Consequently, it is an interesting question whether PLiD provides order formation in systems of higher complexity as well. Increasing numbers of reactive species enlarge the degrees of freedom in a system and thus the pool of potential reaction pathways. This opens the opportunity to create advanced materials provided that a tool is available that channels those reactions into useful directions. Using the example of a well known composite, this study demonstrates the potential of PLiD for order formation and reaction control in complex systems.

Our model system, stainless steel type EN 1.4301 (AISI 304), is a widely employed and well-investigated construction material. The alloy contains three transition metals, one half-metal and several trace elements. Its mayor alloying elements are Fe (69 wt%), Cr (18 wt%) and Ni (10 wt%) but it also contains Mn (2 wt%), Si (1 wt%), N (<0.1 wt%), C (<0.07 wt%), and S (<0,015 wt%). The model system was triggered by laser pulses in the nanosecond time domain. A single laser pulse delivered an optical fluence of ø = 2.88 J/cm^2 to the surface, thus heating the outmost layer of stainless steel to liquefaction. Consecutive chemical reactions and structure formation processes rapidly cease due to supercooling and resolidification. At a given pulse frequency of 30 kHz this event, in the following abbreviated as dewetting cycle (DC), repeats every 33 µs. The impact of sequential photo-thermal stimuli on the surface properties of stainless steel was screened in a range from 0 to 589 DC (see **Supporting Information 1**). Using a set of 24 samples, this approach provides profound insights into the mechanisms of laser-directed order formation and reaction control in a complex system. In order to illustrate these findings in a more general way we narrowed the presentation of system-specific features to essentials. Details are provided in the **Supporting Information**.

As an introduction to the subject, the effects of PLiD to the crystalline structure of stainless steel are presented because this is a prerequisite for later contents of this study. PLiD modifications induce changes in the crystalline structure of EN 1.4301 that are traceable by X-ray diffraction analyses (XPD). **Fig. 1a** illustrates a combined plot of diffraction patterns obtained from the sample set. Distinct peak intensity shifts and peak broadenings indicate sequential transformations of the formerly microcrystalline structure of virgin stainless steel (DC = 0) into a highly textured nanocrystalline structure. TEM images visualize these structural changes exemplarily (**Fig. 1b**). Beyond size scaling effects, a phase separation is observed in steel samples subjected to PLiD treatments exceeding 30 DC. The face centered cubic phase (fcc), which is typically found in austenitic steels like EN 1.4301, is intermixed with a body centered cubic phase (bcc) characterized by emerging peaks at 44.42 ± 0.01 ° $2\theta_{CuK\alpha}$ (**Supporting Information 2**). Pronounced intensity gains of fcc-111- and bcc-110-peaks illustrate a course of texture evolution that is characterized by mutual interactions between both phases (**Fig. 1c**). A strong influence of bcc phase segregation to fcc texture development is obvious. The fcc-phase shows maximum texture expression after 165 DC while texture formation in the bcc phase is less
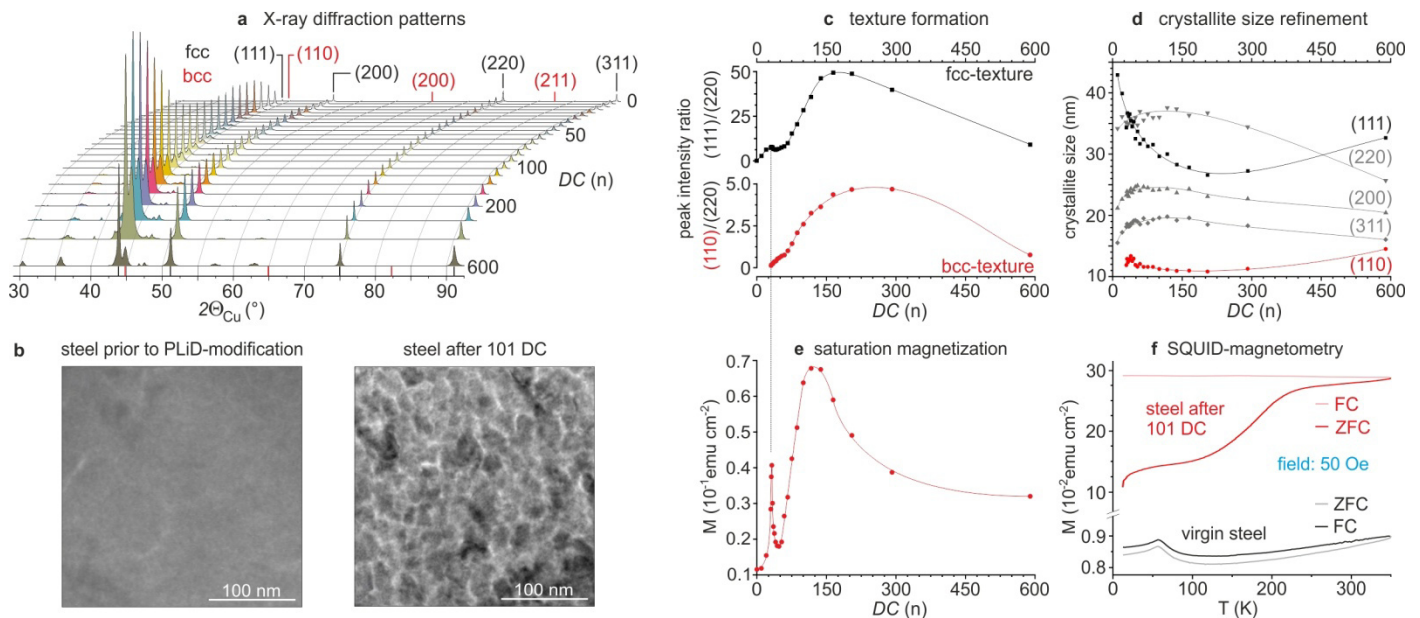
Figure 1. Crystal structure analysis and magnetic characterization of PLiD-modified stainless steel
(a) Waterfall plot of X-ray diffraction patterns obtained from the set of 24 steel samples sequentially subjected to increasing numbers (n) of dewetting cycles (DC). The diffraction pattern of untreated steel is given for comparison at DC = 0. Miller indices for the fcc-phase (face-centered cubic) and the bcc-phase (body-centered cubic) are indicated at the top. **(b)** TEM images show the grain structure in stainless steel prior and after PLiD modification. **(c)** DC-dependent texture formation in steel illustrated by peak intensity ratios of fcc-(111) and bcc-(110) in relation to fcc-(220). **(d)** DC-dependent crystallite size refinement in stainless steel determined using the Scherrer equation. See **Supporting Information 2 and 3** for details about crystal structure analyses. **(e)** DC-dependent saturation magnetization of stainless steel measured by SQUID-magnetometry. The degree of magnetization is taken as an indicator for the amount of PLiD-induced bcc-precipitates. **(f)** Comparison between magnetic characteristics of untreated and PLiD-modified steel. ZFC-FC measurements at a low field of 50 Oe (SQUID) show that untreated steel behaves similar to a Pauli paramagnet which orders antiferromagnetically at appr. 60 K. In contrast to that, PLiD-modified steel features sharply enhanced magnetization that decreases with temperature. More details about magnetic characteristics are provided in **Supporting Information S4**.
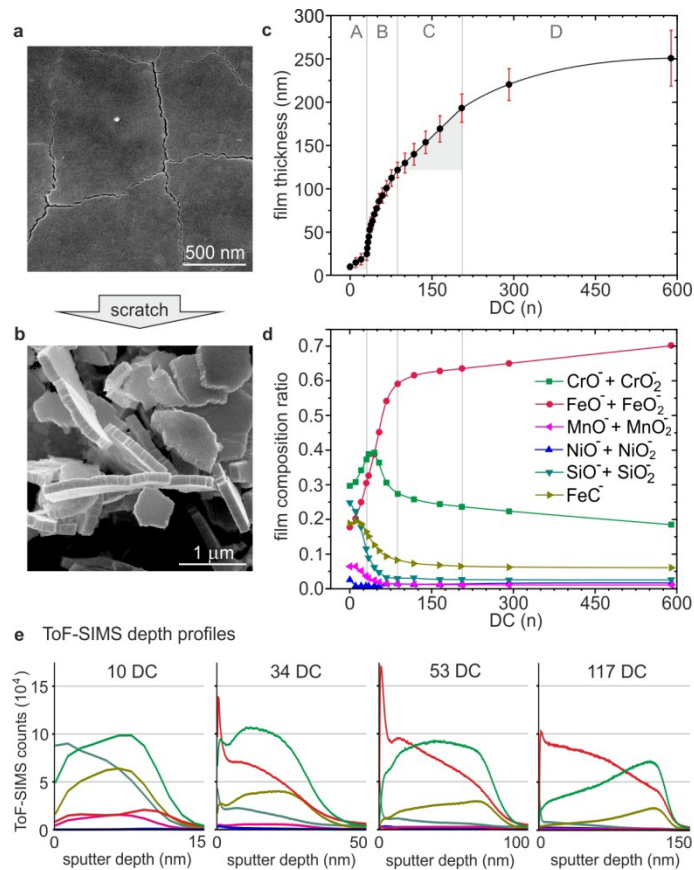
pronounced but clearly evident and peaking between 200 and 300 DC. Texture formation in metals is commonly accepted to vector of laser induced heat which rapidly diffuses from the surface of stainless steel into the bulk. Repeated thermal cycling leads to stepwise optimization of oriented crystal growth and thus texture evolution. As the declines of texture quality starting at 200 DC show, this optimization is not progressing unlimited. The effect is supposed to be a consequence of nanocrystallite recombination due to excessive thermal cycling. Crystallite size determinations using the Scherrer equation support this assumption **(Fig. 1d)**. Minimum crystallite sizes are detected in the very same DC range where maximum texture quality is found, whereas the decline of texture quality is accompanied by an increase of crystallite size. Another peculiarity in PLiD-modified steel is the finding that bcc and fcc phases show significant differences regarding their crystallite sizes. While fcc nanocrystallites cover a size range of 15 to 43 nm the bcc phase features smaller crystals with a narrow size distribution ranging from 11 to 14 nm. These size deviations are caused by cooling rate variations during PLiD-stimulated nanocrystal formation. Recursion to Yang`s results concerning cooling rate dependent grain size refinement in stainless steels suggests cooling rates of $10^6 - 10^7$ K s^{-1} to be necessary for nanocrystal formation in the size range of 15 –43 nm.[24] Even faster cooling rates of about 10^8 K s^{-1} lead to nanocrystal formation in the size range determined is supposed to be a consequence of bcc to fcc retransformation due to thermal equilibration. Interestingly, the course of PLiD-induced magnetization shows an additional peak at 33 DC. This singularity is attributed to a phenomenon named Laser-induced Periodic Surface Structures (LIPSS). LIPSS generation is the result of a feedback mechanism between light and matter that occurs under certain conditions of laser irradiation which lie hidden in the PLiD parameter space. Beyond other interesting effects, LIPSS generates regular

be a result of oriented crystal growth along a vector of heat diffusion. In the present case crystal growth is directed by the for the bcc-phase. It can thus be stated that bcc crystals originate from an earlier stage of structure maturity than fcc crystals. This can be understood by the fact that bcc is the initial phase that occurs at the solidification contour of austenitic steel melts.[25] The fact that bcc to fcc transformation is a diffusion process and thus time dependent makes this phase separation accessible for processes that control liquid lifetimes on the nanosecond time scale. Obviously, cooling rates that occur during a PLiD cycle are too fast for a complete retransformation into the thermodynamically favored fcc-phase, thus capturing bcc intermediates in a non-equilibrium state. In general, the results of crystal structure analysis show that phase separation and texture formation are additional transformations accessible by PLiD beyond nanostructure formation. Depending on the precursor system, phase separations offer the potential to enrich the pool of controllable material characteristics. In the present example PLiD-induced bcc precipitation provides magnetic tuning of stainless steel **(Fig 1e)**. Incorporations of bcc-nanocrystals transform the formerly paramagnetic steel into a ferromagnetic material **(Fig. 1f)**. The stepwise increase of saturation magnetization reaches its maximum between 100 and 150 DC. Similar to the loss of texture quality, excessive thermal cycling was found to reduce the saturation magnetization of PLiD-modified steel. The effect patterns of bcc-precipitates in stainless steel, thus equipping the material with a magnetically patterned surface **(Supporting information 5)**. Details concerning the effects of LIPSS to stainless steel are covered elsewhere.[26]

Now that structural transformations in stainless steel are exposed, the question to which extent PLiD enables control of chemical reactions in a complex system is evaluated. By the fact that all PLiD modifications of stainless steel were performed in ambient air, reactions between steel components

and oxygen are to be expected. As illustrated in **Fig. 2a**, products of such reactions cover the surface of stainless steel in the form of ceramic films or rather mosaic-like platelets. Even though these platelets feature excellent adhesion to the substrate, plastic deformation of the underlying steel causes exfoliation **(Fig. 2b)**. The procedure was utilized for systematic cross section analyses yielding a film thickness assay of the sample set. Plotting film thickness versus DC **(Fig. 2c)** gives a steady growth function with zones of different slope labeled A-D. Zone A is characterized by a linear thickening of stainless


Figure 2. Characterization of PLiD-generated ceramic thin films on stainless steel
(a) Plane view SEM inspection of a steel surface resulting from PLiD modification using 101 DC. (b) The same thin film exfoliated from the underlying steel by mechanical deformation. (c) Film thicknesses of all samples determined by thin film cross section survey. Failure bars indicate statistical variations in thin film thickness. The DC-dependent increase of film thickness shows different slope characteristica sectioned in A-D. Slopes: A = 0.5 nm DC^{-1} (linear), B ~ 1 nm DC^{-1} (nonlinear), C = 0.6 nm DC^{-1} (linear), D ~ 0.15 nm DC^{-1} (nonlinear, saturation) (d) DC-dependent chemical segregation scenario in thin films analyzed by Time-of-Flight Secondary-Ion-Mass-Spectrometry (ToF-SIMS). ToF-SIMS depth profiles of 14 PLiD-modified steel samples were extracted and combined to this overview scheme. Mass fragments indicating chemical species are given in the legend. (e) A selection of ToF-SIMS depth profiles showing gradual transformation of layering structures in PLiD-generated thin films. More information about ToF-SIMS analyses and the theoretical background of metal-oxide segregation is provided in **Supporting Information S6**.

steel`s natural passivation film (about 10 nm thickness) with a slope of 0.5 nm DC^{-1}. Exceeding 30 DC (zone B) a sudden change to nonlinear film growth with averaged slopes of 1 nm DC^{-1} is observed. In zone C the growth rate returns to a slope similar to that observed in zone A and finally falls into saturation for DC > 200 (Zone D). The results show that film thicknesses in a range between 10 and 250 nm are freely adjustable by PLiD. Besides these quantitative aspects of surface oxidation the composition of PLiD-generated oxide films was analyzed by Time-of-Flight Secondary-Ion-Mass-Spectrometry (ToF-SIMS). Compositional screenings of the

sample set reveal a DC-dependent segregation scenario in PLiD-generated ceramic thin films **(Fig. 2d)**. Prior to laser treatment stainless steel is covered by a natural passivation film composed of Cr- and Si-oxides to the most part. Even small numbers of PLiD cycles (< 30 DC) induce explicit shifts in the composition ratio. Cr- and Fe-oxide contents gradually increase while Si-, Mn- and Ni-oxides are more and more diminished. At 48 DC the thin film enrichment with Cr-oxide passes its maximum, while Si-, Mn- and Ni-oxide contents fall into a minimum. PLiD modifications exceeding 48 DC successively promote Fe-oxide accumulation, thus eventually inverting the former layering structure. As the DC-dependent evolution of thin-film layering structures indicates **(Fig. 2e)**, this inversion process is driven by a pervasive stream of thermally activated iron-species towards oxidation sites. The overall oxide segregation scenario can be understood from a thermodynamic point of view. Regarding free Gibbs energies of oxide formation, Si features the highest affinity to oxygen and Ni the lowest. Even though Si belongs to the minor alloying elements (1 wt%) its scavenges oxygen much more efficiently than any other element contained in stainless steel. The observed course of thin film composition indicates a strong influence of the thermodynamic reactivity sequence Si>Mn>Cr>>Fe>Ni on the metal oxide segregation scenario (see **Supporting Information 6** for details). Adherence to this sequence results from the fact that thin film growth is governed by oxygen deficiency, as indicated by Fe-carbide contents observed in all ceramic films **(Fig. 2d, e)**. Increasing numbers of DC initially result in progressive oxidation of Si and Mn according to the given reactivity sequence. The Cr-oxide ratio rises not until those minor alloying elements suffer local depletion. Although Cr is the major alloying element (18 wt%) of stainless steel, its feedstock in the laser affected zone is still limited. Consequently, Fe is more and more oxidized for DC numbers exceeding 48 because Cr subsequently depletes. As the basic component of steel Fe virtually never depletes, thus leaving low reactive Ni in a nearly unoxidized state. In conclusion it can be stated that the observed oxide segregation scenario is in good compliance to thermodynamic expectations. A result like this could not be assumed necessarily because PLiD-stimulated reactions proceed under non-equilibrium conditions, as the before mentioned phase separation shows. Anyway, this finding opens the opportunity to predict the course of PLiD-induced oxide segregation for other precursor systems thus paving the way to custom tailored nanocomposite synthesis. A large variety of readily available composite materials and processing conditions make this approach very flexible and practicable.

So far we demonstrated that PLiD generates metal-oxide thin films with transversally graded composition. However, the finding that PLiD gives control over the lateral composition as well is even more interesting. PLiD-generated metal oxide composites are essentially no films but rather densely packed arrays of nanostructures. Four basic structural motifs can be distinguished **(Fig. 3a)**: PLiD modifications up to 30 DC solely induce changes in the layering structure of stainless steel`s natural passivation film. Exceeding 30-44 DC PLiD-generated nanocomposites also exhibit lateral inhomogeneities in composition beyond transversal grading. This is especially true for PLiD modifications exceeding 44 DC. Such conditions initially produce core-shell nanostructures that finally merge into a motif of closely spaced nanoparticles when a threshold of 87 DC is overrun. Cross sectional SEM views **(Fig. 3b)** show that both motifs (III and IV) actually represent arrays of vertically aligned nanorods with aspect ratios ranging between
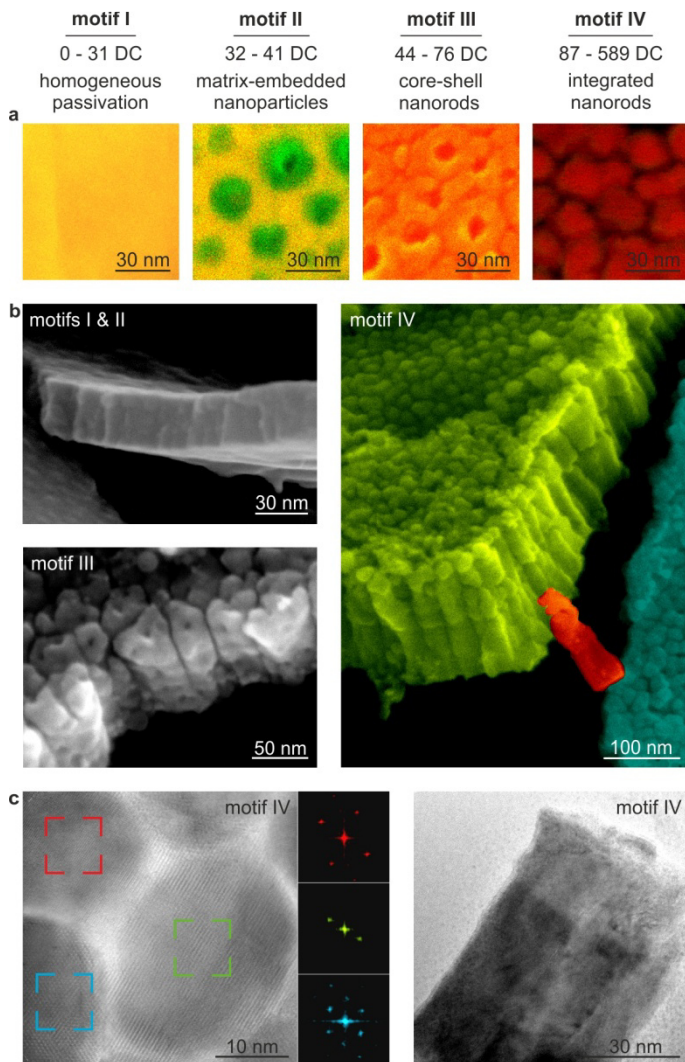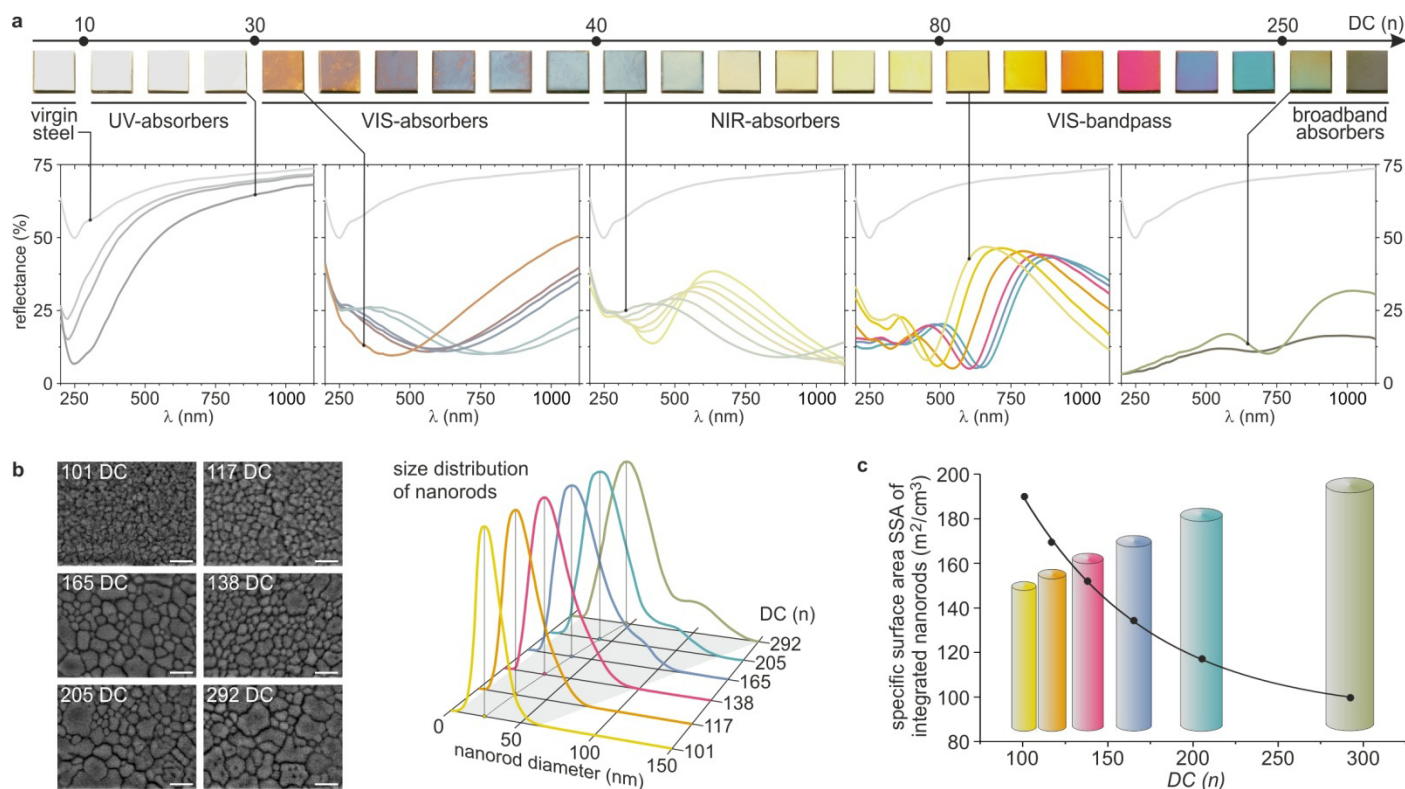
Figure 3. Nanostructures in PLiD-generated oxide scales
(a) SEM plane views on typical structure motifs of thin films generated in four different DC ranges. The coloration is a result of dual sensor interpolation (SE/BSE). The secondary electron detector (SE) visualizes purely morphological aspects (green), whereas the backscattered electron detector (BSE) supports material-specific information (red). The contrast scales with the effective atomic number Z_{eff} of materials. The higher Z_{eff} the higher the backscattering efficiency. **(b)** SEM views (SE detector) on breaking edges of thin films representing motifs I - IV. Motif I and motif II are characterized by densely packed or rather monolithic films without distinctive morphological features. In contrast to that, motif III comprises assemblies of closely packed and upright core-shell nanostructures. Motif IV dominantly presents integrated structures of vertically alligned nanorods. The picture was colored to highlight individual entities. **(c)** TEM inspections of motif IV nanorods. The left picture shows a plane view of a nanorod-array. Fast Fourier transformations (insets) visualize different lattice orientations for each nanorod. The right picture shows a cross sectional view on a nanorod agglomerate comprising 2-3 entities. Gray scales on nanorod edges indicate that the layering structure analyzed by ToF-SIMS is manifest in each entity

2 and 8. The arrays comprise individual building blocks that can be separated from one another. Moreover, fast Fourier transformations on the basis of TEM lattices images prove that adjacent nanorods represent individual crystalline domains **(Fig. 3c)**. Staged gray scales in the cross sectional transmission image of motif IV nanorods visualize that transversal composition gradients are manifest in each building block. Integrated structures of such complexity and order are sought-after materials because they provide special physico-chemical properties that are promising for a variety of applications. Nanocomposites built from transition metal oxides (TMOs) are of special interest because TMOs belong to the most diverse and richest classes of materials in terms of optical, electrical, thermal, magnetic and catalytic properties. Their properties

originate essentially from d-d electronic transitions between lower t_{2g} and higher e_g levels in fivefold degenerated 3d orbitals. The bandwidths of such transitions are usually large due to strong electronic coupling to vibrations of the local environment. Even marginal variations of parameters like oxidation state, stoichiometry, crystallinity, density, morphology or particle size, dispersity and shape result in alterations of their electronic structure.[27] The potential of PLiD to affect such parameters was demonstrated by means of structural and compositional transformations in TMO nanocomposites on stainless steel. Consequently, changes in their electronic structure are to be expected. A sensitive probe for such amendments is optical spectroscopy, but this technique is initially not required to observe PLiD-stimulated changes. Visual inspection of the sample set **(Fig 4a)** guides the eye to a series of vivid colors generated by PLiD treatments in the range from 80 to 205 DC. Apart from that, the majority of modifications are less eye-catching but by no means less interesting. Integrating sphere measurements reveal a wide variety of optical diversity that covers the spectral range from ultraviolet (UV) to near-infrared (NIR). The suspicion that these optical effects might be a result of thin film interference can be refuted by angle dependent measurements along with other evidence (see **Supporting Information 7**). Consequently, this diversity must originate from specific combinations of compositional and structural aspects that alter the electronic structure of TMOs. While optical characteristics of UV-absorbers primarily result from PLiD-induced thin film thickening, those of VIS- (visual spectrum) and NIR-absorbers are increasingly influenced by structural peculiarities like matrix embedded nanoparticles and core-shell-nanorods **(cp. Fig. 3a, motifs II, III)**. Such incorporations act as interfaces in an initially rather homogeneous material thus creating quantum confinement effects and two-dimensional electron gases which are known to exhibit unusual electronic structures.[28-30] The effect of interfaces to the optical properties of TMO nanocomposites can best be illustrated on the examples of VIS-bandpass and broadband absorbers. Considering that the composition of this motif IV structures remains nearly constant **(cp. Fig. 2d, zones C and D)**, their spectral diversity must originate almost completely from differences in nanorod size distribution **(Fig. 4b)**. Calculations based on nanorod size distributions yielded an exponential dependency between the numbers of DC applied to the substrate and the specific surface area (SSA) of nanorods interfaces created within the oxide matrix **(Fig. 4c)**. This provides insights into the laser directed self-organization process on the one hand and demonstrates the impact of oxide interfaces to the electronic structure of TMO nanocomposites on the other hand. Size scaling of nanoparticles by PLiD is not essentially novel. However, the generation and scaling of vertically aligned nanostructures with anisotropic composition and shape was, to our knowledge, never reported before. The mechanism of structure formation can be understood as a template assisted oxidation process. As demonstrated in the first section, PLiD treatments transform the surface of stainless steel into a nanocrystalline and textured material. In each PLiD cycle the surface of this nanostructured template is simultaneously oxidized to some extent, thus replicating its texture more and more into vertically aligned metal-oxide nanostructures. The model of template assisted oxide formation is supported by good dimensional correlation between PLiD-generated nanocrystallites in stainless steel **(cp. Fig. 1b, d)** and metal oxide nanostructures found on its surface.

Figure 4. Optical properties of PLiD-generated oxide nanostructures
(a) DC-dependent changes of stainless steel`s optical properties. Pictures of all 24 steel samples are given at the top. The sample reffered to as virgin steel represents a mirror polished steel sheet (10 x 10 x 0.8 mm) prior to PLiD modification (DC = 0). Integrating sphere measurements of all samples are given below. A spectrum of virgin steel accompanies all spectra as a reference. The spectra are color coded with respect to the visual appearance of each sample. **(b)** Size distributions of nanorod diameters for samples modified in the DC range from 101 to 292 (color coded). SEM plane views visualize corresponding motif IV nanorod-arrays; the scale bar is 100 nm. **(c)** Selective surface area (SSA) of integrated nanorods versus DC (calculations are based on nanorod size distributons). SSA decreases exponentially with increasing DC. Averaged dimensions of typical nanorods are sketched for comparative purpose. More information concerning optical properties of PLiD-modified stainless steel is provided in **Supporting Information S7**.

In conclusion it can be stated that PLiD is a powerful tool for order formation and reaction control in complex systems. The materials makes the introduced concept attractive for application. PLiD-stimulated oxide segregations were found to proceed in compliance to thermodynamic expectations. This gives a basis for prediction of PLiD-induced segregation processes thus paving the way for targeted synthesis of tailored nanocomposites by means of precursor adaption. Accessible effects like phase separation and texture formation expand the pool of opportunities for specific nanocomposite design additionally. The demonstrated ability of PLiD for interface formation in oxide materials is of special interest, as emergent phenomena in two-dimensional electron gases located at oxide interfaces include superconductivity, exceptional carrier mobility, fractional quantum hall effect and beyond.[31-34] In recent years, structured nanocomposites become increasingly important as platforms for detection and sensing, energy harvesting and storage, data storage, and biomedical applications, to name a few.[35-39]

EXPERIMENTAL METHODS
Stainless steel type EN 1.4301 (AISI 304), a non-magnetic austenitic alloy with a composition of Fe (69 wt%), Cr (18 wt%), Ni (10 wt%), Mn (2 wt%), Si (1 wt%), N (<0.1 wt%), C (<0.07 wt%), and S (<0,015 wt%) was used in this study. Steel sheets of 0.8 mm thickness were cut into adequate dimensions for respective measurements and polished to a root mean square roughness of $R_{RMS} < 25$ nm.
Surface modifications of stainless steel were stimulated by a Nd:YVO$_4$ DPSS nanosecond pulsed laser (Vector 532-1000-20, Coherent, USA). Details concerning experimental design are provided in **Supporting Information 1**.

potential for controlled synthesis of nanostructured composites starting from inexpensive and readily available precursor Scanning electron microscopy (SEM) was performed on a field emission microscope (JSM-7500F, Jeol, Japan) equipped with a backscattered electron detector (YAG, Autrata, Czech Republic) for material contrast imaging by means of effective atomic number contrast Z_{eff}. In order to improve the visualization of nanostructures like vertically aligned nanorods, respective samples were etched in an aqueous solution of 1 M H$_2$SO$_4$ for 1-2 hours prior to SEM-inspection.
Transition electron microscopy (TEM) of exfoliated ceramic thin films was performed on a JEM 3010 (Jeol, Japan). Images were captured by a Gatan 2kp x 2kp CCD camera and analyzed with Digital Micrograph.
Crystal structure analysis of PLiD-modified stainless steel samples were performed on a Philips X`Pert PRO MPD powder diffractometer (XPD) equipped with X`Pert tube Cu LFF operating at 40 kV and 40 mA. Spectra were obtained in the $20° \leq 2\theta \leq 92°$ range at room-temperature. X`Pert High Score Plus v2.2c and Origin Pro 8 were used for data processing and analysis; see **Supporting Information 2 and 3** for details)
Magnetic characterizations of unmodified and PLiD-modified stainless steel samples were performed on a superconducting quantum interference device (DC-SQUID, Quantum Design, USA). **Supporting Information 4** provides details about analytical procedures.
Optical spectroscopy was performed on a PerkinElmer Lambda 35 UV-VIS-NIR spectrometer equipped with integrating sphere C6951014 for surface characterization.
Time-of-Flight Secondary-Ion-Mass-Spectrometry (ToF-SIMS[4], Ion-Tof, Germany) was employed to study the effects

of PLiD to the chemical composition of ceramic thin films on stainless steel. In order to review the course of chemical alterations we conducted compositional depth profiling of 14 samples, each modified with different numbers of dewetting cycles in the range between 0 and 598 DC. Layer-by-layer ablation of ceramic thin films by a scanned antimony-ion-beam coupled with simultaneous mass spectrometry of ejected fragments yielded transversal composition profiles with nanometer depth resolution. A discussion concerning the theoretical background of PLiD-induced oxide segregation is given in **Supporting Information 6**.

1 Corté, L.; Chaikin, P. M.; Gollub, J. P.; Pine, D. J. *Nature Physics* **2008**, *4*, 420-424. DOI: 10.1038/nphys891
2 Ben-Jacob, E. *Nature* **2002**, *415*, 370. DOI: 10.1038/415370a
3 Huang, J.; Kim, F.; Tao, A. R.; Connor, S.; Yang, P. *Nature Mater.* **2005**, *4*, 896-900. DOI: 10.1038/nmat1517 2005
4 Becker, J.; Grün, G.; Seemann, R.; Mantz, H.; Jacobs, K.; Mecke, K. R.; Blossey, R. *Nature Mater.* **2003**, *2*, 59-63. DOI: 10.1038/nmat788
5 Berne, B. J.; Weeks, J. D.; Zhou, R. *Annu Rev. Phys. Chem.* **2009**, *60*, 85-103. DOI: 10.1146/annurev.physchem.58.032806.104445
6 Botiz, I.; Freyberg, P.; Stingelin, N.; Yang, A. C-M.; Reiter G. *Macromolecules* **2013**, *46*, 2352-2356. DOI: 10.1021/ma400120z
7 Xu, L.; Reiter, G.; Shi, T.; An, L. *Langmuir* **2010**, *26*, 7270-7276. DOI: 10.1021/la904420d
8 Péron, N.; Brochard-Wyart, F.; Duval, H. *Langmuir* **2012**, *28*, 15844-15852. DOI: 10.1021/la303374m
9 Mukherjee, R.; Das, S.; Das, A.; Sharma, S. K.; Raychaudhuri, A. K.; Sharma, A. *ACS Nano* **2010**, *4*, 3709-3724. DOI: 10.1021/nn901912d
10 Tan, K. W.; Saba, S. A.; Arora, H.; Thompson, M. O.; Wiesner, U. *ACS Nano* **2011**, *5*, 7960-7966. DOI: 10.1021/nn2023446
11 Roberts, N. A.; Fowlkes, J. D.; Mahady, K.; Afkhami, S.; Kondic, L.; Rack, P. D. *ACS Appl. Mater. Interfaces* **2013**, 5, 4450-4456. DOI: 10.1021/am400925h
12 Krishna, H.; Shirato, N.; Favazza, C.; Kalyanaraman, R. *J. of Materials Research* **2011**, *26*, 154-169. DOI: 10.1557/jmr.2010.17
13 Fowlkes, J. D.; Kondic, L.; Diez, J.; Wu, Y.; Rack, P. D. *Nano Lett.* **2011**, *11*, 2478-2485. DOI: 10.1021/nl200921c
14 Rayleigh, L. *Philos. Mag.* **1892**, *34*, 145-154.
15 Plateau, J. A. F. Statique expérimentale et théorique des liquides soumis aux seules forces moléculaires, *Gauthiers-Villars*, Paris **1873**.
16 Krishna, H.; Shirato, N.; Favazza, C.; Kalyanaraman, R. *Phys. Chem. Chem. Phys.* **2009**, *11*, 8136-8143.DOI: 10.1039/b906281p
17 McKeown, J. T.; Roberts, N. A.; Fowlkes, J. D.; Wu, Y.; LaGrange, T.; Reed, B. W.; Campbell, G. H.; Rack, P. D. *Langmuir* **2012**, *28*, 17168-17175. DOI: 10.1021/la303657e
18 Fowlkes, J. D.; Kondic, L.; Diez, J.; Wu, Y.; Rack, P. D. *Nano Lett.* **2011**, *11*, 2478-2485. DOI: 10.1021/nl200921c
19 Krishna, H.; Shirato, N.; Yadavali, S.; Sachan, R.; Strader, J.; Kalyanaraman, R. *ACS Nano* **2011**, *5*, 470-476. DOI:10.1021/nn1022632
20 Fowlkes, J. D.; Wu, Y.; Rack, P. D. *ACS Appl. Mater. Interfaces* **2010**, *2*, 2153-2161. DOI: 10.1021/am100417x
21 Wu, Y.; Fowlkes, J. D.; Rack, P. D.; Diez, J. A.; Kondic, L. *Langmuir* **2010**, *26*, 11972-11979. DOI: 10.1021/la1013818
22 Fuentes-Cabrera, M.; Rhodes, B. H.; Baskes, M. I.; Terrones, H.; Fowlkes, J. D.; Simpson, M. L.; Rack, P. D. *ACS Nano* **2011**, *5*, 7130-7136. DOI:10.1021/nn2018254
23 Wu, Y.; Fowlkes, J. D.; Roberts, N. A., Diez, J. A.; Kondic, L.; González, A. G.; Rack, P. D. *Langmuir* **2011**, *27*, 13314–13323. DOI: 10.1021/la203165v
24 Yang, J.; Lian, J.; Dong, Q.; Guo, Z.; *Appl. Surf. Sci.* **2004**, *229*, 2-8. DOI: 10.1016/j.apsusc.2004.01.054
25 d'Oliveira, A. S. C. M.; Paredes, R. S. C.; Weber, F. P.; Vilar, R. *Materials Research* **2001**, *4*, 93-96. DOI: 10.1590/S1516-14392001000200009
26 Reinhardt, H.; Kim, H-C.; Pietzonka, C.; Kruempelmann, J.; Harbrecht, B.; Roling, B.; Hampp, N. *Adv. Mat.* **2013**, DOI: 10.1002/adma.201205031.
27 Vayssieres, L. *Int. J. of Nanotechnology* **2004**, *1*, 1-41. DOI: 10.1504/IJNT.2004.003728
28 Hwang, H. Y.; Iwasa, Y.; Kawasaki, M.; Keimer, B.; Nagaosa, N.; Tokura, Y. *Nature Mater.* **2012**, *11*, 103-113. DOI: 10.1038/nmat3223
29 Thiel, S.; Hammer, I. G.; Schmeh, I. A.; Schneider, C. W.; Mannhart, J. *Science* **2006**, *313*, 1942–1945. DOI: 10.1126/science.1131091
30 Chakhalian, J.; Millis, A. J.; Rondinelli J. *Nature Mater.* **2012**, *11*, 92-94. DOI: 10.1038/nmat3225
31 Mannhart, J.; Schlom, D. G. *Science* **2010**, *327*, 1607-1677. DOI: 10.1126/science.1181862
32 Biscaras, J.; Bergeal, N.; Hurand, S.; Feuillet-Palma, C.; Rastogi, A.; Budhani, R. C.; Grilli, M.; Caprara, S.; Lesueur, J. *Nature Mater.* **2013**, *12*, 542-548. DOI: 10.1038/nmat3624
32 Mannhart, J.; Blank, D. H. A.; Hwang, H. Y.; Millis, A. J.; Triscone, *J. M. Mater. Res. Soc. Bull.* **2008**, *33*, 1027-1034. DOI: 10.1038/ncomms2394
33 Ohtomo, A.; Hwang, H. Y. *Nature* **2004**, *427*, 423-426. DOI: 10.1038/nature02308
34 Tsukazaki, A.; Ohtomo, A.; Kita, T.; Ohno, Y.; Ohno, H.; Kawasaki, M. *Nature Mater.* **2010**, *9*, 889-893. DOI: 10.1038/nmat2874
35 Lu, M-L.; Lai, C-W.; Pan, H-J.; Chen, C-T.; Chou P-T.; Chen, Y-F. *Nano Lett.* **2013**, *13*, 1920-1927. DOI: 10.1021/nl3041367
36 Lee, M-J.; Kim, S. I.; Lee, C. B.; Yin, H.; Ahn, S-E.; Kang, B. S.; Kim, K. H.; Park, J. C.; Kim, C. J.; Song, I.; Kim, S. W.; Stefanovich, G.; Lee, J. H.; Chung, S. J.; Kim, Y. H.; Park, Y. *Adv. Funct. Mat.* **2009**, *19*, 1587-1593. DOI: 10.1002/adfm.200801032
37 Sun, K.; Pang, X.; Shen, S.; Qian, X.; Cheung, J. S.; Wang, D. *Nano Lett.* **2013**, *13*, 2064-2072. DOI: 10.1021/nl400343a
38 Zhang, C.; Chen,J.; Zeng, Y.; Rui, X.; Zhu, J.; Zhang, W.; Xu, C.; Lim, T. M.; Hng, H. H.; Yan, Q. *Nanoscale* **2012**,4, 3718-3724. DOI: 10.1039/C2NR30525A
39 Thanh, N. T. K.; Green, L. A. W. *Nano Today* **2010**, *5*, 213-230. DOI: 10.1016/j.nantod.2010.05.003

Supporting Information

Laser-Directed Self-Organization and Reaction Control in Complex Systems -

A Facile Synthesis Route for Functional Materials

Hendrik M. Reinhardt[1], Clemens Pietzonka[1], Bernd Harbrecht[1,2], Norbert Hampp[1,2]*

[1] Department of Chemistry, Philipps-University of Marburg

Hans-Meerwein-Str., 35032 Marburg, Germany

[2] Material Science Center, 35032 Marburg, Germany

Contents

1   Experimental Design

Laser modifications of stainless steel EN 1.4301 (AISI 304) were conducted with a Nd:YVO$_4$ DPSS nanosecond pulsed laser (Vector 532-1000-20, Coherent, USA) emitting a wavelength of 532 nm in spatial mode TEM$_{00}$ at a pulse repetition rate of 30 kHz and a pulse width of 5 ns. The average laser power delivered to the specimen was kept at a constant level of 610 mW for all experiments, controlled by a laser power meter (FieldMaxII, Coherent, USA). The laser beam was focused to an effective spot size of 30 µm diameter (or 707 µm^2) by an F-Theta lens (Ronar-532-163, Rodenstock, Germany). Each laser pulse delivered a laser fluence of ϕ_{pulse} = 2.88 J/cm^2 to the specimen. In order to modify extended surface areas the laser spot was scanned over steel samples using a galvanometer head (SCANgine14-532, SCANLAB, Germany). Both, the laser output characteristics as well as the line spacing (3 µm) of the scan pattern were kept constant in all experiments. The pool of different surface modifications on stainless steel results solely from different numbers of laser pulses delivered to the surface of individual steel samples. This was achieved by systematic variations of the laser spot line scan speed S, which results in different total numbers of laser pulses P_{total} delivered to an area A_{total} = 1 cm^2 on each sample. **Table S1** shows laser modification parameters for all steel samples at a glance.

| sample number	S (mm/s)	P_{total} (cm^{-2})	DC (n)
0 (virgin steel)	-	-	-
1	682	1.4 · 10^6	10
2	346	2.8 · 10^6	20
3	231	4.3 · 10^6	31
4	223	4.5 · 10^6	32
5	215	4.6 · 10^6	33
6	206	4.8 · 10^6	34
7	196	5.1 · 10^6	36
8	184	5.4 · 10^6	38
9	172	5.8 · 10^6	41
10	159	6.3 · 10^6	44
11	146	6.8 · 10^6	48
12	132	7.5 · 10^6	53
13	119	8.4 · 10^6	59
14	106	9.5 · 10^6	67
15	93	1.1 · 10^7	76
16	81	1.2 · 10^7	87
17	70	1.4 · 10^7	101
18	60	1.7 · 10^7	117
19	51	1.9 · 10^7	138
20	43	2.3 · 10^7	165
21	34	2.9 · 10^7	205
22	24	4.1 · 10^7	292
23	12	8.3 · 10^7	589
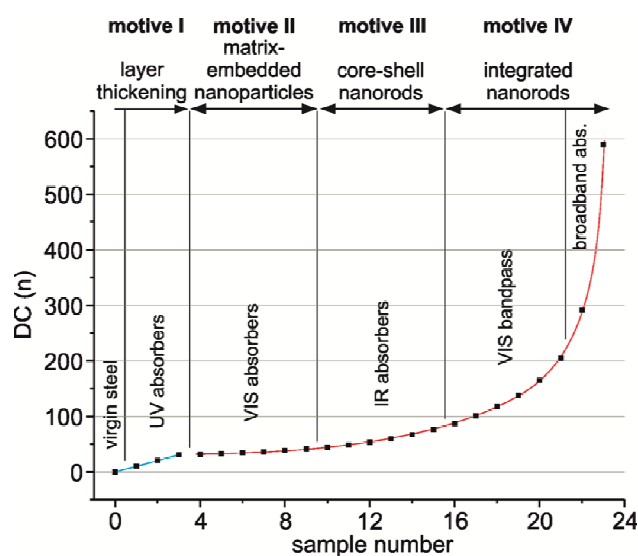
Fig. S1   *DC*-assignment for a set of 24 steel samples

Tab. S1   Laser parameters for the modification of extended surface areas on stainless steel 1.4301 (AISI 304)
Constant irradiation parameters: 532 nm wavelength, pulse width 5 ns, laser power on sample 610 mW, pulse repetition rate 30 kHz, pulse energy 20.33 µJ, effective laser spot diameter 30 µm, laser fluence 2.88 J/cm^2, line spacing of scan pattern 3 µm.

Typically, PLiD stimulated nanostructure formation is triggered by a certain number of fully overlapping laser pulses at a given laser fluence ϕ_{pulse}. In contrast to this, we applied a dynamic PLiD process in order to modify surface areas larger than the footprint of one laser spot. For comparative purposes, characteristic process parameters were derived statistically. Accordingly, the number of fully overlapping laser pulses, abbreviated as dewetting cycles DC, delivered to an area the size of one laser spot footprint (a_{pulse} = 707 µm^2) is given by the equation: $DC = a_{pulse} / A_{total} \cdot P_{total}$. One DC is defined to be a laser pulse delivering a fluence of ϕ_{pulse} = 2.88 J/cm^2 to the specimen. Each of the 24 stainless steel samples was subjected to a selective number of DC that is assigned according to functions given in **Fig. S1**. Based on experience, this course of DC increase was found to be optimal in order to cover a broad variety of surface modifications within the sample range. It is initially characterized by a linear slope but progresses into an exponential growth ranging up to 589 DC.

2   Phase analysis of PLiD-modified steel EN 1.4301

PLiD modifications induce changes to the crystalline structure of stainless steel that are traceable by X-ray powder diffraction (XPD). A comparison between diffraction patterns of untreated and PLiD- affected stainless steel visualizes the effects of this treatment **(Fig. S2)**. Peak intensity shifts and peak broadenings indicate a transformation of microcrystalline steel to a nanocrystalline and textured material. The lattice parameter of the fcc-phase shows only a slight decline in lattice spacing after laser treatment. More striking is the occurrence of a second phase that manifests in a distinct peak at 44.42 ± 0.01 °2θ$_{Cu}$. This peak in addition with less pronounced peaks at 64.86 and 82.27 ± 0.01° 2θ$_{Cu}$ indicate an emerging bcc-phase in PLiD modified stainless steel. The phase is also known as δ-ferrite, a magnetic allotrope of iron that is normaly not found in austenitic stainless steel like EN 1.4301 (AISI 304). Of course, the phase is not expected to be pure δ-ferrite because EN 1.4301 contains additional alloying elements beyond iron. Anyway, magnetic measurements (**Supporting Information 4)** show a subsequent magnetization of PLiD modified EN 1.4301, thus supporting this result of Rietveld analysis.
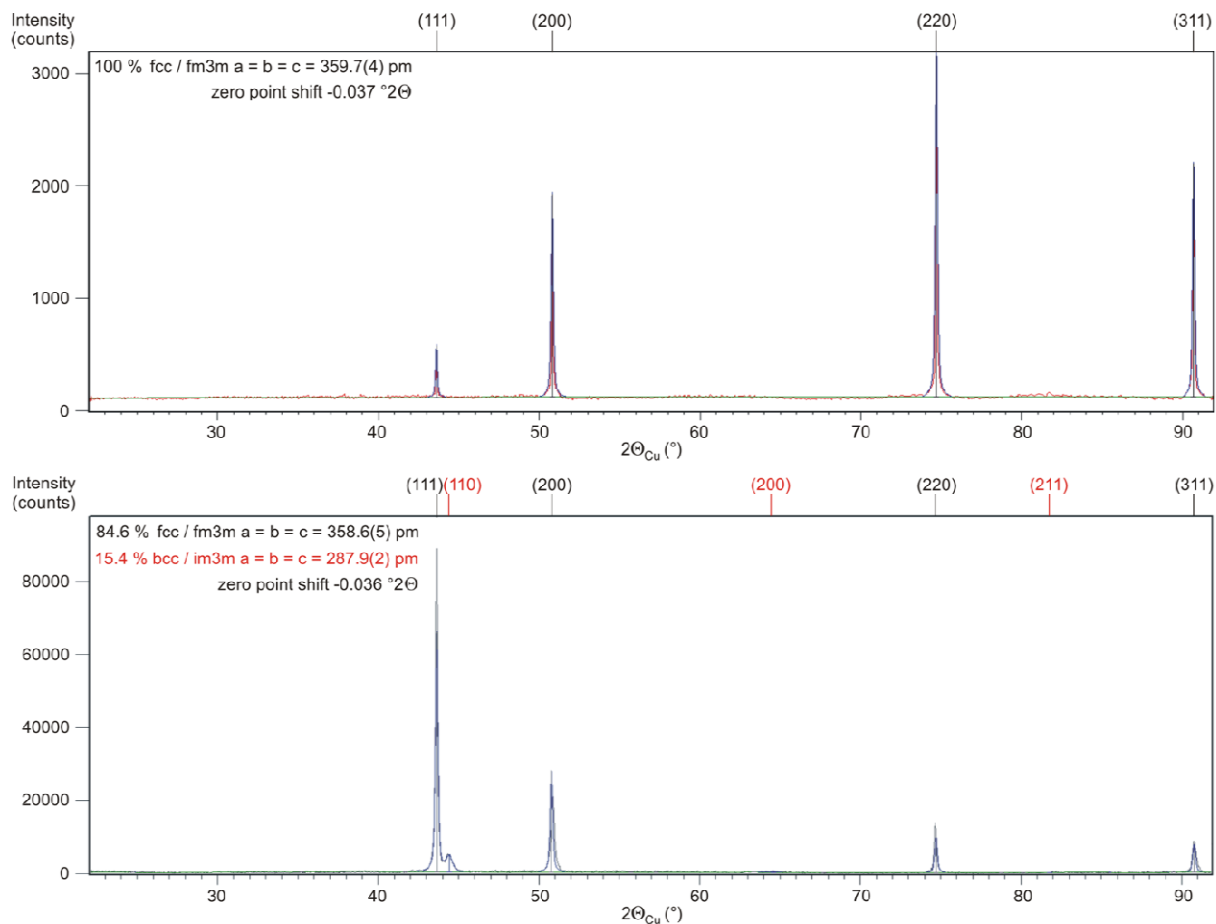
Figure S2   Rietveld analysis of XPD patterns
top: untreated austenitic stainless steel type EN 1.4301 (AISI 304)
bottom: the same alloy after PLiD treatment with 101 DC

3   Scherrer crystallite size estimation

Grain size refinements in PLiD-modified stainless steel samples were determined using the Scherrer crystallize size estimation (SCSE). The analytical procedure is exemplified on the basis of a stainless steel sample treated with 165 DC **(Fig. S3)**. Single peaks extracted from the XPD pattern of this sample were fitted with a Lorentz function in order to extract full width half maxima (FWHM). Based on these data, crystallite sizes for fcc- and bcc-phases were calculated using a form factor of k = 0.9 in the Scherrer equation. The 165 DC sample shows a size distribution of fcc-crystallites ranging between 19.2 and 37.4 nm, thus indicating shape anisotropy or a fibrous recrystallization respectively. The size of bcc-crystallites was derived from a single peak located at 44.42 ± 0.01 °$2\theta_{Cu}$ because other peaks of this phase are too less pronounced for FWHM evaluation. The determined bcc-crystallite size of 10.9 is significantly smaller than the fcc-crystallite size. This indicates that bcc precipitates originate from an earlier state of structure maturity compared to fcc crystallites. The issue is discussed in the paper.
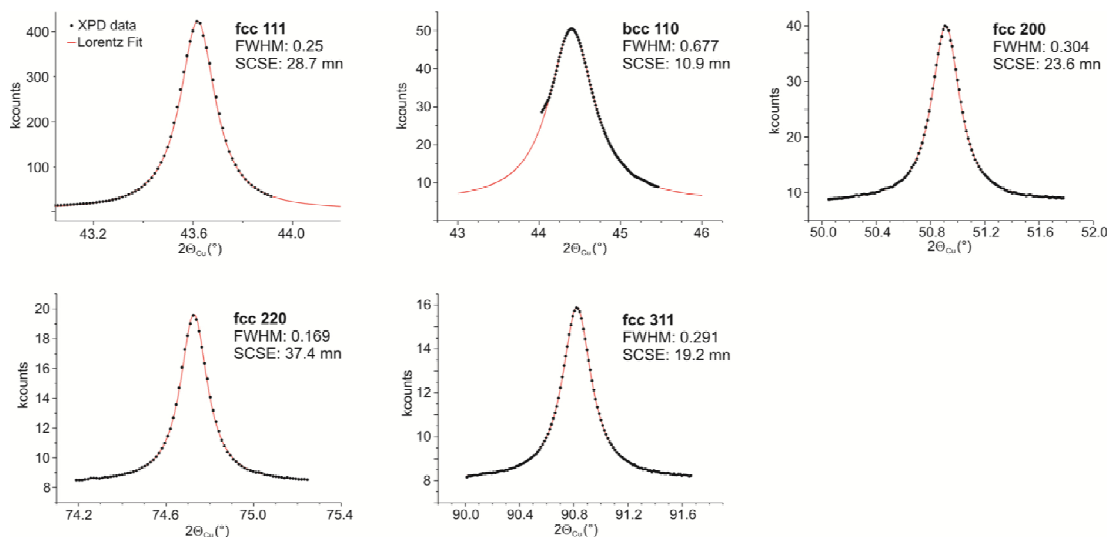
Fig. S3   Reflection profile analysis and Scherrer crystallite size estimation (SCSE) of a 165 DC stainless steel sample

60

4 Magnetic characterization by SQUID

Magnetic measurements were performed on a superconducting quantum interference device (DC-SQUID, Quantum Design, USA). In order to improve the signal to noise ratio we used stainless steel foils (EN 1.4301, AISI 304) of 100 µm thickness instead of steel sheets (800 µm thickness). The higher surface to volume ratio of foils allows for more accurate characterizations of PLiD effects to the magnetic behavior in subsurface regions. Zero field cooling magnetization curves (ZFC) were obtained during slow temperature increase from 2.5 K to 300 K in a weak H-field of 50 Oe. Field cooling magnetization curves (FC) were recorded in the cool down phase to 2.5 K at an H-field of 50 Oe. Magnetic hysteresis loops were measured at 300 K in a range of ± 50 kOe. Data analyses were performed using Origin Pro 8.

Calculation of the area-normalized magnetization M_A from magnetic measurements:

$$M_A = M_{obs} \cdot \rho_{V2A} \cdot d_{V2A} \cdot m^{-1}$$

M_{obs} represents the measured magnetization of the sample in electromagnetic units (emu), whereas ρ_{V2A} is the density of stainless steel (7.9 g cm^{-3}), d_{V2A} the thickness of the steel foil (100 µm) and m the mass of the sample. Magnetic hysteresis loops were recorded at 300 K in a range from -50 to 50 kOe; examples are given in **(Fig. S4a)**.
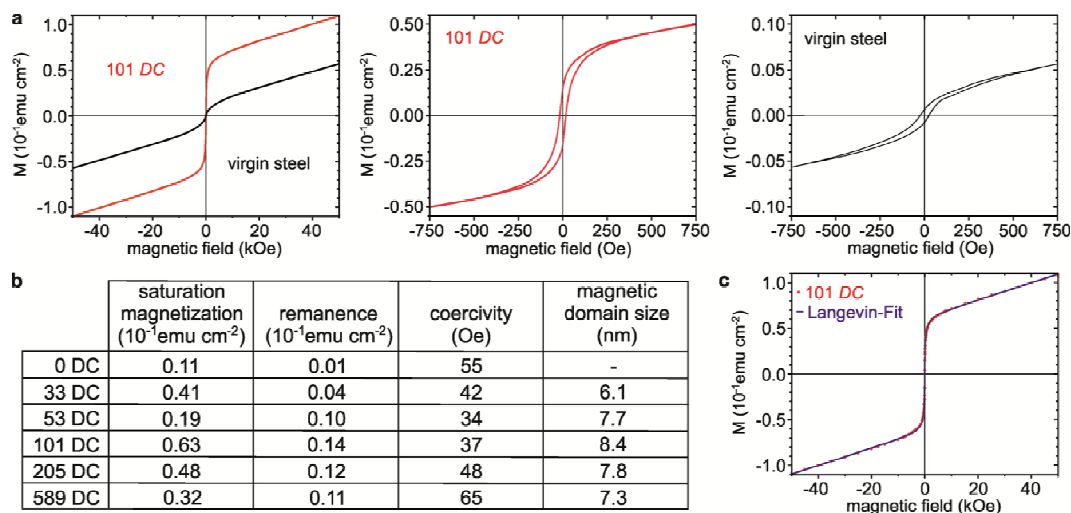
Fig. S4 SQUID-magnetometry of untreated and PLiD-modified stainless steel foils EN 1.4301 (AISI 304)
(a) Comparison between hysteresis loops of untreated (black) and PLiD-modified (red) steel foils. Magnifications show coercivity and remanence. **(b)** Table of magnetic parameters for 6 samples of the sample set. **(c)** Examplary Langevin Fit (bimodal) used for magnetic domain size determination.

	saturation magnetization (10^{-1}emu cm^{-2})	remanence (10^{-1}emu cm^{-2})	coercivity (Oe)	magnetic domain size (nm)
0 DC	0.11	0.01	55	-
33 DC	0.41	0.04	42	6.1
53 DC	0.19	0.10	34	7.7
101 DC	0.63	0.14	37	8.4
205 DC	0.48	0.12	48	7.8
589 DC	0.32	0.11	65	7.3

When comparing the hysteresis loops of untreated stainless steel and a sample that was subjected to 101 cycles, a significantly higher saturation magnetization is striking. Interestingly, the coercivity of both, untreated steel and PLiD modified steel is rather low **(cp. Fig. S4b)**. This tendency to superparamagnetic behavior is supposed to be attributed to very small magnetic domain sizes. Using the Langevin function, magnetic domain sizes were determined in a DC-dependent size range between 6.1 and 8.4 nm.

Determination of the magnetic domain size by the Langevin function:
The magnetization depending on external field (H_0) and temperature (T) in a system of macroscopic magnetic moments can be described by the Langevin function with respect to the average magnetic moment (μ) of a particle.

$$m = m_{sat} \cdot L$$
$$L = \coth(\alpha) - \frac{1}{\alpha}$$
$$\alpha = \frac{\mu H_0}{k_B T}$$

Fig. S4c shows a Langevin Fit on the example of a stainless steel treated with 101 DC. The Langevin-fit delivered the following value:
*$\mu = 5.4 \cdot 10^{-16}$ emu = 58252 BM*
μ represents the average magnetic moment of a domain. Taking into account V_{at} and μ_{at}, the volume of a magnetic domain is available and thus its radius. For α-Fe the value is 2.2 Bohr magnetons, bcc phases of Fe$_{0.9}$Ni$_{0.1}$ and Fe$_{0.8}$Cr$_{0.2}$ feature values of 2.1 and 1.7 BM, respectively.[S1, S2]
As listed in **Fig. S4b**, magnetic domain sizes of PLiD modified steel range between 6.1 and 8.4 nm in diameter. Considering that bcc nanocrystals fall into a size range of 11 to 14 nm (estimated by SCSE) indicates that each bcc crystal represents either a single magnetic domain or contains a maximum of two magnetic domains. Even though, magnetic domains in this size range can be expected to cause superparamagnetic behavior, a clear deblocking was not observed in the temperature range of ZFC-FC measurements (**cp. Fig. 1g**). This is expected to be attributed to the stainless steel matrix in which fcc-nanocrystals are

embedded, thus inhibiting Brown-relaxation. The absence of Néel-deblocking in the course of ZFC-FC measurements indicates that fcc-nanocrystals feature more than one energetic state.

5   Nanomagnetic characterization by MFM

PLiD-generated bcc-precipitates not only affect the macroscopic magnetic properties of stainless steel but also the nanoscopic magnetic profile of its surface. **Fig. S5** shows a comparative plot of magnetic profiles recorded by magnetic force microscopy (MFM).
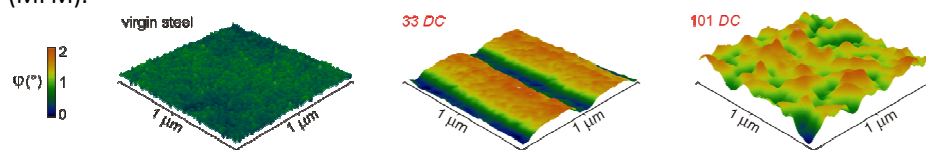

Fig. S5   Magnetic profile analysis by magnetic force microscopy (MFM)
Magnetic force microscopy was performed on a Nanoscope IV (Bruker, USA) using MESP-RC tips (antimony n-doped Si, 0.01-0.025 Ω, magnetic Co/Cr coating with coercivity of ~400 Oe, k = 5-10 N/m, f_0 = 150-200 kHz, Bruker) utilizing the LiftMode feature of the microscope. Magnetic force detection was accomplished by a two-pass procedure in which a line profile of the specimen is scanned by tapping mode in a first pass. Memorized topographic data are then used to guide the second pass in a lift height of 20 nm above the previously scanned profile. Disparities in surface magnetization interfere with the magnetic tip, thus inducing cantilever deflection that was contrasted by phase detection (φ) during this noncontact scan.

As the figure implies, there is only a faint magnetic profile to be found on virgin steel. In contrast to that, the sample treated with 101 DC shows a distinct magnetic profile with roughness on the nanometer scale. Compared to the magnetic profile of a sample treated with 33 DC it is rather chaotic, thus indicating isle-like bcc-precipitation. As mentioned in the paper, the 33 DC sample was subjected to a special phenomenon named Laser-induced Periodic Surface Structures (LIPSS). It can occur as the consequence of light-matter feedback mechanisms that create temporary instabilities in an initially homogeneous spatial state. Depending on the type of material a certain number of laser pulsed at a specific laser fluence is needed to stimulate LIPSS. As the results show, irradiation conditions for the creation of this hierarchical self-organization phenomenon fall within the PLiD parameter space. Beyond other interesting effects, LIPSS generates regular patterns of bcc-precipitates in stainless steel, thus equipping the material with a magnetically patterned surface.[S3]

6   Segregation scenario of PLiD-generated metal-oxides on steel EN 1.4301

Compared to pure metals the oxidation of alloys produces mixed oxides that feature complex layering structures. By the fact that oxide formation on alloys follows thermodynamic and kinetic laws it can be predicted to a certain degree of accuracy, which depends on the complexity of the system under consideration. Ellingham diagrams are very helpful to derive a forecast on oxide formation on alloys as they display and compare the stabilities of metal oxides under stated conditions. A diagram reduced to the components of our model system stainless steel EN 1.4301 (AISI 304) is illustrated in **Fig. S6**.
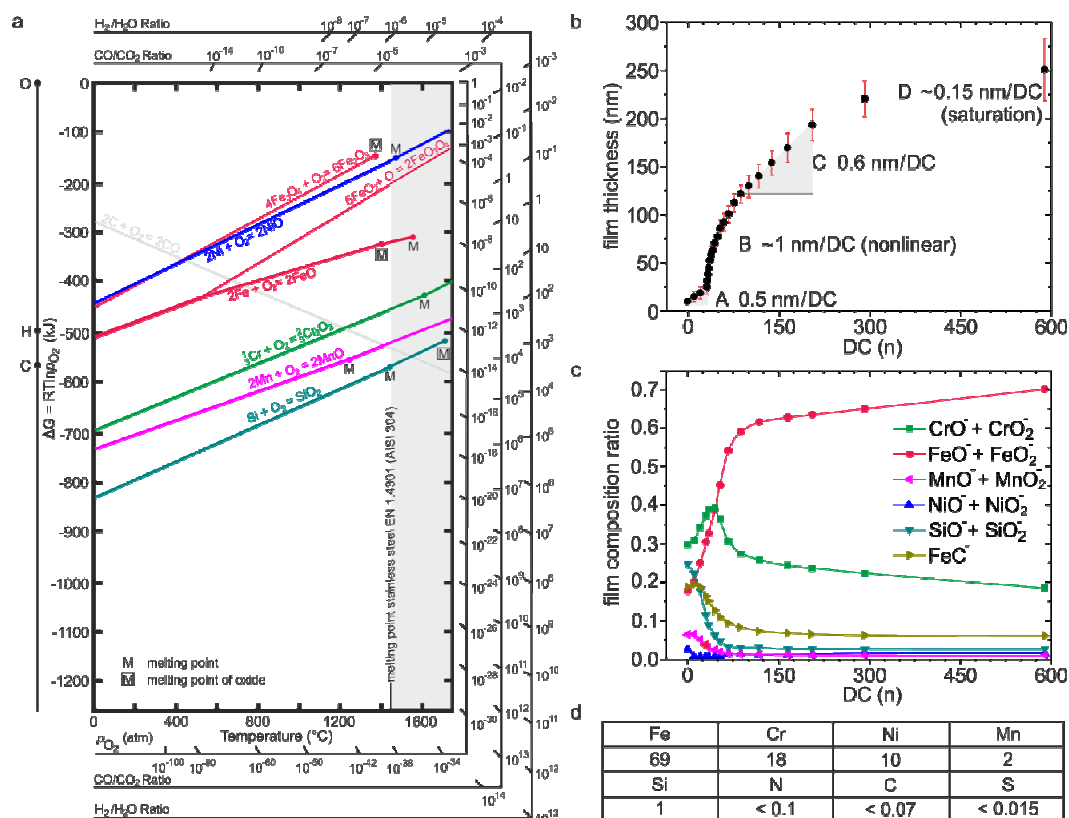

Fig. S6
Theory and observation of PLiD-induced oxide segregation on stainless steel EN 1.4301 (AISI 304)

(a) Ellingham diagram for stainless steel EN 1.4301 (AISI 304). Thermodynamic parameters extracted from D. R. Gaskell.[S4]
(b) DC-dependent metal oxide growth on EN 1.4301. **(c)** DC-dependent metal oxide composition on EN 1.4301. **(d)** Alloy composition of EN 1.4301 (mean, in wt%).

The diagram shows that all elements contained in stainless steel feature different free energies of oxide formation. It indicates that Si will preferably oxidize over other elements in the alloy and Mn will oxidize next when Si becomes depleted. Overall, the Ellingham diagram predicts an oxidation sequence of Si>Mn>Cr>>Fe>Ni in a temperature range between 0 and 1700 °C. This includes the melting point of stainless steel EN 1.4301, which is surpassed in each dewetting cyle. During a PLiD cycle alloy constituents oxidize in rates according to their affinity to oxygen and eventually solidify in time scales of a few nanoseconds. Although this process cannot be expected to run under equilibrium conditions, its outcome corresponds well with thermodynamic expectations, as the segregation scenario (**Fig. S6c**) demonstrates. Si- and Mn-oxides are preferably oxidized and thus suffering rapid depletion in the laser affected zone. As a result more and more chromium is oxidized in each photo-thermal cycle. Due to the high availability of chromium in stainless steel (18 wt%) the growing oxide film is enriched with increasing amounts of chromium-oxides and its derivates. It takes only a few PLiD-cycles more and also chromium suffers local depletion (starting from 30 DC). What happens now can best be illustrated by a series of TOF-SIMS depth profiles **(Fig. S7)**.
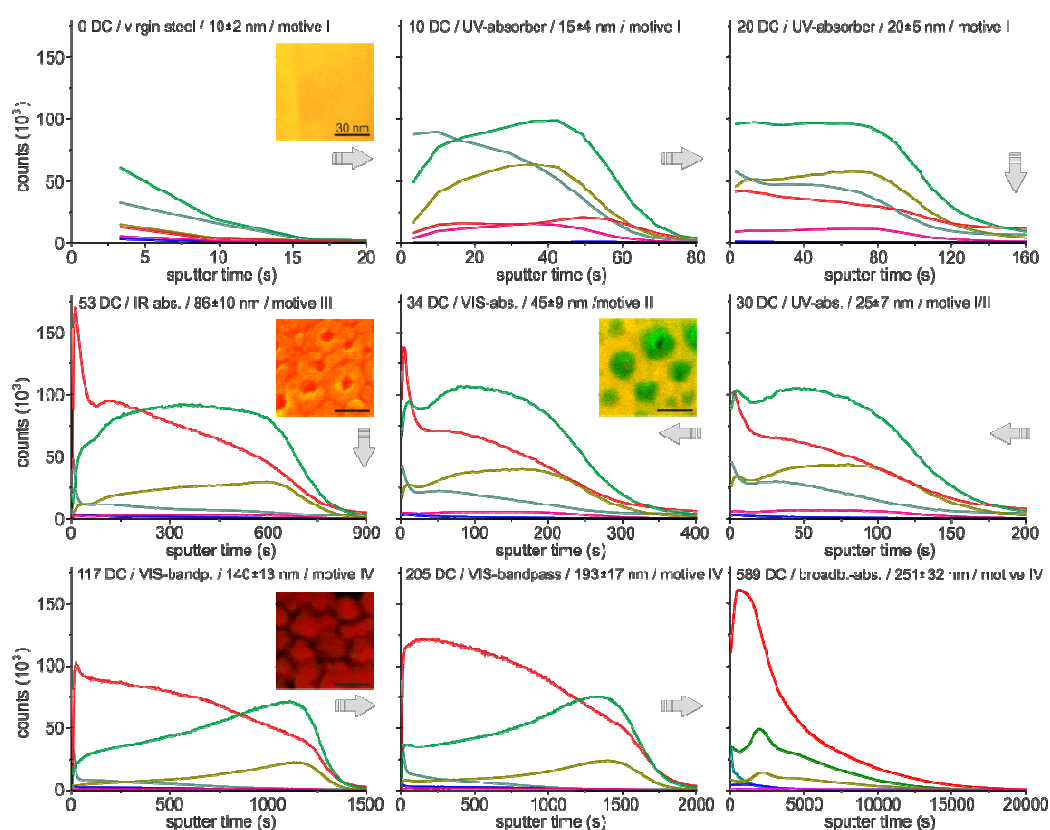
S7 Selection of ToF-SIMS depth profiles obtained from metal oxide scales on PLiD-modified stainless steel EN 1.4301
The arrows guide through an evolution of compositional depth profiles obtained from samples subjected to increasing numbers of DC. All depth profiles were recorded by layer-by-layer ablation of oxide thin films on steel using a scanned antimony-ion-beam at constant current. Mass peak assignment using a database of known mass fragments (see legend, top left) yielded insights into the layering structure of PLiD generated oxides.

Exceeding 30 DC, pervasive streams of activated iron-species striving for oxidation sites traverse existent passivation films. The impact of this process to the lateral distribution of metal oxide species is apparent regarding the material contrasts of these films (see insets).

7 Optical characteristics of PLiD-generated metal oxides on steel EN 1.4301

The answer to the question why an ordinary material like stainless steel readily blossoms into such a multitude of optical features is actually not trivial. One might argue that the origin of this spectral diversity is a consequence of thin film interference. However, optical shifts that are typical for interference colors were not observed by angle dependent measurements on modified steel samples **(Fig. S8)**.
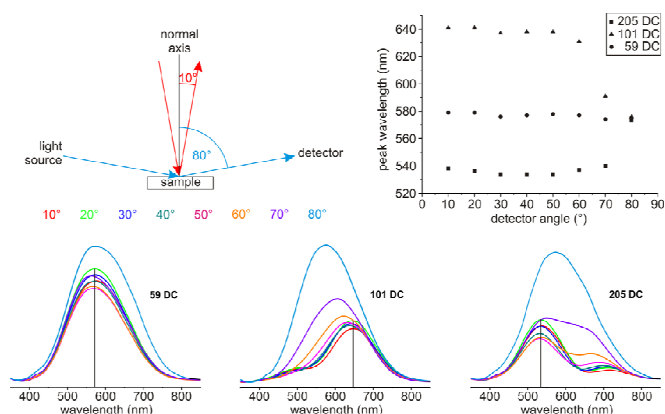

Fig. S8 Angle-dependent measurements on PLiD-modified steel

Optical shifts only occur when detector angles of 70 ° are surpassed and this is due to total reflection of irradiated light at the air-oxide interface. Another proof for inconsistence with the physics of thin film interference are peculiarities in the course of average reflectance of PLiD-modified steel **(Fig. S9)**.
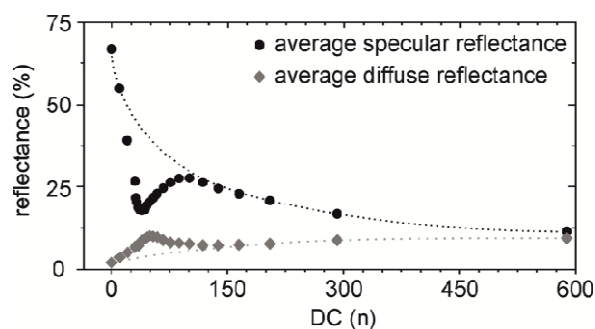
Fig. 9 Average specular reflectance and average diffuse reflectance of steel samples in the spectral range from 200 to 1100 nm wavelength

A minimum in average specular reflectance is observed for a sample with a film thickness of 58 nm (38 DC), whereas a maximum of diffuse reflectance occurs for a sample with an oxide-film of 70 nm thickness (44 DC). This is inconsistent with thin film interference, because similar values of averaged specular and averaged diffuse reflectance are also reached by samples featuring ceramic films that exceed 200 nm thickness.

Based on these analyses, the broad variation of optical properties in the sample set is expected to be a result of subsequent changes in the electronic structure of transition metal oxides. UV-absorption of steel samples subjected to 10 - 31 DC can be explained by increasing optical density due to film thickening from 10 to 25 nm because all analyzed oxides absorb in this spectral region. In contrast to that, optical properties emerging from modifications induced by DC numbers exceeding 32 are considerably more difficult to understand because they originate from complicated interactions between chemical and structural features. Backscattered electron inspection (BSE) on VIS-absorbers (32-41 DC) show material contrasts that indicate oxide segregations in TMO thin films **(cp. Fig. 3a)**. Considering that transition metals like Cr, Mn and Fe feature almost the same electron backscattering efficiency due to similar atomic numbers (Z = 24-26) gives several possibilities for this contrast to occur:

- density fluctuations in the solid solution of oxides
- Si-oxide segregations because Z_{Si} = 14
- oxygen deficiencies or rather unsatisfied valence

In any case, such nanoscopic inhomogeneities affect the electronic structure of TMOs and thus its optical properties due to interface formation in the local electronic environment. Even more distinct structure formation is observed for NIR-absorbers (44-76 DC), although the material contrast is no longer as pronounced but still existent in these arrays of vertically aligned core shell nanorods. Interestingly, samples featuring VIS-bandpass and broadband-absorber capabilities (87-589 DC) do not show internal boundaries detectable be BSE and not even distinct differences in composition according to ToF-SIMS. Statistical compilations show a significant influence of the nanorod diameter distribution to be the origin of optical tunability observed for this group **(cp. Fig. 4b, c)**.

References in the Supporting Information

S1 Dumpich, G.; Wassermann, E. F.; Manns, V.; Keune, W.; Murayama, S.; Miyako, Y.   *Journal of Magnetism and Magnetic Materials* **1987**, *67*, 55-64.

S2 Aldred, A. T. *Physical Review B* **1976**, *14*, 219-227.

S3 Reinhardt, H.; Kim, H-C.; Pietzonka, C.; Kruempelmann, J.; Harbrecht, B.; Roling, B.; Hampp, N. *Adv. Mat.* **2013**, DOI: 10.1002/adma.201205031.

S4 Gaskell, D. R. *Introduction To The Thermodynamics Of Materials*, 4th ed., Taylor & Francis Books Inc., London **2003.**

B   Self-Organization of Multifunctional Surfaces - The Fingerprints of Light on a Complex System.

Hendrik M. Reinhardt, Hee-Cheol Kim, Clemens Pietzonka, Julia Kruempelmann, Bernd Harbrecht, Bernhard Roling, Norbert Hampp

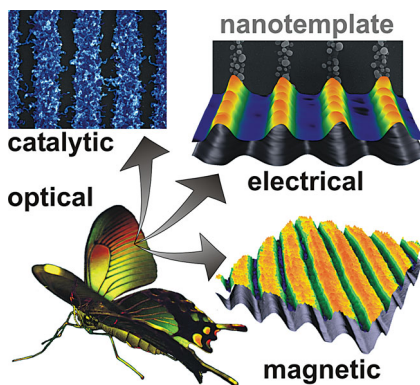*Adv. Mater.* (25) 3257, **2013.** DOI: 10.1002/adma.201370155
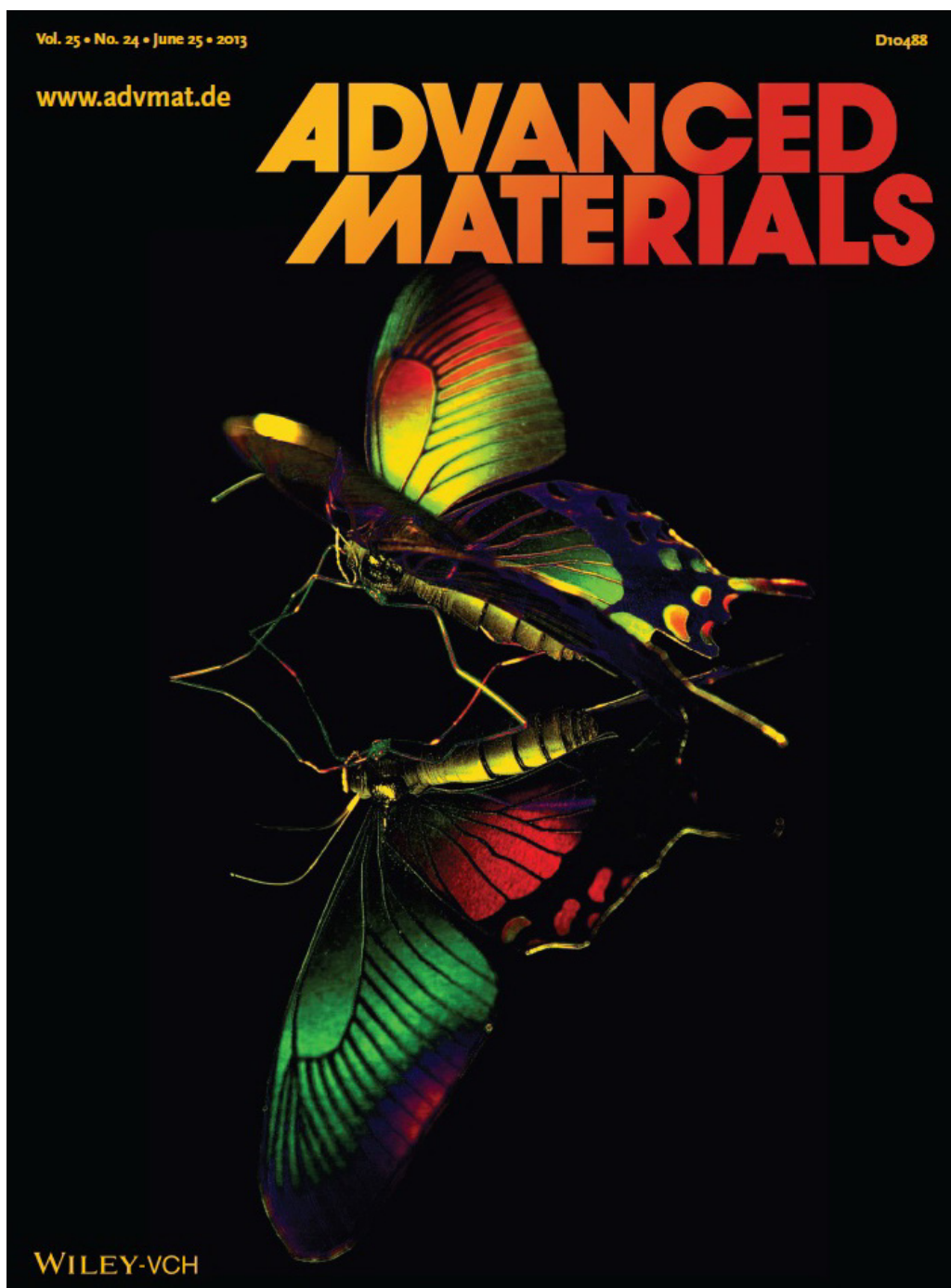
Self Organization

H. Reinhardt, H.-C. Kim, C. Pietzonka,
J. Kruempelmann, B. Harbrecht,
B. Roling, N. Hampp* ....x–xx

Self-Organization of Multifunctional Surfaces – The Fingerprints of Light on a Complex System

Nanocomposite patterns and nano-templates are generated by a single-step bottom-up concept that introduces laser-induced periodic surface structures (LIPSS) as a tool for site-specific reaction control in multicomponent systems. Periodic intensity fluctuations of this photothermal stimulus inflict spatial-selective reorganizations, dewetting scenarios and phase segregations, thus creating regular patterns of anisotropic physicochemical properties that feature attractive optical, electrical, magnetic, and catalytic properties.

Self-Organization of Multifunctional Surfaces – The Fingerprints of Light on a Complex System

*Hendrik Reinhardt, Hee-Cheol Kim, Clemens Pietzonka, Julia Kruempelmann, Bernd Harbrecht, Bernhard Roling, and Norbert Hampp**

Self-organization and pattern formation in complex systems is one of nature's outstanding capabilities.[1,2] Inspired by the concept in nature of triggering system reorganizations by a specific stimulus, scientists around the world explore its imitation.[3,4] Self-organization processes are becoming increasingly important, as they play a key role for efficient production of highly ordered systems. Massive efforts in research continuously improve the understanding of self-organization[5–11] and expand the repertoire of this fascinating interdisciplinary field.[12–15] The science of pattern formation benefits from this acquired knowledge, as it utilizes the principles of self-organization by directing them with spatio-temporal stimuli.[16–19] In general, pattern formation is a dynamic process that generates periodic structures resulting from temporary instabilities of an initially homogeneous spatial state. An elegant way to realize this special type of stimulus for practical applications is given by a phenomenon named laser-induced periodic surface structures (LIPSS).[20] The self-constructing nature of periodic light intensity patterns was demonstrated on metals, dielectrics, semiconductors and polymers as a result of intense laser irradiation.[21–24] Scientists are captivated by the simplicity of LIPSS generation and even more by the fact that no consistent theory was found for this effect so far.[25] Most studies restrict their investigations to the origin of the phenomenon itself or to morphological patterning of pure materials. In contrast to this, we investigate the effects of LIPSS to complex systems and found a number of additional types of patterning; an overview is given in the Supporting Information, Section 1. Of course, compared with the complexity of biological systems, this approach is rather simple, but it shows that even a manageable number of components in a system give raise to the formation of multifunctional surfaces, like those found in nature.

Our model system, austenitic steel, type EN 1.4301 (AISI 304), belongs to the most widely applied steel alloys worldwide. Surface modifications to this material were conducted by a nanosecond-pulsed laser emitting linearly polarized light at a wavelength of 532 nm. For the generation of LIPSS on stainless steel (SS), henceforth abbreviated as SSLIPSS, steel samples were irradiated in ambient air. SSLIPSS formation was found for total laser fluencies Φ_{total} in the range from 30 to 120 J cm^{-2}, optimal results were achieved at $\Phi_{total} = 75$ J cm^{-2} on mirror-polished steel (see Supporting Information, Section 2 for details). Successful SSLIPSS generation causes significant changes of the optical properties of steel; some examples are given in **Figure 1**. The diffraction characteristics were found to be attributed to regular patterns of sinusoidal waves with a periodicity of 500 nm. The fact, that this morphological modification was not structured line by line, legitimates the question of its origin. As already mentioned, LIPSS is a phenomenon of light whose physical background is not fully understood yet. The self-construction of inhomogeneous intensity distributions on the surface of solids subjected to intense laser irradiation was interpreted by interference of the incident laser beam with its backscattered wave front.[26] Theoretical expectations concerning the periodicity of such intensity fringe patterns can be derived from the equation[27] $\Lambda = \lambda[n(1 \pm \sin\theta)]^{-1}$, where λ is the laser wavelength, θ the angle of incidence from normal, n the refractive index of the fringe pattern envelope, and Λ the fringe spacing. However, this theory is limited to the prediction of fringe patterns induced by nanosecond-pulsed lasers up to a critical angle of incidence and has been proved insufficient when femtosecond pulsed lasers are used. Other theories consider the LIPSS effect to be related to surface plasmon polaritons[28,29] but this dispute is actually not the scope of our study. We want to demonstrate the potential of laser-induced fringe patterns as a trigger for spatial selective transformations in multicomponent systems. First of all, we enlighten the basic transformations that occur in stainless steel as a result of LIPSS modification and derive a model for morphological pattern formation.

X-ray diffraction patterns (XPD) display distinct changes in the crystalline structure of steel after LIPSS modification (**Figure 2**b). Massive peak broadenings and peak intensity shifts indicate that a fringe pattern impact converts initially coarse grained steel into a highly textured and nanocrystalline material. Grain refinements were analyzed using the Scherrer crystallite size estimation (Supporting Information, Section 4). Accordingly, the former microcrystalline austenite phase of steel (γ-Fe) was transformed to γ-Fe-crystallites ranging from 13 nm to 47 nm. This result combined with distinct shifts of reflections, in particular a pronounced increase of the γ-Fe-(111)-reflection, suggests a fibrous austenite recrystallization in (111)-texture (Supporting Information, Section 5). Transformations of this kind are typically induced by mechanical stress or heat treatment:[30] in our case, a photothermal process is the driving force. Laser-induced thermal cycling was demonstrated to effect the granularity of steels due to rapid surface melting and

H. Reinhardt, Dr. H.-C. Kim, C. Pietzonka,
Dr. J. Kruempelmann, Prof. B. Harbrecht,
Prof. B. Roling, Prof. N. Hampp
Department of Chemistry
University of Marburg
35032 Marburg, Germany
E-mail: hampp@staff.uni-marburg.de

ADVANCED
MATERIALS
www.advmat.de

Materials
Views
www.MaterialsViews.com

COMMUNICATION
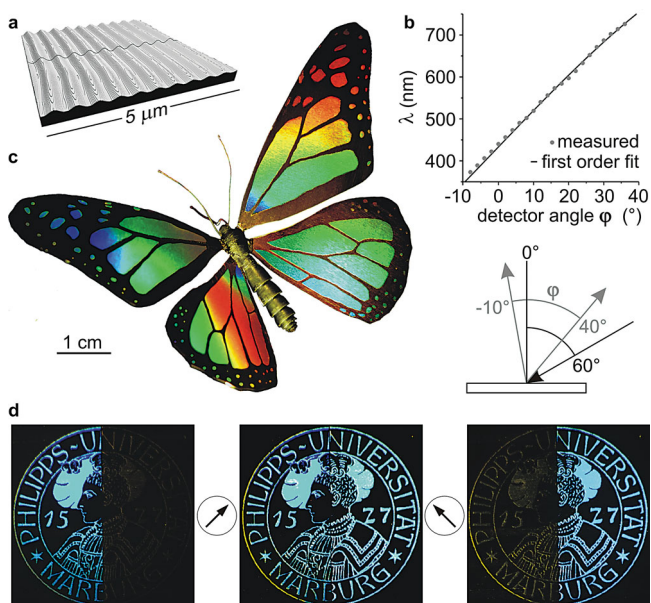
Figure 1. Optical properties of SSLIPSS. a) The surface topography of SSLIPSS was analyzed by laser scanning microscopy (LSM) and features a periodic grating with a periodicity of 500 nm. b) Angle dependent measurements of SSLIPSS show a diffraction characteristic that is close to theoretical expectations for a grating of 2000 lines per millimeter. The experimental setup is sketched below the graph. c) High process robustness allows for LIPSS-modification of larger surface areas and even on rolled blank stainless-steel foils. As an example, a butterfly model with a wing-span of 75 mm was prepared from LIPSS-modified steel foil. More examples and process-related details are provided in the Supporting Information, Section 2. d) Since LIPSS-formation is a laser-based process it facilitates rapid implementations of arbitrary designs. The example logo contains two SSLIPSS-patterns in orthogonal orientations that are adjacent at the centerline of the pictures. Depending on the direction of illumination (indicated by arrows) either the left, or the right side of the logo reflects a certain fraction of incident light to the observer.

resolidification.[31] Such reorganizations from the liquid state are generally attributed to the plateau Rayleigh instability of thin liquid films, that break up into particles striving for a more favorable energy state.[32,33] This principle of self-organization is very promising for nanostructure formation, however, selective capturing of certain particle maturity states is demanding. Pulsed laser-induced dewetting (PLID) is a technique that gives control over liquid lifetimes by supporting thermal cycling rates up to 10^{10} K s^{-1}.[34] The effect of PLID to stainless steel was studied by Yang,[35] who found a logarithmic relationship between the cooling rates and feature sizes for the formation of sub-micrometer grains. Regression of his results suggests cooling rates of about 10^7 K s^{-1} to be necessary for the generation of γ-Fe nanofibers like those found in SSLIPSS. Besides γ-Fe reorganization rapid thermal cycling is known to inflict phase separations in austenitic stainless steel, because ferrite is the initial phase that occurs at the solidification contour of the melt.[36] Ferrite contents in steel can be analyzed by superconducting quantum interference device (SQUID)-magnetometry. We found that the formerly paramagnetic behavior of austenitic steel was changed to a ferromagnetic characteristic after fringe pattern impact, thus indicating ferrite precipitation (Figure 2d). Calculations based on area normalized saturation magnetization (Figure 2e) yielded an average ferrite film thickness of 198 nm to be present in SSLIPSS, so we deduced that the liquefied film during SSLIPSS formation had at least the same thickness. A low coercivity of 80 Oe and a weak deblocking at 240 K indicate a very fine granularity of ferrite. This tendency to superparamagnetism is attributable to very small magnetic domain sizes of about 6 nm, estimated by a Langevin fit (Figure 2f). Details of these analyses are provided in Supporting Information, Section 6. The presence of ferrite in SSLIPSS is also reflected in its XPD pattern, which shows an additional body-centred cubic (bcc)-phase, which was not found in untreated steel. Crystallite sizes between 5.4 and 12.8 nm were derived for
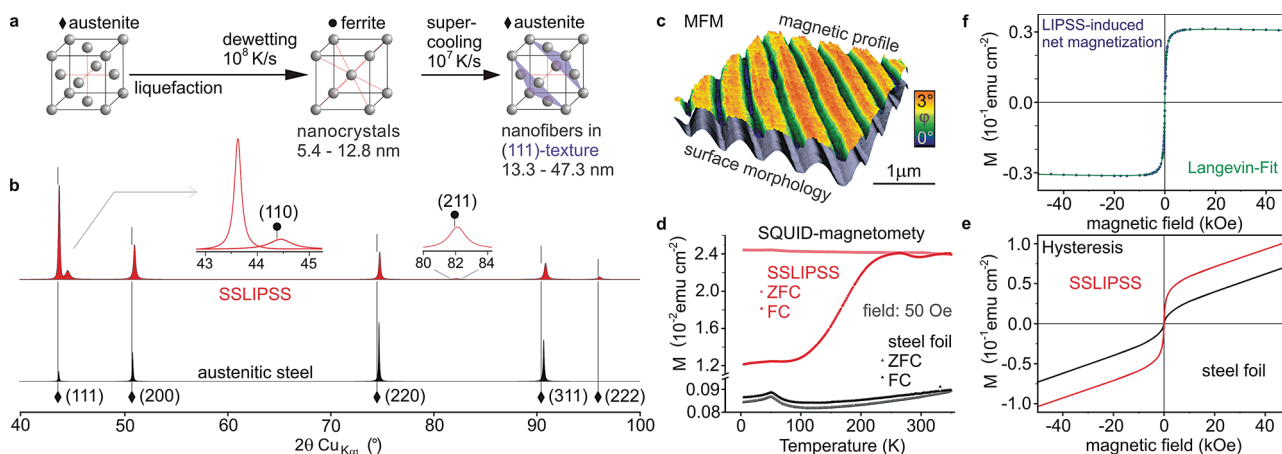
Figure 2. Crystal structure analysis and magnetic properties of SSLIPSS. a) Dewetting scenario and phase separation of stainless steel at a glance. b) X-ray diffraction patterns of stainless steel and SSLIPSS indicate ferrite precipitation, grain refinement and texture evolution as a result of laser modification; see Supporting Information, Section 3–5. c) Magnetic force microscopy (MFM) on SSLIPSS visualizes sub-micrometer magnetic patterning (detected by phase shift), which is attributed to site-specific precipitation of magnetic ferrite nanocrystals. d) LIPSS-modification of steel induces significant changes of its magnetic properties. Zero-field-cooling (ZFC) and field-cooling (FC) measurements at a field of 50 Oe show paramagnetic behavior for untreated steel, while ZFC-FC for SSLIPSS indicates a ferromagnetic behavior. e) Magnetic hysteresis loops show a distinct increase of saturation magnetization after LIPSS modification, while the coercivity remains nearly unchanged. f) The LIPSS-induced net magnetization was calculated by subtraction of the magnetic background of virgin steel from this measured for SSLIPSS. Corrected data were fitted using a Langevin function in order estimate the magnetic domain size, which came out to be about 6 nm.
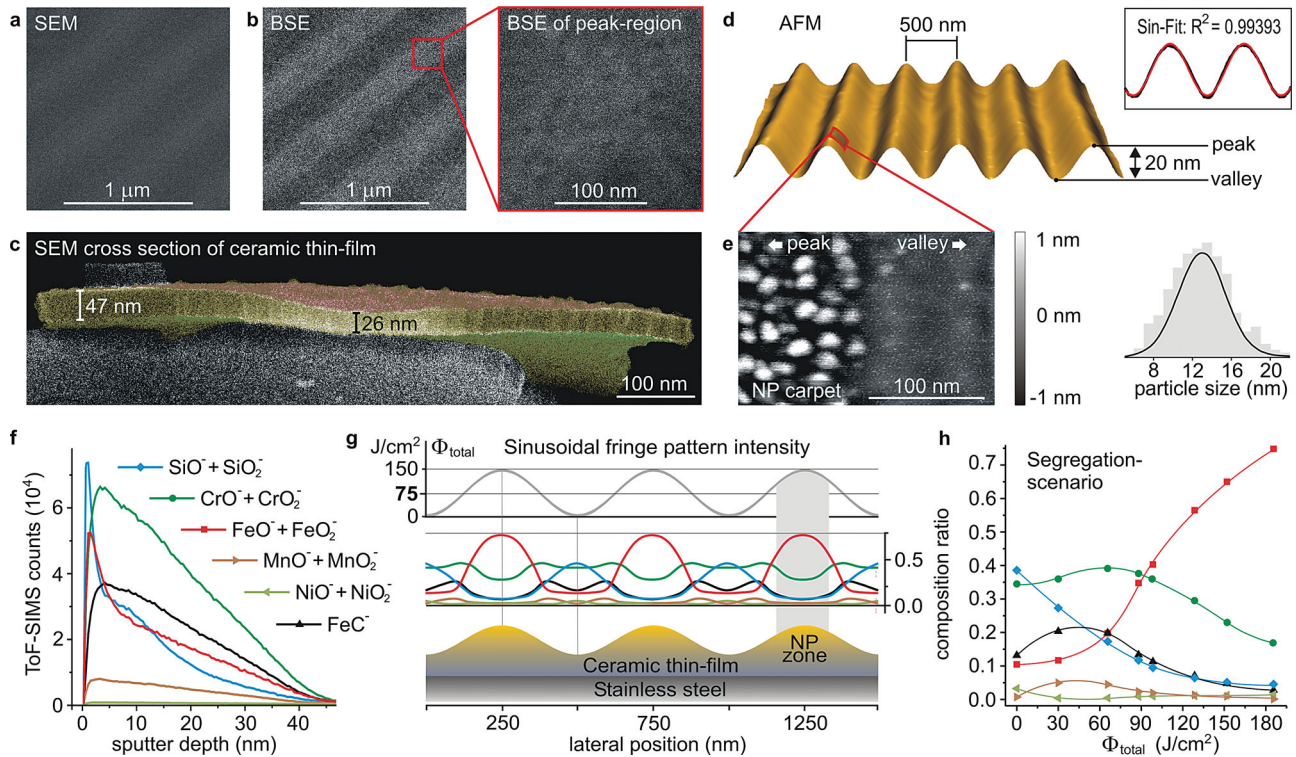
Figure 3. Morphological and compositional analyses of SSLIPSS. a) A plane view SEM-inspection of SSLIPSS gives just a vague idea of a patterned surface. b) When the same region is visualized by backscattered electron imaging (BSE) a periodic structure is ascertained by the material contrast between peak- and valley-regions of SSLIPSS. c) LIPSS-modification creates ceramic thin-films on stainless steel that can be exfoliated from the substrate by severe mechanical stress. Film thicknesses between 19 and 52 nm were determined by several measurements. d) The topography of SSLIPSS, analyzed by atomic force microscopy (AFM), shows a nearly sinusoidal waveform with a peak-to-valley amplitude of 20 nm and a periodicity of 500 nm. e) An AFM scan on a single wave section revealed nanoparticles on the peaks of SSLIPSS that are similar to those found by high resolution BSE. The Gaussian size distribution determined for nanoparticles is given on the right. f) The ToF-SIMS depth profile obtained from a ceramic thin-film on SSLIPSS shows a complex layering with transversal inhomogeneities. Each compound analyzed by ToF-SIMS is coded by a specific color. This color-code is maintained throughout the study. g) The composition model (center) provides insights into the chemical surface patterning of SSLIPSS. It is derived from investigated relations between Φ_{total} and thin-film composition. h) The composition of ceramic thin films on stainless steel is essentially controlled by the laser Φ_{total}. In order to analyze this relation we extracted ToF-SIMS depth profiles from 8 samples irradiated at different Φ_{total} and combined the results in the graph (see Supporting Information, Section 7 for details).

this bcc-phase using the Scherrer estimation. Particles of that size require cooling rates of about 10^8 K s^{-1} for self-assembly,[35] since the dewetting process must be terminated in the state of nucleation. It can therefore be stated that ferrite precipitation is restricted to regions where maximum cooling rates occur. This is most likely to happen in zones of maximum fringe pattern intensity, thus inflicting massive thermal gradients that rapidly diffuse by multidirectional heat dissipation. The hypothesis was substantiated by magnetic force microscopy (MFM) that contrasted regions in which ferrite precipitation took place (Figure 2c). Evidently, zones of maximal magnetization coincide with morphological peak regions, thus indicating a close correlation between structural transformations and morphological aspects of SSLIPSS. This discovery may be explained by the fact that grain refinement leads to an increase of grain boundaries, which inflicts stress in the crystalline structure. Stress enforces volume expansions that shape the surface morphology according to the local amount of stress, which is governed by the intensity profile of the fringe pattern stimulus. In addition to that, structural transformations were found to

determine morphological aspects on a secondary hierarchical level of SSLIPSS. High-resolution AFM scans revealed carpets of closely spaced nanoparticles covering the peak regions of SSLIPSS (**Figure 3**e). These nanoparticles are comprised of iron oxide, as will be shown in the next section, and feature a median particle size of 13 nm. Considering that iron undergoes a volume increase of approximately 30% when oxidized, makes a direct connection between ferrite patterns and nanoparticle carpets obvious. Full oxidation renders ferrite nanocrystals in the determined size range between 5.4 and 12.8 nm into iron oxide particles between 5.9 and 14 nm, a range that is covered by the size distribution of iron oxide nanoparticles found in peak regions. Based on these relationships, we conclude that morphological aspects of SSLIPSS are predetermined by structural transformations that result from site-specific dewetting scenarios governed by the local fringe pattern intensity.

Now that structural and morphological patterns of SSLIPSS are disclosed, it is reasonable to raise the question whether chemical patterning is yet another effect resulting from a spatio-temporal stimulus. Photothermal excitation by a fringe
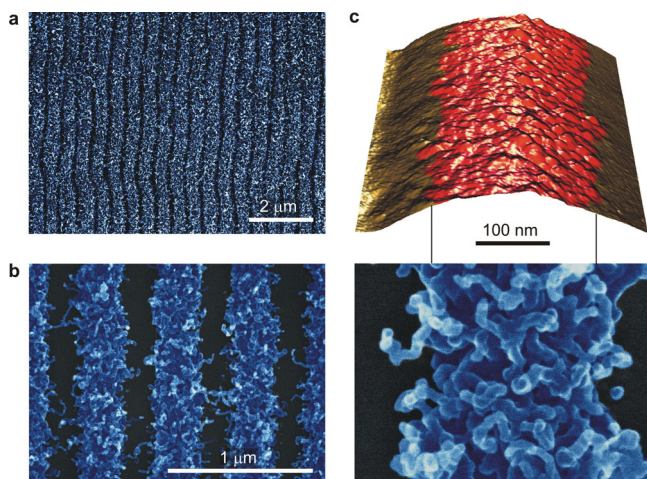
Figure 4. Catalytic properties of SSLIPSS. a) The result of thermal CVD accounts for the existence of site-selective catalytic activity on SSLIPSS-substrates. b) Patterned CNT growth is observed in parallel lanes with a periodicity of 500 nm. c) The upper picture shows an AFM topography taken from a peak region of SSLIPSS prior to CVD. A correlation between CNT growth (lower picture) and the zone of catalytically active iron-oxide NPs (red) is obvious. The scale bar applies for both pictures in (c) likewise.

pattern causes not only transformations in stainless steel but also surface reactions with the surrounding medium. For the investigated model system this is primarily the reaction of steel components with oxygen from air, which leads to the formation of ceramic thin films on the steel surface. Cross sections of such films exfoliated from a SSLIPSS substrate are given in Figure 3c. The splinter-like fractures show different layer thicknesses indicating that the periodic wave structure of LIPSS is manifested in the ceramic thin-film. ToF-SIMS depth profiling (Figure 3f) revealed a composition of Cr-, Fe- and Si-oxides as well as FeC that is characterized by transversal inhomogeneity. Unfortunately, the lateral resolution of ToF-SIMS is insufficient for chemical diversification between peak and valley regions. Despite this problem chemical patterning of SSLIPSS has been verified. The prerequisite for this approach is a precise understanding of the dynamics of laser-induced thin film growth. The extent of laser-induced reactions between stainless steel and air is essentially controlled by the total laser fluence Φ_{total}. An analysis of the relationship between surface composition and Φ_{total} is given in Figure 3h. Accordingly, laser treatment with low Φ_{total} leads to a surface composition that is dominated by Cr- and Si-oxides, whereas an accumulation of Fe-oxides is found when Φ_{total} is continuously increased. Once the correlation between Φ_{total} and chemical alteration is analyzed for a system, this knowledge can be used to predict the type of chemical patterning that is to be expected after fringe pattern impact. Doing this for our system under the assumption of a sinusoidal fringe pattern intensity profile gives insights into the spatial segregation scenario of SSLIPSS. The results, presented in Figure 3g, display a well defined chemical surface patterning. Obviously, the peak regions of SSLIPSS are primarily composed of iron oxide in solid solution with chromium oxide, while valley regions consist of chromium oxide and silica.

It should be mentioned that this model represents a semi-empirical approach for pattern prediction because appropriate methods for compositional analysis with spatial resolution on the nanoscale are barely available. Having this model in mind we checked related surface properties. There is, for example, a good correlation to the material contrast visualized by BSE (Figure 3b), which indicates a lower effective atomic number Z_{eff} in valley regions compared to the peaks of SSLIPSS. Due to the fact that the atomic number is almost equal for Cr and Fe ($Z_{Cr} = 24$ and $Z_{Fe} = 26$), a decrease of Z_{eff} must be entailed by Si ($Z_{Si} = 14$) which, according to the model, preferably occurs in the valleys. Another validation for the model is based on its prediction that nanoparticles observed in peak-regions of SSLIPSS essentially consist of iron-oxide and thus represent a catalyst for carbon nanotube (CNT) growth.[37] Patterned CNT-growth on SSLIPSS was actually achieved by chemical vapor deposition (CVD) as demonstrated in **Figure 4**. Both results substantiate the validity of the model, thus making this approach attractive for the prediction of LIPSS-induced chemical patterning on other systems as well.

Besides surface modifications presented so far, the investigated SSLIPSS substrate provides another effect that was found to be advantageous for template applications. Templates frequently paved the way of nanotechnology from fundamental research to technological implementations. However, the choice of templates accessible by simple and cost efficient processes is limited. For this reason we would like to introduce LIPSS as a novel technique for template generation. The concept is based on the finding that the thickness of laser-induced ceramic thin-films on stainless steel is essentially controlled by Φ_{total}. Accordingly, irradiation under LIPSS-conditions is likely to create a ceramic coating with periodically varying film thicknesses corresponding to the fringe pattern intensity profile. Since the dielectric strength of ceramic thin-films is basically a function of layer thickness we expected a pattern of periodically alternating electrical resistance on SSLIPSS. This assumption was confirmed by conductive atomic force microscopy (CAFM). Contact scans with a biased tip inflicted electrical breakdowns exclusively in the valley regions of SSLIPSS (**Figure 5**a). Surfaces with spatially varying conductivity on the submicron scale are sought-after substrates for template applications;[38] the most prominent is porous anodic alumina.[39] Structured electrodes are interesting for electrochemical applications as they provide spatial reaction control. An example is given by the site-specific electrodeposition of silver nanoparticles on a SSLIPSS substrate. Prior to this experiment linear sweep voltammetry and CAFM were performed to identify electrode potentials suitable for patterned deposition (see Supporting Information, Section 8–10). Good results were obtained at a bias of −1.4 V in an aqueous electrolyte containing 0.1 M KNO₃ and 5.8 mM AgNO₃. The condition provides site-specific Ag⁺ reduction yielding precise silver nanoparticle patterns in the valley regions of SSLIPSS (Figure 5b). Implementations of such structures into functional systems are facilitated by the possibility of pattern transfer to secondary substrates like PDMS or SU8 as it is demonstrated in Figure 5c. This opportunity combined with the diversity of materials accessible by electrochemical deposition prospects a broad application potential for templates generated by the LIPSS-process.

Materials
Views
www.MaterialsViews.com

ADVANCED
MATERIALS
www.advmat.de

COMMUNICATION
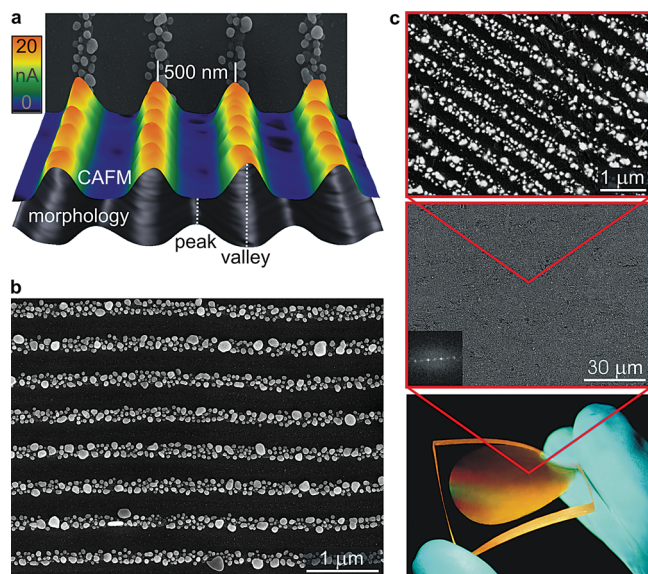
Figure 5. Electrical Properties of SSLIPSS. a) Conductive atomic force microscopy (CAFM) on SSLIPSS revealed increased current flows in valley regions of SSLIPSS at a tip bias of 3 V. This site-specific current flow confines electrochemical processes to the valley regions. b) Electrochemical reduction of Ag^+ results in patterned silver-nanoparticle deposition predefined by the SSLIPSS-substrate. c) A transfer of deposited material to secondary substrates is promoted by low adhesion of nanoparticles to the SSLIPSS-substrate. A large-area replica of silver nanoparticle patterns fixed in PDMS is shown at the bottom. SEM inspections (center and top) prove pattern conservation with low numbers of defects.

The introduced concept of self-organized pattern formation in multicomponent systems is evidently very prolific. Using the example of stainless steel, we demonstrated the potential of LIPSS as a process for simple and cost-efficient generation of multifunctional surfaces. Apart from the system investigated here arbitrary combinations of subsystems may be considered for patterning by LIPSS. Prospective approaches benefit from the opportunity to create custom tailored reactive systems that enable for surface modifications with pre-defined functionality. The design flexibility is further enhanced by the wide scalability of self-organized pattern formation thus allowing for adaption to respective requirements. Addressable feature sizes of LIPSS patterns span the microgap to nanogap and depend on parameters such as laser wavelength, angle of incidence, pulse width and refractive index of the irradiated system. Pattern periodicities down to 20 nm have been demonstrated recently.[40,41] Moreover, the LIPSS-process is not restricted to line patterns as presented in this study. Pattern shapes are basically controlled by the type of laser polarization that is used during LIPSS-generation. Dot- and cross-patterns,[42,43] circles and spirals[44,45] and even hierarchical patterns[46] have been realized so far.

Experimental Section

Composition of Austenitic Stainless Steel Type EN 1.4301 (AISI 304): Cr 17–19.5 wt%, Ni 8–10.5 wt%, Mn <2 wt%, Si <1 wt%, N <0.1 wt%, C <0.07 wt%, S <0.015 wt%, Fe balance.

Formation of SSLIPSS: A Nd:YVO$_4$ DPSS nanosecond laser (Explorer XP 532-5, Newport, USA) emitting a wavelength of 532 nm was utilized

for LIPSS formation on stainless steel. A detailed description of the process is given in the Supporting Information, section 2.

Morphological Analysis: Scanning electron microscopy (SEM) inspection was performed using a field-emission microscope (JSM-7500F, Jeol, Japan) equipped with a backscattered electron detector (YAG, Autrata, Czech Republic) for material contrast imaging by means of effective atomic number contrast Z_{eff}.

Atomic force microscopy (AFM) was performed using a Nanoscope IV (Bruker, USA) instrument, using SCM-PIT tips (antimony n-doped Si, 0.01–0.025 Ω, k = 1-5 N m^{-1}, f_0 = 70–83 kHz, Bruker) in tapping mode.

Topological mapping of substrate surfaces was performed using a laser scanning microscope (LSM 5 Pascal, Carl Zeiss, Germany).

Composition Analysis: Time-of-flight secondary-ion-mass-spectrometry was employed to determine the composition of ceramic thin-films on stainless steel using a ToF-SIMS^4 mass spectrometer from Ion-ToF, Germany. Detailed information concerning the measurement procedures and the disclosure of chemical patterning on SSLIPSS are provided in the Supporting Information, Section 7.

Crystal Structure Analysis: X-ray diffraction studies were carried out using a Philips X-Pert MPD Pro powder diffractometer equipped with an X-Pert tube Cu LFF operating at 40 kV and 40 mA. Spectra were obtained in the range of $40° ≤ 2\theta ≤ 100°$ at room-temperature. Data analysis and postprocessing was conducted using X-Pert High Score Plus v2.2c and Origin Pro (see Supporting Information, Section 3–5).

Magnetic Characterizations: Macroscopic measurements were performed on a DC-SQUID (Quantum Design, USA). Magnetic force microscopy (MFM) was performed using a Nanoscope IV instrument (Bruker, USA). Details concerning data acquisition and processing are provided in the Supporting Information, Section 6.

Electrical Characterizations: Conductive atomic force microscopy (CAFM) was performed using a Solver P47 (NT-MDT, Russia) atomic force microscope. Electrochemical analysis on SSLIPSS-substrates was performed using a potentiostat/galvanostat (EG&G 273A, Princeton Applied Research, USA) (see Supporting Information, Section 8–9).

Template Processes: CNT growth was conducted by a thermal chemical vapor deposition (CVD) process. Spatially selective precipitation of silver nanoparticles was obtained by cathodic reduction of a silver nitrate solution. Supporting information, Section 10 provides detailed descriptions of both processes.

Supporting Information

Supporting Information is available from the Wiley Online Library or from the author.

[1] J. Reinitz, *Nature* **2012**, *482*, 464.

[2] B. S. Glick, *Nat. Cell. Biol.* **2007**, *9*, 130–132.

[3] S. Robinson, P. B. de Reuille, J. Chan, D. Bergmann, P. Prusinkiewicz, *Science* **2011**, *333*, 1436–1440.

[4] R. Madueno, M. T. Räisänen, C. Silien, M. Buck, *Nature* **2008**, *454*, 618–621.

[5] M. Takahashi, C. Figus, T. Kichob, S. Enzo, M. Casula, M. Valentini, P. Innocenzi, *Adv. Mater.* **2009**, *21*, 1732–1736.

[6] S. Kondo, T. Miura, *Science* **2010**, *329*, 1616–1620.

[7] L. Corté, P. M. Chaikin, J. P. Gollub, D. J. Pine, *Nat. Phys.* **2008**, *4*, 420–424.

[8] C. Jung, P. Schwaderer, M. Dethlefsen, R. Köhn, J. Michaelis, C. Bräuchle, *Nat. Nanotechnol.* **2011**, *6*, 87–92.

[9] K. R. Hebert, S. P. Albu, I. Paramasivam, P. Schmuki, *Nat. Mater.* **2012**, *11*, 162–166.

[10] G. Pawin, K. L. Wong, K.-Y. Kwon, L. A. Bartels, *Science* **2006**, *313*, 961–962.

[11] J. Becker, G. Grün, R. Seemann, H. Mantz, K. Jabobs, K. R. Mecke, R. Blossey, *Nat. Mater.* **2003**, *2*, 59–63.

[12] Z. Nie, A. Petukhova, E. Kumacheva, *Nat. Nanotechnol.* **2010**, *5*, 15–25.

[13] S. Mann, *Nat. Mater.* **2009**, *8*, 781–792.

[14] R. M. Erb, H. S. Son, B. Samanta, V. M. Rotello, B. B. Yellen, *Nature* **2009**, *457*, 999–1002.

[15] P. F. Damasceno, M. Engel, S. C. Glotzer, *Science* **2012**, *337*, 453–457.

[16] H.-C. Kim, H. M. Reinhardt, P. Hillebrecht, N. A. Hampp, *Adv. Mater.* **2012**, *24*, 1994–1998.

[17] J. K. W. Yang, Y. S. Jung, J-B. Chang, R. A. Mickiewicz, A. Alexander- Ketz, C. A. Ross, K. K. Berggren, *Nat. Nanotechnol.* **2010**, *5*, 256–260.

[18] W. Bao, F. Miao, Z. Chen, Z. Hang, W. Jang, C. Dames, C. N. Lau, *Nat. Nanotechnol.* **2009**, *4*, 562–566.

[19] S. Kim, S. Lee, J. Ko, J. Son, M. Kim, S. Kang, J. Hong, *Nat. Nanotechnol.* **2012**, *7*, 567–571.

[20] M. Birnbaum, *J. App. Phys.* **1965**, *36*, 3688–3689.

[21] J. F. Yong, J. S. Preston, H. M. van Driel, J. E. Sipe, *Phys. Rev. B* **1983**, *27*, 1155–1172.

[22] J. V. Obona, V. Ocelík, J. Z. P. Skolski, V. S. Mitko, G. R. B. E. Römer, A. J. Huis in't Veld, J. Th. M. De Hosson, *Appl. Surf. Sci.* **2012**, *258*, 1555–1560.

[23] G. Miyaji, K. Miyazaki, K. Zhang, T. Yoshifuji, J. Fujita, *Opt. Express* **2012**, *20*, 14848–14856.

[24] E. Rebollar, S. Pérez, J. J. Hernández, I. Martin-Fabiani, D. R. Rueda, T. A. Ezquerra, M. Castillejo, *Langmuir* **2011**, *27*, 5596–5606.

[25] J. Bonse, A. Rosenfeld, J. Krüger, *J. Appl. Phys.* **2009**, *106*, 104910.

[26] D. C. Emmony, R. P. Howson, L. J. Willis, *Appl. Phys. Lett.* **1973**, *23*, 598–601.

[27] N. R. Isenor, *Appl. Phys. Lett.* **1977**, *31*, 148–151.

[28] M. Huang, F. Zhao, Y. Cheng, N. Xu, Z. Xu, *ASC Nano* **2009**, *3*, 4062–4070.

[29] M. Straub, M. Afshar, D. Feili, H. Seidel, K. König, *J. Appl. Phys.* **2012**, *111*, 124315.

[30] M. R. Barnett, L. Kestens, *Texture. Microstruct.* **2000**, *34*, 1–22.

[31] C. Cui, J. Hu, Y. Liu, Z. Guo, *Appl. Surf. Sci.* **2008**, *254*, 3442–3448.

[32] J. A. F. Plateau, *Statique Expérimentale et Théorique des Liquides Soumis aux Seules Forces Moleculaires*, Gauthiers-Villars, Paris **1873**.

[33] L. Rayleigh, *Philos. Mag.* **1892**, *34*, 145–154.

[34] J. D. Fowlkes, L. Kondic, J. Diez, Y. Wu, P. D. Rack, *Nano Lett.* **2011**, *11*, 2478–2485.

[35] J. Yang, J. Lian, Q. Dong, Z. Guo, *Appl. Surf. Sci.* **2004**, *229*, 2–8.

[36] A. S. C. M. d'Oliveira, R. S. C. Paredes, F. P. Weber, R. Vilar, *Mater. Res.* **2001**, *4*, 93–96.

[37] M. Mohapatra, S. Anand, *Int. J. Eng. Sci. Tech.* **2010**, *2*, 127–146.

[38] H. Kim, J. Kim, H. Yang, J. Suh, T. Kim, B. Han, S. Kim, D. S. Kim, P. V. Pikhitsa, M. Choi, *Nat. Nanotechnol.* **2006**, *1*, 117–121.

[39] W. Lee, R. Ji, U. Gösele, K. Nielsch, *Nat. Mater.* **2006**, *5*, 741–747.

[40] S. Shazia Bashir, M. Shahid Rafique, W. Husinsky, *Phys. Res. B* **2012**, *275*, 1–6.

[41] J. Bonse, J. Krüger, S. Höhm, A. Rosenfeld, *J. Laser Appl.* **2012**, *24*, 042006-1-042006-7.

[42] K. Nishioka, S. Horita, *Appl. Phys. A* **2008**, *91*, 235–240.

[43] M. Rohloff, S. K. Das, S. Höhm, R. Grundwald, A. Rosenfeld, J. Krüger, J. Bonse, *J. Appl. Phys.* **2011**, *110*, 014910-1-014910-4.

[44] K. Lou, S.-X. Qian, Z.-C. Ren, X.-L. Wang, Y. Li, C. Tu, H.-T. Wang, *J. Opt. Soc. Am. B* **2012**, *29*, 2282–2287.

[45] J.-T. Chen, W. C. Lai, Y. J. Kao, Y. Y. Yang, J. K. Sheu, *Opt. Exp.* **2012**, *20*, 5689–5695.

[46] J. Z. P. Skolski, G. R. B. E. Römer, J. V. Obona, V. Ocelik, A. J. Huis in't Veld, J. Th. M. De Hosson, *Phys. Rev. B* **2012**, *85*, 075320-1-075320-9.

Supporting Information

Self-Organization of Multifunctional Surfaces - The Fingerprints of Light on a Complex System

Hendrik M. Reinhardt, Hee-Cheol Kim, Clemens Pietzonka, Julia Kruempelmann, Bernd Harbrecht,

Bernhard Roling & Norbert A. Hampp

Department of Chemistry, Philipps-University of Marburg
Hans-Meerwein-Str., D-35032 Marburg, Germany

1 Concept of LIPSS-induced pattern formation in complex systems

A system that is subjected to an extrinsic stimulus reacts in a certain way of transformation that is governed by boundary conditions. For a system consisting of several chemical species in various states of energy and order, a multitude of transformations is to be expected. This study introduces the concept of triggering such transformations by a stimulus of periodically varying light intensity and demonstrates its potential by means of multi-functionalization of stainless steel surfaces. Intended as guidance through the study an overview is given in **Fig. S1**.
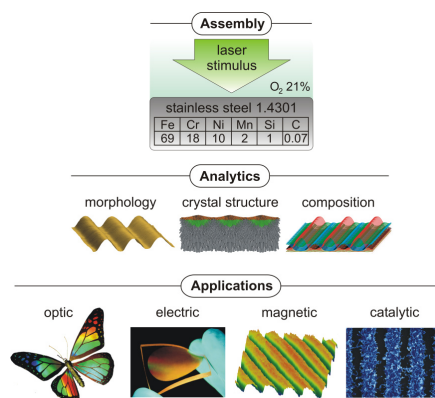
Figure S1 Outline and Summary

Our general approach is characterized by a low effort - high outcome strategy using the concept of multi-hierarchical self-organization in a complex system. "Assembly" illustrates the patterning of our model system steel/air by the LIPSS-process. "Analytics" abstracts the range of pattern analysis presented in this study and "Applications" review SSLIPSS implementations that were derived from pattern analysis and are shown exemplarily.

2 Large-area LIPSS-formation

Besides numerous efforts to elucidate the origin of LIPSS, this unique self-organizing process has received increasing attention in recent years. Its simplicity and its inherent potential for advanced surface modification make the LIPSS-phenomenon very attractive for technical applications. A major hurdle that needs to be taken on the way to practical application is up-scaling, or in other words, LIPSS-formation on large surface areas. The fact that LIPSS-generation is a laser based process and thus a spatial selective surface modification typically covering areas of several square micrometers makes homogeneous LIPSS-formation on areas in the range of square centimeters initially difficult. In order to solve this problem we applied a dynamic process for LIPSS generation that is described in below:

A Nd:YVO$_4$ DPSS nanosecond laser (Explorer XP 532-5, Newport, USA) emitting a wavelength of 532 nm in spatial mode TEM$_{00}$ ($M^2 < 1.1$) at a 50 kHz pulse repetition rate and a pulse width of 6 ns was employed for SSLIPSS generation. The beam was scanned over stainless steel samples with a constant line spacing of 3 μm by a galvanometer scanner (SCANgine 14-532, Scanlab, Germany). Focusing by a F-Theta lens with 163 mm focal length (Ronar-532-163, Rodenstock, Germany) under focal offset conditions projected an effective spot size of 30 μm diameter (≈ 706 μm^2) on the sample surface. The average laser power delivered to the surface was measured by a power meter (FieldMax II with an LM-80V detector head, Coherent, USA) to be 1040 mW, thus giving a pulse energy of 20.8 μJ and a laser fluence ϕ_{pulse} of 2.95 J cm^{-2} (single pulse). LIPSS generation on stainless steel was found for line scan speeds between 270 mm s^{-1} and 610 mm s^{-1}, optimum conditions were achieved at 460 mm s^{-1} (single line spot overlap about 70 %). The total laser fluence Φ_{total} for an area converted to SSLIPSS was calculated as the factor of average laser power and overall irradiation time for a certain area. Accordingly, optimum SSLIPSS was achieved at $\Phi_{total} = 75.36$ J cm^{-2}. Actually, LIPSS generation is the consequence of a feedback mechanism that is triggered by a certain number of overlapping laser pulses at a given laser fluence ϕ_{pulse}. By the fact that a dynamic process was applied for LIPSS generation in this study, these characteristic values can only be derived statistically. Accordingly, an average number of 25.57 laser pulses at a laser fluence of $\phi_{pulse} = 2.95$ J cm^{-2} is necessary to convert an area the size of a laser spot footprint (706 μm^2) to optimum SSLIPSS.

One might argue that industrial grade stainless steel is not very suitable for nanostructure formation due to its surface inhomogeniety and granular structure. **Figure S2** shows pictures of stainless steel with LIPSS modification (SSLIPSS) taken by optical phase-contrast microscopy (**Fig. S2b, S2c**). Although the treated steel surface presents a rather disordered morphology at first glance there is a regularity to be found when fast-Fourier-transformation is applied (see figure inset). An image taken at higher magnification, presented in **Fig. S2c**, reveals the origin of this Fourier pattern: clearly defined LIPSS that cover the full steel surface and actually span across grain boundaries. This shows that dynamic LIPSS-formation by a scanned laser spot is a robust process. Homogeneous LIPSS modifications that cover surface areas of several square centimeters prove the general applicability of the introduced process for technical applications; examples are given in **Fig. S2d-h**. To our knowledge the extention of LIPSS to areas of that size was not demonstrated so far. The diffraction properties of SSLIPSS provide a useful quality indicator especially for applications striving for large scale LIPSS-formation
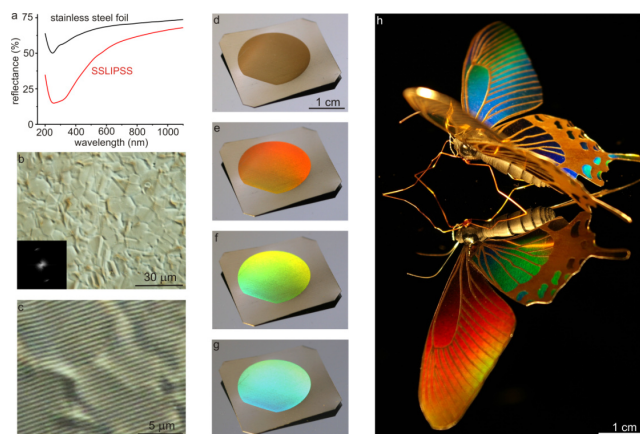
Figure S2. Large-area LIPSS-modification on stainless steel
a, UV-VIS-spectra of stainless steel foil before and after and LIPSS modification **b,** optical phase-contrast microscopy of SSLIPSS and fast-fourier-transformation of the image (inset) **c,** high resolution optical phase-contrast microscopy of SSLIPSS **d,** picture of steel foil with LIPSS-modification (brownish area) **e-g,** the same sample illuminated in angels providing diffraction **h,** model of Papilio Maackii Menetries buildt from LIPSS modified steel foil

3 Rietveld analysis of SSLIPSS

Laser irradiation causes changes in the crystalline structure of stainless steel that are attributed to rapid surface melting and resolidification. The effect of this process was analyzed by X-ray powder diffraction (XPD). **Figure S3** shows the diffraction patterns obtained from untreated stainless steel and SSLIPSS for comparative purpose.
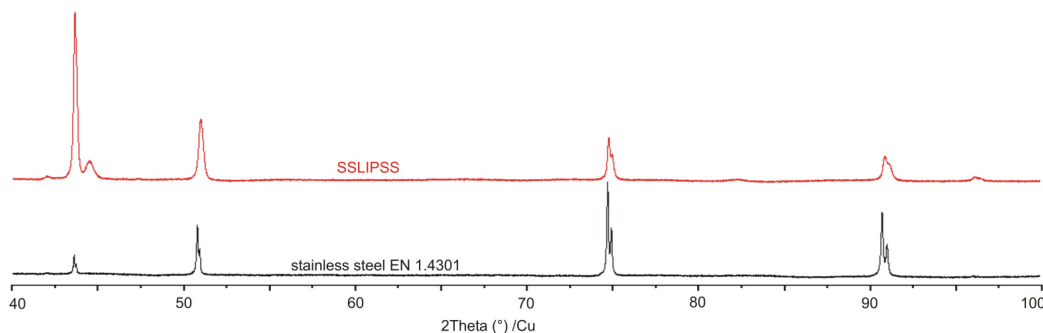
Figure S3. Diffraction patterns of stainless steel and SSLIPSS as obtained from the X-ray spectrometer

Rietveld analysis (**Fig. S4**) yielded distinct phase and texture modifications to occur as a result of laser irradiation of stainless steel. The lattice parameter of 360.4(3) pm determined for the austenite phase (fcc) of untreated stainless steel EN 1.4301 (AISI 304) shows a decrease to 358.5(3) pm after laser irradiation. Moreover, SSLIPSS features an additional bcc phase with a lattice parameter of 287.4(5) pm that is not found in virgin steel. Thermal treatment of stainless steel EN 1.4301 is known to inflict δ-ferrite precipitation, which is a bcc phase of iron. However, it must be noted that EN 1.4301 contains other elements beyond iron, therefore the bcc phase is not expected to be pure δ-ferrite.
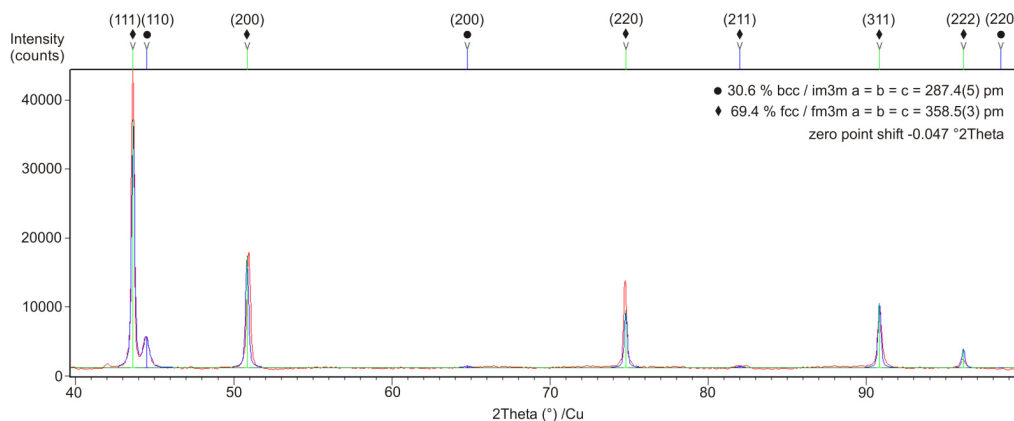
Figure S4. Rietveld analysis of SSLIPSS diffraction pattern

4 Crystallite size determination of SSLIPSS

Crystallite sizes for fcc and bcc phases of SSLIPSS were determined using the Scherrer crystallite size estimation (SCSE). The reflection profile analysis is given in **Fig. S5**. Full width half maxima (FWHM) of all reflections were obtained from Lorenz-Fits of X-ray diffraction data. For crystallite size calculation based on FWHM a form factor of $k = 0.9$ was used. Accordingly the fcc-phase of SSLIPSS features crystallite sizes between 13.3 and 47.3 nm, thus indicating shape anisotropy. Crystallite sizes obtained for the bcc phase were even smaller and show shape anisotropy as well. The mean size of bcc-crystallites was determined to be 9.1 nm.
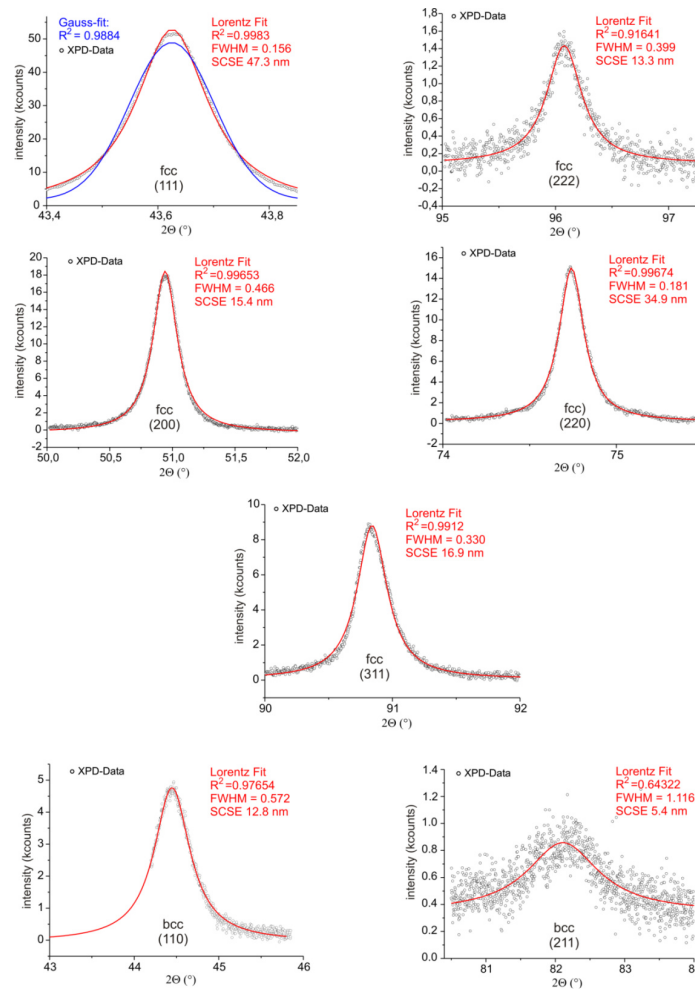

Figure S5. Reflection profile analysis of SSLIPSS and particle size determination by Scherrer crystallite size estimation (SCSE)

5 Laser-induced texture formation in steel

Surface texturing of stainless steel is yet another effect observed as a result of laser irradiation. **Figure S6** shows the evolution of fcc-(111), fcc-(200) and bcc-(110) XPD reflections as a function of laser irradiation. A continuous increase of intensity is obvious for fcc-(111) and bcc-(110) while the diffraction intensity of fcc-(200) remains nearly unchanged. This indicates epitaxial growth of austenite in (111) and ferrite in (110) orientation respectively.
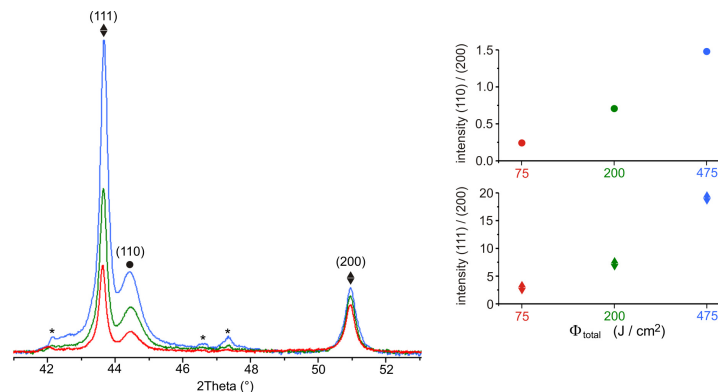

Figure S6. Φ_{total} -dependent evolution of laser-induced texture in stainless steel, SSLIPSS is colored in red

$* = Cr_7C_3$ (JCPDS Card 11-550)

76

6 Magnetic characterization of SSLIPSS

SQUID measurements (Superconducting QUantum Interference Device) were conducted with steel foils of 50 μm thickness that were mounted in parallel orientation with respect to the direction of the magnetic field. The ZFC (zero field cooling) magnetization was obtained by cooling of the sample to 2.5 K followed by slowly heating in the presence of a weak field of 50 Oe. The FC (field cooling) magnetization of the sample was measured while cooling the sample down to 2.5 K in at 50 Oe. Magnetic hysteresis loops were obtained at 300 K in a range of ± 50 kOe. In order to determine the net magnetization induced by LIPSS modification of stainless steel we subtracted measurements of virgin steel foil from measurements of modified steel foil.

Calculation of the area-normalized magnetization (M_A):

$$M_A = M_{abs} \cdot \rho_{V2A} \cdot d_{V2A} \cdot m^{-1}$$

M_{obs} represents the measured magnetization of the sample in electromagnetic units (emu), whereas ρ_{V2A} is the density of stainless steel (7.9 g cm^{-3}), d_{V2A} the thickness of the steel foil (50 μm) and m the mass (g) of the sample, respectively.

Calculation of the bcc-phase layer thickness:

The thickness of the magnetic layer was derived from the saturation magnetization (M_{sat_A}) with respect to the atomic volume (V_{at}) and the magnetic moment (μ_{at}) of one atom in the bcc lattice. For α-Fe the value is 2.2 Bohr magnetons, bcc phases of $Fe_{0.9}Ni_{0.1}$ and $Fe_{0.8}Cr_{0.2}$ feature values of 2.1 and 1.7 BM, respectively [47,48]. If one assumes the bcc-phase as a solid film, the thickness (d) can be calculated by equation:

$$d = \frac{M_{sat_A} \cdot emu \cdot cm^{-2} \cdot V_{at} \cdot cm^3}{\mu_{at} \cdot BM \cdot \mu_B \cdot emu \cdot BM^{-1}}$$

μ_B is the magnetic moment of Bohr magneton with the value $9.27 \cdot 10^{-21} emu \cdot BM^{-1}$.

Determination of the magnetic domain size by the Langevin function:

The magnetization depending on external field (H_0) and temperature (T) in a system of macroscopic magnetic moments can be described by the Langevin function with respect to the average magnetic moment (μ) of a particle.

$$m = m_{sat} \cdot \left(\frac{\coth(a) - 1}{a} \right)$$

$$a = \frac{\mu H_0}{k_B}; \quad (k_B: Boltzman\ constant)$$

Fig. S7 shows the area-normalized net magnetization resulting from laser treatment of stainless steel with Φ_{total} = 75.36 J cm^{-2} (SSLIPPS-formation fluence). The Langevin-fit delivered the following values:

$$m_{sat} = 0.0311\ emu$$
$$\mu = 2.0089 \cdot 10^{-16} emu = 21670\ BM$$

μ represents the average magnetic moment of a domain. Taking into account V_{at} and μ_{at}, the volume of a magnetic domain is available.
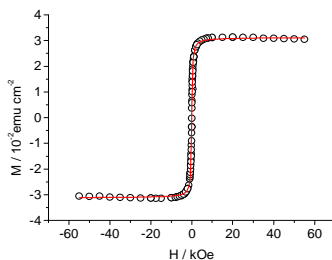
Figure S7. Langevin-fit (red line) of SQUID measurement at 300 K (circles)

[47] G. Dumpich, E. F. Wassermann, V. Manns, W. Keune, S. Murayama, Y. Miyako, *Journal of Magnetism and magnetic Materials* **1987**, *67*, 55-64.
[48] A. T. Aldred, *Physical Review B* **1976**, *14*, 219-227.

Nanomagnetic investigations of SSLIPPS

Magnetic force microscopy (MFM) was performed on a Nanoscope IV (Bruker, USA) using MESP-RC tips (antimony n-doped Si, 0.01-0.025 Ω, magnetic Co/Cr coating with coercivity of ~400 Oe, k = 5-10 N m^{-1}, f_0 = 150-200 kHz, Bruker) utilizing the LiftMode feature of the microscope. Magnetic force detection was accomplished by a two-pass procedure in which a line profile of the specimen is scanned by tapping mode in a first pass. Memorized topographic data were used to guide the second pass in a lift height of 20 nm above the previously scanned profile. Disparities in surface magnetization interfere with the magnetic tip, thus inducing cantilever deflection that was contrasted by phase detection during this noncontact scan. Topographic data are interleaved with magnetic data line by line, finally giving two correlated images.

7 Laser-induced metal oxide segregation on stainless steel EN 1.4301 (AISI 304)

When a photonic fringe pattern strikes the surface of stainless steel this induces a periodic pattern of heat zones and thus locally confined oxidation sites. Chemical separations are to be expected as a consequence of this treatment because each component of stainless steel features a different affinity to oxygen. A first clue for the occurrence of such separations can be derived from the material contrast visualized by BSE (**Fig. 3b** in the paper); however, qualitative material information is not provided. Hence, time-of-flight-secondary-ion-mass-spectrometry (ToF-SIMS) was consulted due to its capability for highly surface selective composition analysis. Compositional depth profiling was conducted using a scanned antimony-ion-beam for layer-by-layer ablation of oxide thin films. Particles ascending from the focus of the antimony-ion-beam are accelerated into the detector and analyzed by impact time thus yielding mass spectra from each sputtered point. Mass peak assignment using a database of known mass fragments finally gave the thin film composition. Prior to ToF-SIMS analysis resulting sputter craters were measured by AFM in order to correlate compositional data to the respective sputter depths, assuming a linear sputter rate, which was given due to a constant sputter current. Although it was possible to investigate the transversal composition of oxide thin films on SSLIPSS substrates (**Fig. 3f** in the paper) the lateral resolution of ToF-SIMS was not sufficient to discriminate between peak and valley regions of SSLIPSS. In order to circumvent this problem we determined thin-film compositions of another 8 stainless steel samples, each subjected to different values of Φ_{total} in the range from 0 J cm^{-2} (natural passivation layer of steel) to 185 J cm^{-2}. The extraction of composition data obtained from the outmost surface of ceramic films up to a sputter depth of 5 nm (termed as near-surface composition ratio) was used to create the relationship illustrated in **Fig. 3h** in the paper. This plot reveals the dependency of Φ_{total} to the near surface composition of laser-modified stainless steel. The observed segregation scenario in ceramic thin films can be understood from a thermodynamic point of view regarding the Gibbs free energies of oxide formation, which indicate the reactivity sequence Si>>Mn>Cr>Fe>>Ni for the components of steel. Although Si belongs to the minor alloying elements, it features the strongest oxygen affinity and thus favored oxidation even at low values of Φ_{total}. From the fact that Fe is primarily existent in a carburized form under the same irradiation conditions, we concluded that this segregation regime is governed by oxygen deficiency. Consequently, major alloying elements like Fe are barely oxidized as long as higher reactive species act as oxygen scavengers. This explains why significant iron-oxidation occurs not until Si, Mn and Cr are locally depleted.

The investigated relationship between Φ_{total} and composition was finally utilized to estimate the chemical pattern on SSLIPSS by assignments of local fringe pattern intensities (assuming a sinusoidal waveform) to composition ratios analyzed for respective values of Φ_{total}. Certainly, the accuracy of chemical pattern prediction could be improved by considering additional effectors like heat diffusion, phase transitions, nonlinearities and proximity effects, but that was not our scope here.

8 Nanoelectrical properties of SSLIPPS

Conductive atomic force microscopy (CAFM) was performed using a Solver P47 (NT-MDT, Russia) atomic force microscope. All measurements were carried out with a conductive tip (Nanosensors GmbH) in contact mode under ambient conditions. Topography and conductivity of the sample surface were simultaneously imaged. Closer examinations of the site-specific electrical properties of SSLIPSS are presented in **Fig. S8**. Current voltage curves obtained by CAFM show different electric conductivities for peak- and valley- regions of SSLIPSS. A conductive tip landed in the valley region gives a current response in the nA-range for voltages exceeding approximately|1.4 V| (green lines). In contrast to that, measurements in the peak regions show current response in the pA-range for tip voltages up to 3 V. Clearly, the current response in the peak region is more than two orders of magnitude lower than in the valley region, thus confirming the alternating electric resistance on SSLIPSS as demonstrated by the CAFM area scan illustrated in **Fig. 5a** in the paper. The effect is attributed to alternating thicknesses of the ceramic coating on the steel surface, which are about 45 nm in peak- and about 25 nm in valley regions. Beyond higher film thickness the low conductivity on the peaks seems to be attributed to its special arrangement as well. Scanning polarimetry showed that peaks exhibit resistive properties differing from the classical ohmic behavior. The effect may be attributed to matrix embedded nanoparticles that were found solely in peak regions. Randomly oriented grain boundaries are known to form back-to-back diode pairs that allow only tiny current flows owing to reversed leakage.
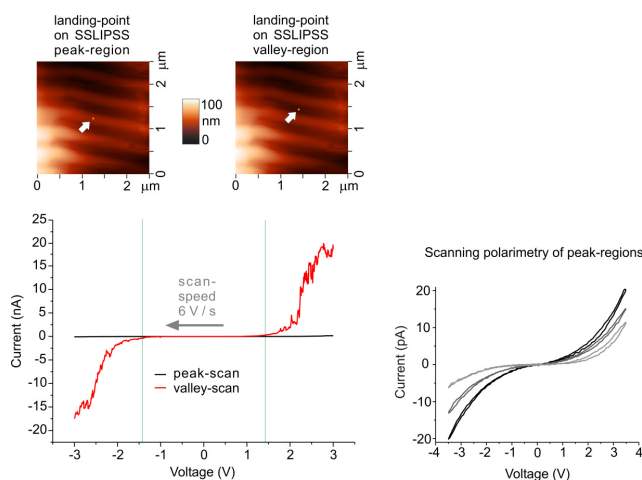

Figure S8. Current voltage curves of peak- and valley-regions
A conductive AFM-tip (diamond-coating) was landed in peak or valley regions of SSLIPSS, respectively; see AFM-pictures. The tip-bias was scanned with 6 V/s from +3 V to -3 V while contacted to peak or valley.

9 Macroscopic electrical properties of SSLIPSS

Linear sweep voltammetry was performed to measure the macroscopic silver reduction on the SSLIPSS electrode. The measurements were carried out in an undivided cell using a potassium nitrate electrolyte solution (0.1 M) containing silver nitrate (1 mg ml^{-1}). The SSLIPSS substrate disk with a diameter of 5 mm was used as working electrode, a glassy carbon disk electrode with a diameter of 3 mm (Metrohm, Swiss) as counter electrode. Both were mounted in a horizontal face-to-face arrangement with an inter-electrode distance of 8 mm. The experiments were performed on an EG&G 273A potentiostat / galvanostat (Princeton Applied Research , USA) at a scan rate of 20 mV s^{-1} with increments of 2 mV.
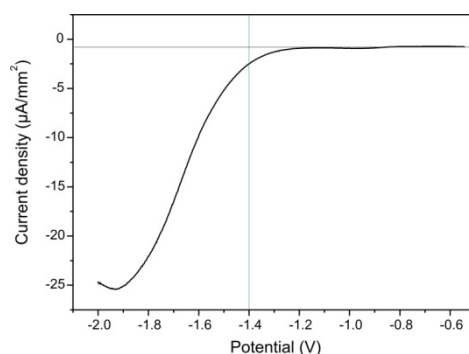
Figure S9. Linear sweep voltammetry of the SSLIPSS-electrode

in 0.1 M KNO$_3$ solution containing 1 mg ml^{-1} AgNO$_3$

The result is in good agreement with the results obtained by conductive atomic force microscopy (CAFM). A macroscopic cathodic current is observed at potentials lower than -1.25 V, which corresponds to the electrochemical breakdown of the oxide layers located in the valley regions of the SSLIPSS-electrode. The current density increases exponentially with the potential up to a peak potential of -1.94 V. After this, the current density decays as a consequence of Ag$^+$-depletion in the interfacial region.

10 Template Processes

Spatial selective growth of carbon nanotubes (CNTs) on SSLIPSS

SSLIPSS samples were placed in a tube furnace and ramped at a rate of 5 °C min^{-1} under 500 sccm forming gas flow (5% H$_2$ / 95% N$_2$). At 800 °C the forming gas flow was reduced to 150 sccm and bubbled through a washing flask containing hexane before entering the oven for 10 minutes. Finally the furnace was cooled at a rate of 10 °C min^{-1} under forming gas flow without hexane admixture.

Spatial selective silver nanoparticle deposition on SSLIPSS and pattern transfer

The deposition was carried out in an undivided cell using a potassium nitrate electrolyte solution (0.1 M) containing silver nitrate (0.1 mg ml^{-1}). All chemicals were of analytical grade and used without further purification. Prior to deposition a thermal treatment of SSLIPSS substrates for 24 h at 300 °C in ambient air was found to be beneficial for the reduction of defects in the ceramic thin-film in order to avoid leakage currents. The SSLIPSS substrate was used as working electrode, a stainless steel mesh of the same size as counter electrode. Both were mounted in a vertical face-to-face arrangement with an inter-electrode distance of 8 mm. Site selective deposition of silver on SSLIPSS-substrates was performed by applying a constant potential of -1.4 V for 150 s at a current density of 1.3 µA mm^{-2}. After electrochemical deposition, the samples were carefully rinsed with deionized water. For the transfer of deposited silver nanoparticle patterns to secondary substrates a PDMS prepolymer solution was prepared from a 10:1 mixture (by weight) of the base and the curing agent (PDMS-Kit, Sylgrad 184) and poured onto the electrochemically treated LIPSS-samples. After curing, PDMS was carefully detracted from the SSLIPSS substrate.

8   Publications

A   Laser-Directed Self-Organization and Reaction Control in Complex Systems - A Facile Synthesis Route for Functional Materials.

Hendrik M. Reinhardt, Clemens Pietzonka, Bernd Harbrecht, Norbert Hampp

submitted

B   Self-Organization of Multifunctional Surfaces - The Fingerprints of Light on a Complex System.

Hendrik M. Reinhardt, Hee-Cheol Kim, Clemens Pietzonka, Julia Krümpelmann, Bernd Harbrecht, Bernhard Roling, Norbert Hampp

Adv. Mater. (25) 3257, **2013.** DOI: 10.1002/adma.201370155

C   Photochemical Preparation of Sub-Wavelength Heterogeneous Laser-Induced Periodic Surface Structures.

Hee-Cheol Kim, Hendrik M. Reinhardt, Pierre Hillebrecht, Norbert Hampp

Adv. Mater. (24) 1994, **2012.** DOI: 10.1002/adma.201200534

D   Transformation of anodic aluminum oxide to nanoporous α-Al$_2$O$_3$, Ruby and Ti-sapphire micropatterns.

Hendrik M. Reinhardt, Hee-Cheol Kim, Norbert A. Hampp

JECS (33) 1281, **2013.** DOI: 10.1016/j.jeurceramsoc.2013.01.005

COMMUNICATION

Photochemical Preparation of Sub-Wavelength Heterogeneous Laser-Induced Periodic Surface Structures

Hee-Cheol Kim, Hendrik Reinhardt, Pierre Hillebrecht, and Norbert A. Hampp*

Intense linearly polarized laser light may induce periodic patterns on the surface of various metals, semiconductors and dielectrics.[1] The periodicity of the patterns depends both on the laser wavelength, and the angle of the incidence to the surface. A vertically incident laser beam leads to a periodic line pattern with a spacing in the range of the wavelength of the light employed. These lines or ripples are generally perpendicular to the polarization of the incident field. Recently, researchers have reported sub-wavelength periodic surface structures,[2] a discovery that gave rise to the differentiation between low spatial frequency (LSFL) and high spatial frequency (HSFL) LIPSS.[2d,3] LSFLs can be obtained by nanosecond-laser pulses whereas HSFLs are exclusively observed in case of ultra-short laser pulses owing to nonlinear optical effects which must be considered during HSFL formation. In spite of extensive research in this field there is no comprehensive theory about LIPSS available to date. However, the classical patterns with a periodicity close to the laser wavelength (LSFL) are commonly accepted as a result of interaction between incident and backscattered surface wavefronts.[4] Besides the numerous efforts to elucidate the origin of LIPSS, this unique self-organizing process has received increasing attention in recent years due to its potential in morphological surface modification.[5] We found that a periodic pattern of light intensity on the surface, which is typical for the LIPSS phenomenon, provides a powerful tool to control photochemical reactions on the surface with high spatial resolution. The linewidth obtained with the method described here reaches beyond earlier holographic and laser ablation approaches.[6] In this paper we report a well defined photochemical reaction, utilizing LIPSS, to fabricate sub-wavelength periodic structures of organometallic hybrid nanowires without altering or damaging the substrate itself. Our system is based on 7-hydroxycoumarin, a photoexcitable molecule, acting as mediator for the photoreduction of silver cations (Ag^+) on the one hand and structure forming precursor for as-generated silver seeds on the other hand. Pulsed laser irradiation into the interface between this reaction mixture and the substrate induces a concentration profile of reactive intermediates. The reduction of metal ion species is directly followed by polymerization of the photosensitizer, resulting in highly ordered LIPSS patterns of metal NPs entrapped in a polymeric insulator. Removal of low molecular weight compounds at elevated temperatures yields sub-wavelengths structures.

In the presented first proof-of-concept experiment anodic aluminum oxide (AAO) was preferred as substrate, even though LIPSS formation could be achieved on polished aluminum blanks as well. The primary advantage of AAO compared to aluminum blanks is improved adhesion of the reaction mixture to the substrate, owing to its well-defined porous nanostructure[7] which in addition allows for accurate detection of laser-induced damages. Considering this, together with the actuality that AAO belongs to the most prominent templates in modern nanotechnology, makes AAO the substrate of choice.

With regard to increased interest in the fabrication of nanostructures, the method introduced here provides a novel way to control photochemical reactions within nanometer spatial resolution. Taking advantage of the fact that photochemical reduction solely depends on the sensitizer,[8] our findings can be transferred to various metals of interest, e.g. gold, copper, platinum and others, just by choice of the matching sensitizer. Furthermore, we believe that this well-defined photochemical event can be used as a model-system to gain deeper insight into mechanisms of LIPSS.

Photochemical generation of metal NPs hand in hand with structure formation is our approach for the generation of organometallic hybrid-LIPSS patterns onto arbitrary substrates. In the first step a photomediator, in this case 7-hydroxycoumarin is excited by absorption of a photon. 7-Hydroxycoumarin shows a broad absorption band at 310–360 nm, which is attributed to the carbonyl group in conjugation with a benzene ring (see **Figure 1**). Excitation of 7-hydroxycoumarin by a 355 nm photon produces a phenoxyl radical[9] which is capable of undergoing electron-transfer reactions with silver cations to form silver NPs, but also triggers polymerization.[10]
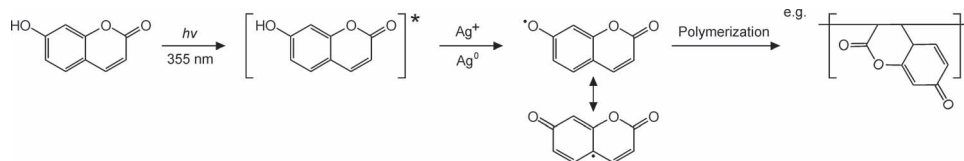
Photoformation of electroactive species from photoexcited 7-hydroxycoumarin, capable to reduce silver cations, was monitored by controlled-potential coulometry (see **Figure 2**, left). During electrolysis at a fixed potential of 0.45 V *vs.* Ag/AgCl reference electrode, the sample solution was irradiated stepwise by 355 nm photons for different time spans. As a reference the same process was measured without laser light exposure. Figure 2 shows that 355 nm laser exposures, indicated by arrows, cause the formation of rather stable electroactive species. Addition of silver cations (Ag^+) after 550 sec and 575 sec induced immediate loss of electroactive species. This demonstrates that electroactive species formed from 7-hydroxycoumarin serve as electron donor for the reduction of silver cations. The population of excited states was found to be proportional to the energy of incident radiation (Figure 2, right).

Photocontrolled formation of silver nanoparticles generated in 7-hydroxycoumarin/Ag^+ solution upon 355 nm irradiation
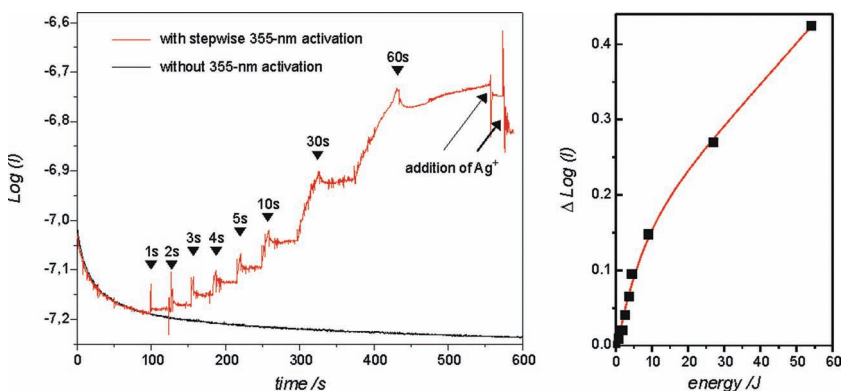
Dr. H.-C. Kim, H. Reinhardt, P. Hillebrecht,
Prof. N. A. Hampp
Department of Chemistry
University of Marburg
35032 Marburg, Germany
E-mail: hampp@staff.uni-marburg.de

Figure 1. Photoreduction of silver cations through photoexcitation of 7-hydroxycoumarin. The elemental silver serves as a nucleus for nanoparticle formation.


Figure 2. Photochemical generation of reductive species from photoexcited 7-hydroxycoumarin. (left) Current response at 0.45 V *vs.* Ag/AgCl carried out in 0.19 M 7-hydroxycoumarin solution with (red) and without (black) photoactivation by 355-nm laser pulses (0.98 W, 3 ns length at 10 kHz repetition rate). (right) Current response depending on the total irradiation time and the total amount of energy applied, respectively.
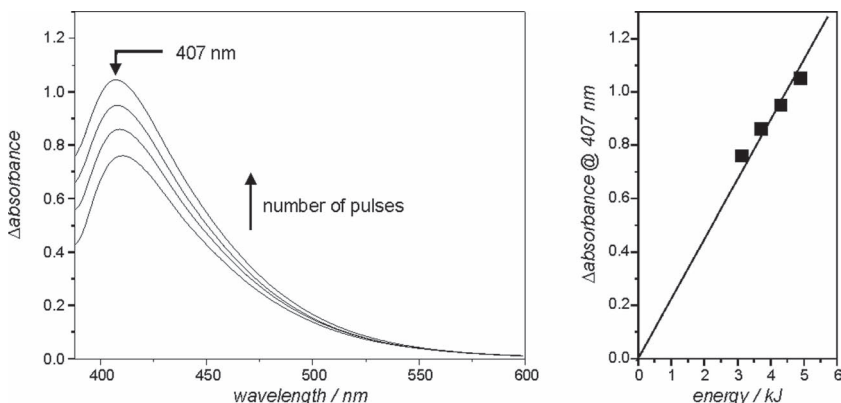
Figure 3. Formation of silver nanoparticles from 7-hydroxycoumarin/Ag$^+$ upon photoexcitation. (left) Time evolution of the UV/Vis absorption spectrum of the 7-hydroxycoumarin/Ag$^+$ solution upon irradiation with 355-nm laser pulses at 98 µJ/pulse. (right) Absorption at 407 nm, which indicates the formation of silver nanoparticles, as a function of energy applied.

When a linearly polarized laser beam of appropriate energy incidences vertically onto a surface, a surface structure with a periodicity in the range of the laser wavelength is formed. It is generally accepted that LIPSS patterns result from inhomogeneous energy deposition due to the interference of the incident beam with a surface scattered field, which leads to a parallel fringe pattern of light intensity perpendicular to the polarization of incident light. The periodicity Λ of the fringe pattern is described by the equation[5a,12] $\Lambda = \lambda \cdot [n \cdot (1 \pm \sin\theta)]^{-1}$, where λ is the wavelength of the light, θ the angle of incidence from normal and n the refractive index of the solid. The principle of our approach to utilize LIPSS as a template for photochemical reactions is illustrated schematically in **Figure 4**. For vertical incidence, we expect a well-ordered periodical line structure of silver NPs having a periodicity smaller than the laser wavelength of 355 nm. The fringe pattern triggers the photosensitized formation of silver NPs. In the areas of high light intensity the generation of Ag^0 seeds occurs and causes the concentration of Ag$^+$ to drop. Diffusion of Ag$^+$ from non-illuminated into illuminated areas further enhances silver nanoparticle growth.

In the experiment we used a solution of silver nitrate (0.19 M) and an equimolar concentration of 7-hydroxycoumarin in a water-acetone-ethanol mixture (2:4:1 v/v/v). AAO substrates were dip-coated in the reactant solution. LIPSS formation was done with 355 nm laser pulses at pulse energies up to

was detected by their distinctive surface plasmon resonance at 407 nm.[11] **Figure 3** shows the evolution of UV/Vis spectra after irradiation by increasing numbers of laser pulses. The amount of silver NPs formed is proportional to the duration of exposure or the energy applied, respectively (Figure 3, right).

Heterogeneous LIPSS formation is one of the potential applications of our photosystem. We want to point out that this new approach does not alter the substrate itself in a morphological way but changes its chemical composition by adding LIPSS onto the substrate's surface. Prior to practical realization a prediction of structures to be expected was conducted from LIPSS-theories. It has to be mentioned that detailed mechanisms of this effect are still under discussion.
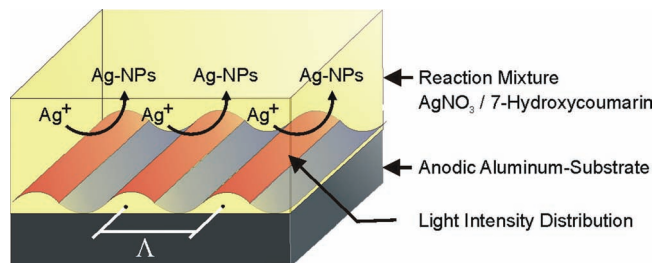
Figure 4. Principle of utilizing LIPSS for photochemically structured silver nanoparticle formation on anodic oxidized aluminium substrates. Ag$^+$ is reduced to Ag^0 in the areas where photochemically excited 7-hydroxycoumarin is produced. The Ag^0 seeds lead to the formation of Ag nanoparticles.
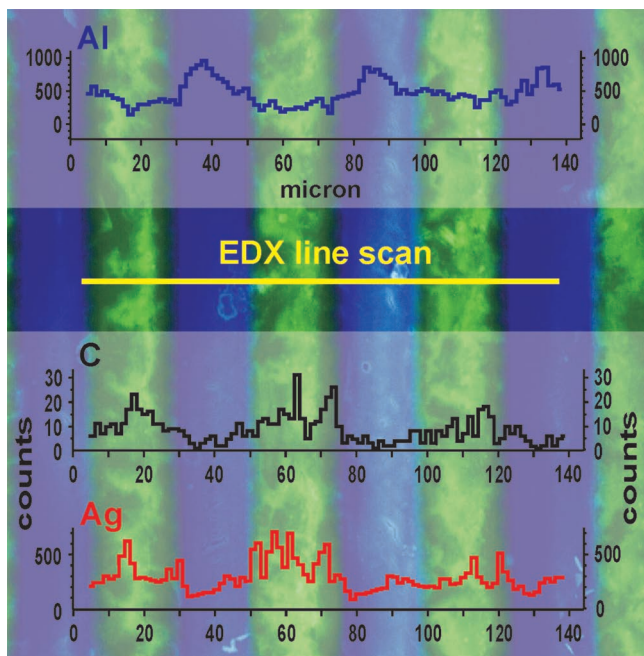
Figure 5. Chemical analysis of the laser induced surface structure. Scanning electron microscopy (SEM) analysis of the silver nanoparticle pattern (green) obtained upon laser exposure of a solution of $AgNO_3$/7-hydroxycoumarin on anodic oxidized aluminium (blue). The EDX spectra were collected along the yellow marked line. Line spacing 40 μm, laser focus 25 μm.

17.2 μJ. EDX analysis confirmed that silver formation occurred exclusively in regions where laser pulses were applied. **Figure 5** shows an EDX line scan across 25 μm wide lines (green) having a spacing of 40 μm prepared by 4.6 μJ laser pulses at 10 kHz repetition and a scan speed of 1 mm/s. Ag and C are only formed in the laser irradiated areas of the AAO surface.

For high resolution morphological analysis by SEM, the dip-coated AAO substrates were irradiated with a pulse energy of 4.6 μJ/pulse at various distances from the focal point to tune the effective intensity. In good agreement with the known characteristics of LIPSS from other studies, we observed three different morphological structures depending on the intensity of the irradiation applied (**Figure 6**). On samples irradiated with low intensities we observed no LIPSS formation. Polydisperse silver NPs were formed at 110 W cm^{-2}, however, without any regularity in spatial distribution (Figure 6, top). The characteristic ripple structure develops from a rather irregular structure to a highly regular one with increasing laser intensities. The lowest energy density observed to be sufficient to develop LIPSS was about 125 W cm^{-2}. Well-ordered periodic structures appeared on the surface of the AAO substrate at 150 W cm^{-2} (Figure 6, middle). As expected, ripples sprawl perpendicular to the direction of laser polarization. The periodicity of the ripples and the ripple width were measured to be about 285 nm and 133 nm, respectively. This is in good agreement with an expected periodicity of 264 nm calculated by the equation given above using the refractive index of water of 1.3426 at 355 nm and vertical incidence of the beam.[13] Illumination intensities considerably higher than the given threshold value for LIPSS-formation involve damage
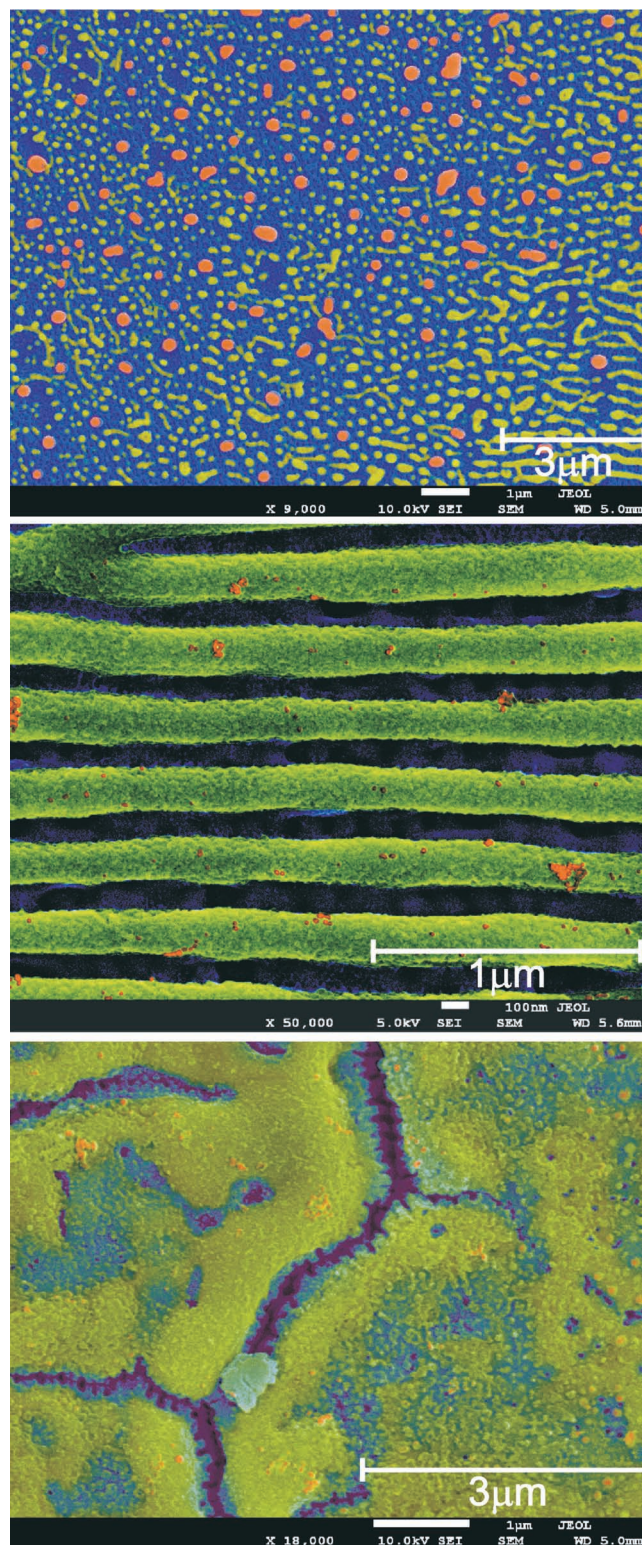
Figure 6. Dependence of LIPSS-induced formation of silver nanoparticle structures on the laser intensity. SEM images of samples treated at different irradiation energies, varied by moving the samples to various distances above the focal point of the lens at a constant pulse energy of 4.6 μJ pulse^{-1}. Top: 110 W cm^{-2}, Middle: 150 W cm^{-2}, Bottom: 245 W cm^{-2}.
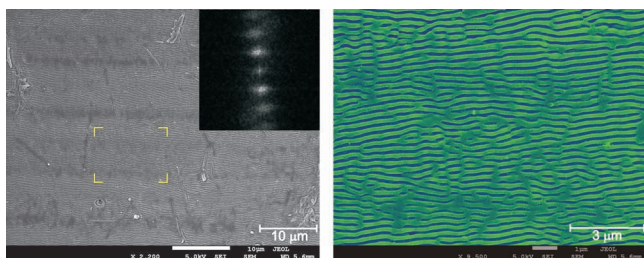
Figure 7. LIPSS surface patterning. (Left) Long-range ordered ripple structure on the substrate. (insert) Fourier transform prepared from full picture. (Right) Magnification of the yellow marked section in the left image.

to the substrate. Crack-lines and surface deviations are the consequence (Figure 6, bottom). In summary formation of LIPSS occurs solely within a narrow range of illumination intensities. Hence, optimization of laser parameters allows for the generation of extended LIPSS areas in high quality (**Figure 7**, left). Fourier analysis (inset) indicates homogeneous line spacing over the total surface. The close-up (Figure 7, right) gives a better impression of the LIPSS-structure.

As mentioned above 7-hydroxycoumarin has a dual function. First it serves as a photomediator to reduce Ag^+ to Ag^0, which leads to Ag nanoparticle formation, and second it photopolymerizes. In combination with the light induced diffusion processes this causes the formation of ripples on the substrate with empty space between. Those ripples are obviously composed of silver nanoparticles (red) embedded in insoluble coumarin-based polymer (green) (**Figure 8**, top-left). Most of the organic matter can be removed by thermal treatment. Figure 8 (top, right) shows an image of a sample after thermal treatment at 250 °C for 45 minutes. Whereas the periodicity remains completely unchanged the ripple width is reduced by a factor of 2 to 3 from 130 nm to approximately 50 nm.

Finally we could confirm the presence of silver NPs and identify their location using backscattered electron imaging
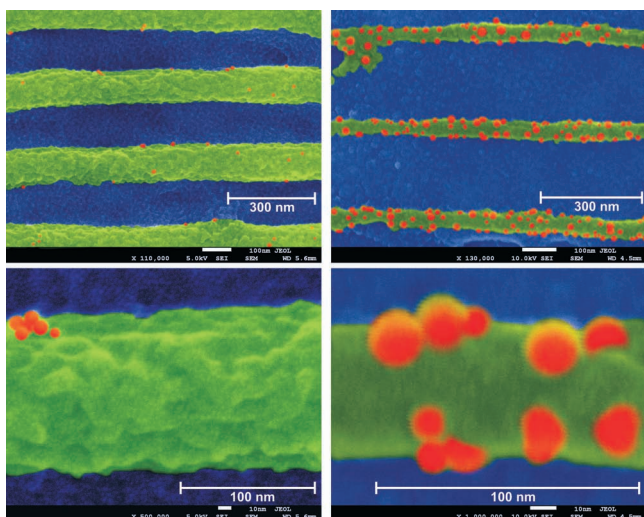
Figure 8. Line-shrinkage by thermal treatment of the LIPSS pattern. (Top left) Ripple structure before thermal treatment. (Bottom left) Close-up of a single line. (Top right) Ripple structure after thermal treatment at 250 °C for 45 min. (Bottom right) Close-up of a single line. The green material is polymer, the red spheres are Ag nanoparticles.
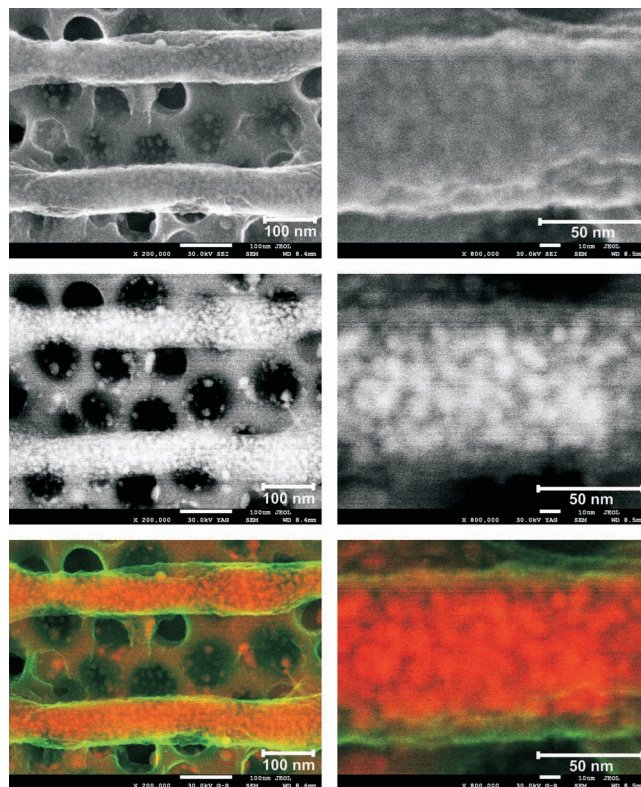
Figure 9. Analysis of the core-shell nanostructure of the lines. (Top) SEM images of the ripple structures. (Center) Backscattering (BSE) images of the very same ripple structures enhancing elements with higher atomic mass. (Bottom) Combined SEM/BSE (SEM = green - polymer, BSE = red - Ag nanoparticles) proving that the Ag nanoparticles are embedded inside the polymeric wires.

(BSE). **Figure 9** shows secondary electron (SE, top row) and BSE images (middle row) of LIPSS-induced ripples at high magnifications. In the combined SE/BSE images silver NPs (red) are clearly shown as bright red spots mainly located inside the fiber-like jacket consisting of organic matter (green). Those hybrid metalorganic LIPSS structures resemble an array of parallel electrical nanowires on an insulator surface (AAO). Macroscopic electrical conductivity measurements resulted in a resistance of about 8 kΩ along the ripple structure with a probehead distance of 1 mm. Resistance of the AAO surface without LIPSS treatment (reference) as well as the resistance perpendicular to the ripple structure was beyond 100 MΩ.

A universal concept to exploit LIPSS-related light intensity patterns for the generation of chemically heterogeneous nanostructures was introduced. Our approach breaks away former limitations of LIPSS by involving photochemistry into its structure formation capability. Free combinations of LIPSS materials with substrate materials of choice become accessible. The potential of this new method was demonstrated using the example of hybrid core-shell-nanowire arrays generated on the surface of anodic aluminum oxide (AAO). For this purpose a non-reversible photomediator was used in a bifunctional way: firstly it serves as photoexcitable reducing agent for silver-nanoparticle generation from an Ag^+-source; secondly it immobilizes as-prepared Ag-NPs on the substrate by cladding those in a wire-like manner. Due to its reliability,

simplicity and flexibility the process is very useful for applications in e.g. optics and electronics, where expensive lithographic techniques are used for the generation of nanostructures so far.

Experimental Section

Chemicals: All chemicals were of the highest commercially available quality and used without further purification.

Formation of silver NPs in bulk solution: Silver nitrate (10 mM) and 7-hydroxycoumarin (10 mM) were dissolved in a mixture of methanol and PVA (0.5 wt-%). Irradiation of the reaction solution (2.0 mL) was done in quartz cuvettes of 10 mm path length by a frequency-tripled Nd:YAG laser operating at 355 nm with 20 ns pulse length (AVIA 355-7000, Coherent, USA). The beam diameter was 5.7 mm and the spatial beam profile was near Gaussian. An average laser power was 0.98 W at a repetition rate of 10 kHz (pulse energy 98 μW) was irradiated into the constantly stirred mixture. Formation of silver NPs was monitored by absorbance measurements using a UV/Vis spectrometer (Lambda 35, Perkin Elmer, USA).

Controlled-potential coulometry: Controlled-potential coulometric experiments were performed using an EG&G model 273A potentiostat/galvanostat. Experiments were done in an undivided cell. A glassy carbon rotating disk electrode rotating at 1000 rpm was used as working electrode (2 mm diameter, Metrohm, Swiss) and a glassy carbon rod served as the counter electrode. The working electrode potential was measured versus a saturated silver/silver chloride reference electrode (Metrohm, Swiss). The electrochemical cell was filled with a 7-hydroxycoumarin water-acetone-ethanol solution (2:4:1 v/v/v) (0.19 M, 3 mL) and tetrabutylammonium tetrafluoroborate (0.2 g) as the supporting electrolyte. Current-time curves were recorded by applying a constant potential of 0.45 V for 10 min. Photoactivation of 7-hydroxycoumarin was accomplished by illuminating the cell from the bottom with the 355 nm laser system described above.

Preparation of anodic aluminum oxide substrates (AAO): Anodic aluminum oxide (AAO) substrates were prepared in a single-step anodization process. Electropolished aluminum sheets (EN AV-5505, 99.9%, 0.55 mm thick) were anodized in a 0.3 M oxalic acid solution at 5 °C at a constant voltage of 60 V for 2 h. After anodization the samples were treated for 40 min in 5% phosphoric acid to widen the pores. Then the samples were rinsed subsequently with deionized water, ethanol and acetone. As-prepared AAO showed an inter pore distance of about 120 nm determined by scanning electron microscopy.

Heat treatment of substrates: Heat treatment of the irradiated samples was carried out in an electronically controlled furnace (C19/S19, Nabertherm, Germany).

Electron microscopy: Field emission scanning electron microscopy (SEM) images and backscattered scanning electron microscopy (BSE) images were taken using a JSM-7500F electron microscope (JEOL, Japan) equipped with a YAG-BSE detector (Autrata, Czech Republic). Energy dispersive X-ray (EDX) analysis was performed using an EDX coupled scanning electron microscope (CamScan-4DV, CamScan, UK).

Resistance measurements: Electrical resistance of the samples was measured using a point probe station (Karl Suss PM5). A Tektronix Type 576 curve tracer was used to measure I-V curves. Tip distance was 1 mm throughout all experiments.

Formation of silver NPs using LIPSS template: Transfer of the reaction mixture onto the AAO samples was carried out by dip-coating for a few seconds. Before irradiation the samples were mounted on a three-axis translation stage (SM 32, OWIS, Germany). In all experiments the stage speed was 1 mm/s and irradiations were performed using the 355 nm Nd:YAG laser described above. The polarized laser beam (s-polarization) was focused onto the sample using a lens with a focal length of 21.9 mm. Irradiation intensity was varied either by optical power control, employing a half wave plate and a Glan laser prism, or by varying the distance between the sample and the focal point. The laser power was measured with a power meter (FieldMax II with an LM-80V detector

head, Coherent, USA). After irradiation the samples were intensely rinsed with ethanol, water and acetone to remove residual agents from the sample surface.

[1] a) M. Brinbaum, *J. Appl. Phys.* **1965**, *36*, 3688–3689; b) J. F. Young, J. S. Preston, H. M. Driel, J. E. Sipe, *Phys. Rev. B* **1983**, *27*, 1155–1172; c) N. R. Isenor, *Appl. Phys. Lett.* **1977**, *31*, 148–150; d) A. K. Jain, V. N. Kulkarni, D. K. Sood, J. S. Uppal, *J. Appl. Phys.* **1981**, *52*, 4882–4886; e) P. E. Dyer, R. J. Farley, *Appl. Phys. Lett.* **1990**, *57*, 756–758; f) S. Lazare, M. Bolle, A. Cros, L. Bellard, *Nucl. Instrum. Meth. B* **1995**, *105*, 159–163.

[2] a) A. M. Ozkan, A. P. Malshe, T. A. Railkar, W. D. Brown, M. D. Shirk, P. A. Molian, *Appl. Phys. Lett.* **1999**, *75*, 3716–3718; b) A. Borowiec, H. K. Haugen, *Appl. Phys. Lett.* **2003**, *82*, 4462–4464; c) L. Ran, Z. Guo, S. Qu, *Appl. Phys. A* **2010**, *100*, 517–521; d) M. Huang, F. Zhao, Y. Cheng, N. Xu, Z. Xu, *Nano* **2009**, *3*, 4062–4070.

[3] J. Z. P. Skolski, G. R. B. E. Römer, A. J. Husis in't Veld, V. S. Mitko, J. V. Obona, V. Ocelik, J. T. M. De Hosson, *J. Laser Micro/Nanoengineering* **2010**, *5*, 263–268.

[4] a) D. C. Emmony, R. P. Howson, L. J. Willis, *Appl. Phys. Lett.* **1973**, *23*, 598–600; b) G. Zhou, P. M. Fauchet, A. E. Siegman, *Phys. Rev. B* **1982**, *26*, 5366–5381; c) J. E. Sipe, J. F. Young, J. S. Preston, H. M. Driel, *Phys. Rev. B* **1983**, *27*, 1141–1154.

[5] a) J. Siegel, P. Slepička, J. Heitz, Z. Kolská, P. Sajdl, V. Švorčik, *Appl. Surf. Sci.* **2010**, *256*, 2205–2209; b) K. Nishioka, S. Horita, *Appl. Phys. A* **2008**, *91*, 235–240; c) J. Eichstädt, G. R. B. E. Römer, A. J. Huis in't Veld, *Phys. Procedia* **2011**, *12*, 7–15; d) A. K. Sharma, J. Smedley, T. Tsang, T. Rao, *Rev. Sci. Instr.* **2011**, *82*, 033113; e) S. Watanabe, Y. Yoshida, S. Kayashima, S. Yatsu, M. Kawai, T. Kato, *J. Appl. Phys.* **2010**, *108*, 103510.

[6] a) L. Balan, C. Turck, O. Soppera, L. Vidal, D. J. Lougnot, *Chem. Mater.* **2009**, *21*, 5711–5718; b) W.-C. Hung, W.-H. Cheng, M.-S. Tsai, W.-C. Chung, I.-M. Jiang, P. Yeh, *J. Appl. Phys. Lett.* **2008**, *93*, 061109.

[7] a) H. Masuda, K. Fukuda, *Science* **1995**, *268*, 1466–1468; b) A. P. Li, F. Müller, A. Birner, K. Nielsch, U. Gösele, *J. Appl. Phys.* **1998**, *84*, 6023–6026.

[8] M. Sakamoto, M. Fujistuka, T. Majima, *J. Photochem. Photobiol. C: Photochem. Rev.* **2009**, *10*, 33–56.

[9] a) Y. Chen, K.-H. Chen, *J. Polym. Sci. Part A: Polym. Chem.* **1997**, *35*, 613–624; b) S. Härtner, H.-C. Kim, N. Hampp, *J. Photochem. Photobiol. A: Chemistry* **2007**, *187*, 242–246.

[10] a) A. Z. Abyshev, S. S. Krylov, *Chem. Nat. Compd.* **1984**, *20*, 35–39; b) Y. Chen, Y.-H. Chen, J. H. Wang, *J. Polym. Research* **1994**, *1*, 295–303.

[11] a) R. P. Bagwe, K. C. Khilar, *Langmuir* **2000**, *16*, 905–910; b) S. Jradi, L. Balan, X. H. Zeng, J. Plain, D. J. Lougnot, P. Royer, R. Bachelot, S. Akil, O. Soppera, L. Vidal, *Nanotechnology* **2010**, *21*, 095605; c) H.-K. Hong, C.-K. Park, M. S. Gong, *Bull. Korean Chem. Soc.* **2010**, *31*, 1252–1256.

[12] a) E. Rebollar, S. Pérez, J. J. Hernandez, I. Martin-Fabiani, D. R. Rueda, T. A. Ezquerra, M. Castillejo, *Langmuir* **2011**, *27*, 5596–5606; b) K. Nishioka, S. Horita, *Appl. Phys. A* **2008**, *91*, 235–240.

[13] G. M. Hale, M. R. Querry, *Appl. Opt.* **1973**, *12*, 555–563.

8   Publications

D   Transformation of anodic aluminum oxide to nanoporous α-Al$_2$O$_3$, Ruby and Ti-sapphire micropatterns.

Hendrik M. Reinhardt, Hee-Cheol Kim, Norbert A. Hampp

This study was not included into the cumulative part because it rather represents a preliminary test that perused the goal of identifying beneficial effects accessible via laser-based material modification. It is concerned with the general possibility to utilize lasers for spatial selective phase transformations in materials. As the example of ferrite precipitation in stainless steel demonstrates (page 33), phase transformation bears the potential to change the properties of materials distinctively. The title of the investigation indicates that phase transformation was performed in anodic aluminum oxide (AAO). This special type of alumina is produced by electrochemical oxidation of aluminum and exhibits a structure of vertically aligned nanopores. Alumina was selected for the investigation because it is a polymorphous material that features interesting properties, which depend largely on its phase. For instance, AAO is an amphoteric and thus easily attacked by aggressive media whereas α-Al$_2$O$_3$ resembles one of the most resistive materials generally known. AAO can be transformed to α-Al$_2$O$_3$ at temperatures exceeding 1000°C, a process that is typically performed via oven sintering. In contrast to this, lasers provide the opportunity for surface selective heating given that irradiated light is efficiently transformed into heat. This can only be achieved for materials that feature a high absorption coefficient in the wavelength range accessible for high power lasers. AAO poses the problem to be practically transparent in a spectral range from near-IR to near-UV, which limits the choice to either unaffordable or low-performance laser types. In order to circumvent this problem, a suitable absorber had to be integrated into AAO. Carbon nanotubes (CNTs) where found to be a good solution for this problem. CNTs can be grown in AAO catalytically and allow for photothermal heating above phase transition temperature. Most importantly, CNTs resemble a sacrificial absorber since they are thermally decomposed in the photothermal process thus leaving a phase-transformed material free of contaminants. In addition to that, the special thermal properties of integrated CNT/AAO composites were found to be advantageous

because laser-induced heat is constrained to very small volumes. This enables for phase transformations with high lateral resolution, an aspect that was exploited for the generation of optically active micropatterns comprising α-Al$_2$O$_3$-based materials like ruby and Ti-sapphire.

Transformation of anodic aluminum oxide to nanoporous α-Al₂O₃, ruby and Ti-sapphire micropatterns

Hendrik M. Reinhardt [a], Hee-Cheol Kim [a], Norbert A. Hampp [a,b,*]

[a] *Department of Chemistry, Philipps-University of Marburg, Hans-Meerwein-Str., D-35032 Marburg, Germany*
[b] *Materials Science Center, D-35032 Marburg, Germany*

Abstract

Anodic aluminum oxide (AAO) stands in the forefront of the most important materials in modern nanotechnology. Its regular nanoporous structure is widely used for template assisted nanopatterning, optical applications, membrane science and plenty more. Our study presents an enhancement on the potential application of AAO by exploiting its inherent nature of polymorphism. Amorphous AAO is selectively transformed to α-Al₂O₃ by a laser-induced photo-thermal process. Carbon nanotubes (CNT) are employed as a sacrificial laser light absorber to accomplish the phase transformation of AAO to α-Al₂O₃. Doping of the evolving α-Al₂O₃ with Cr or Ti enables preparation of free designable photoluminescent surface patterns. The superior properties of α-Al₂O₃ are utilized to create hierarchically structured systems for optical, biomedical and lithographic applications.

1. Introduction

Originally developed as a surface protective coating for aluminum products, anodic aluminum oxide (AAO) matured to an indispensable cross sectional technology. Its key benefits are great design flexibility combined with simple and cost efficient fabrication. The wide variety of applications facilitated by AAO is hard to summarize, moreover new fields are rapidly emerging. High-tech applications have been demonstrated in fields of nanostructure generation,[1–4] energy storage,[5] photovoltaics,[6,7] chemical sensors,[8,9] magnetic data storage,[3] photonics,[10,11] biology[12] and so forth. Large scale highly ordered hexagonal pore arrays,[13] advanced pore size control,[14] modified pore shapes,[15,16] high aspect ratio templates[17] and laser micro-machining of AAO[18,19] are some of the latest achievements. Efforts in this field are focused on morphological improvements of AAO in order to create next generation templates. In contrast, studies concerning modifications of AAO's crystal structural are rare, even though alumina provides diverse crystalline phases. Seven polymorphs of alumina are known, including α, γ, δ, η, θ, κ and χ[20] offering a pool of substantial differences in chemical and physical properties, which might be advantageous for AAO modifications. Actually there are a few studies concerning phase transition reactions of AAO. In the early 70s Sirota and Shokhina described polymorphous transformations of AAO subjected to isothermal treatment at temperatures up to 1200 °C.[21] Later studies by Lee focused on increased chemical stability of AAO transformed to δ- and θ-phase by isothermal treatment at 900 °C.[22] Current studies by Fernández-Romero, Choudhari, Marsal and McQuaig proofed that AAO can be converted to α-Al₂O₃ phase under maintenance of the nanoporous morphology.[23–26] All those studies have in common to employ oven tempering processes for phase transformations of AAO. However, ovens are limited to homogeneous heat treatment, thus subjecting the entire substrate to the same condition. This will do for some applications but the method is unfeasible when heterogeneous features like distinct patterns are required.

We now introduce a laser-based process enabling spatially selective phase transformation of AAO to α-Al₂O₃. During this process the α-Al₂O₃ may be doped with, e.g., Ti or Cr to receive free designable photoluminescent surface structures.

* Corresponding author at: Department of Chemistry, Philipps-University of Marburg, Hans-Meerwein-Str., D-35032 Marburg, Germany. Tel.: +49 6421 28 25775; fax: +49 6421 28 25798.
E-mail address: hampp@staff.uni-marburg.de (N.A. Hampp).

Lasers seem to be an obvious choice for this task, but were never employed for this purpose before. The reason is that AAO is nearly transparent for common laser wavelengths. As a result effective photo-thermal heating of AAO is impossible due to low absorption even for high intensity irradiation. We solved this problem by equipping AAO with carbon nanotubes (CNT) as a sacrificial absorber that enables laser-induced phase transformation of AAO to α-Al_2O_3 with cutting edge precision.

2. Experimental

Fabrication of AAO/CNT. High purity aluminum foil (Good-Fellow Al 99.999) was degreased in 5 wt% sodium hydroxide at 60 °C for 1 min, rinsed with deionized water, pickled in 1:1 nitric acid/water and finally rinsed with deionized water. AAO-membranes examined by X-ray powder diffraction (XPD) and irradiation intensity studies were anodized in 10 vol% sulfuric acid solution at 4 °C with 35 V.[27] AAOs for dotwise patterning were anodized in 0.3 M oxalic acid solution at 3 °C with 100 V.[17] Remaining Al was removed by etching in cupric chloride/hydrochloric acid solution. As prepared AAO samples were rinsed with deionized water and dried at 50 °C for several days.

AAO-template assisted CNT growth was conducted by a thermal CVD process using conditions described by Yang.[28] Briefly, AAO samples were placed in a tube furnace and ramped at a rate of 5°/min in a reducing environment comprising 25% H_2 and 75% N_2. At 750 °C the samples were subjected to a gas mixture of H_2/C_2H_2 at flow rates of 500 sccm and 150 sccm for 2 h. Finally the furnace was cooled at a rate of 5°/min under Ar-flow.

Details concerning fabrication and handling of AAO/CNT membranes are supplied in the Supplementary Information.

Chromium doped α-Al_2O_3 was prepared by immersion of AAO/CNT in an aqueous solution of 1 M $Cr(III)NO_3$ for 1 h prior to irradiation. Titanium doping was achieved by immersion in a solution containing 12% $Ti(III)Cl_3$ in 8% hydrochloric acid (Sigma–Aldrich) for 10 min. After draining and drying the substrates were irradiated to produce micropatterns of Al_2O_3:Cr and Al_2O_3:Ti, respectively. Finally the substrates were purged in distilled water to remove metal salts from unaffected areas.

Laser irradiation of AAO/CNT. A Newport Explorer XP 532-5 DPSS laser emitting TEM_{00} ($M^2 < 1.1$) at a wavelength of 532 nm was used for photo-thermal treatment of AAO/CNT samples. The laser beam was steered over the samples by a SCANgine14 galvanometer scanner equipped with a Rodenstock Ronar F-Theta 100 mm lens. Large scale irradiation for XPD sample preparation was conducted at 3.6 W at a repetition rate of 300 kHz. Doped and pure α-Al_2O_3 dot patterns were generated at 100 mW and 300 kHz repetition rate. Dwelling times used per dot ranged from 1 to 100 ms, depending on the desired dot size.

XPD measurements were carried out on a Philips X-Pert MPD Pro powder diffractometer equipped with X-Pert tube Co LFF operating at 30 kV and 30 mA. Spectra were obtained in the range of $25° \leq 2\theta \leq 85°$ at room temperature. Data analysis and postprocessing was conducted by X-Pert High Score Plus v2.2c.

Fluorescence microscopy of micro structured samples was performed on a Carl Zeiss LSM 5 Pascal under mercury lamp illumination applying fluorescence filter F-Set25.

Topological mapping of substrate surfaces was performed with the same microscope operating in laser-scanning mode (LSM).

Photoluminescence emission of Al_2O_3:Cr and Al_2O_3:Ti were exited by cw-laser irradiation at 532 nm and measured by an OceanOptics USB2000 fiber spectrometer.

Scanning electron microscopy (SEM) was performed on a Jeol JSM 7500F field emission microscope equipped with SEI, LEI and BSE multisensor-matrix.

3. Results and discussion

Like most non-metals, alumina ceramics can be heated by infrared lasers due to resonant phonon coupling. Unfortunately typical IR-sources like CO_2-lasers give poor spatial resolution attributed to their long wavelength of 10.6 μm which is unfavorable for micropatterning regarding the Abbe diffraction limit. Likewise, the attempt to use shorter wavelengths for photo-thermal heating encounters other problems: alumina ceramics are transparent in the spectral range from near-IR to near-UV; band gaps are solely located in the vacuum-UV.[29] In short, laser wavelengths covered by available high power lasers are not absorbed and high power lasers in the vacuum ultraviolet spectral range are barely available. Accepting the fact that this problem cannot be solved by an appropriate choice of laser wavelength the alternative is to change the substrate absorption characteristics. Several modifications increasing the optical density of AAO were tested: Organic dyes soaked into the nanopores of AAO gave good optical absorption but laser irradiation experiments showed that phase transition of AAO to α-Al_2O_3 is not possible because organic molecules decompose before transition temperature is reached. An obvious solution for this problem is the use of inorganic absorbers, which indeed enabled for effective photo-thermal heating. Naturally, this approach results in absorber contaminated α-Al_2O_3 which is undesired because the physicochemical properties of α-Al_2O_3 are very sensitive to contamination. Finally we took advantage of the catalytic capability of AAO to grow carbon nanotubes in its nanopores[30] (see Supplementary Information for details). CNTs feature higher temperature stability than organic dyes and superior optical density. We found that photo-thermal heating of such AAO/CNT substrates readily induces surface temperatures allowing for phase evolution of α-Al_2O_3. XPD spectra of AAO/CNT samples irradiated at a laser wavelength of 532 nm are illustrated in Fig. 1 together with blank aluminum, anodized aluminum and non-irradiated AAO/CNT for comparative purposes.

AAO and AAO/CNT samples can be considered amorphous apart from peaks ascribable to metallic aluminum, denoted by gray miller indices. Laser treatment of AAO/CNT with an irradiation intensity of 100 J/cm^2 turns small amounts of initially amorphous alumina into γ-Al_2O_3. McQuaig and Kirchner observed this transition to occur between 900 and 970 °C by oven sintering of anodic alumina membranes.[26,31] The threshold irradiation intensity for α-Al_2O_3 generation was found at
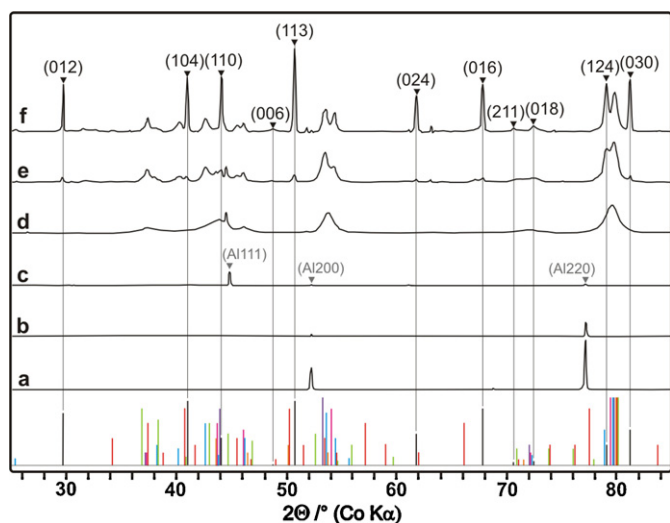
Fig. 1. Photo-thermal phase evolution from AAO/CNT. Aluminum blank (a), AAO (b), AAO/CNT (c), AAO/CNT irradiated with 100 J/cm^2 (d), AAO/CNT irradiated with 350 J/cm^2 (e), and AAO/CNT irradiated with 700 J/cm^2 (f). Characteristic intensities of transition alumina phases are given at the bottom: ICDD card 43-1484 – α-Al$_2$O$_3$ (black), ICDD card 29-1486 – γ-Al$_2$O$_3$ (purple), ICDD card 16-0394 – δ-Al$_2$O$_3$ (blue), ICDD card 21-0010 – η-Al$_2$O$_3$ (pink), ICDD card 35-0121 – θ-Al$_2$O$_3$ (green), ICDD card 04-0878 – κ-Al$_2$O$_3$ (red), ICDD card 34-0493 – χ-Al$_2$O$_3$ (orange). (For interpretation of the references to color in this figure legend, the reader is referred to the web version of the article.)

350 J/cm^2 even though the preferred α-phase represents just a minor amount of the mixed crystalline alumina polymorphs. This changes radically when AAO/CNT is irradiated at an intensity of 700 J/cm^2. Distinct α-Al$_2$O$_3$ peaks, denoted by black miller indices, tower above all other alumina polymorphs. However, pure α-Al$_2$O$_3$ could not be achieved by higher irradiation intensities due to laser induced substrate damage. This results from the fact that the AAO/CNT to α-Al$_2$O$_3$ transition is thermo-dynamically favored for temperatures by far exceeding the thermal stability of CNTs in oxidizing environments.[32,33] Consequently, CNTs act as a sacrificial absorber, which is pyrolyzed during the photo-thermal process (see Supplementary Information for details). On the one hand the rate of absorber degradation is a function of temperature on the other hand temperature depends on irradiation intensity and absorber activity. Evidently a break-even point is present in the system which limits the maximum temperature available for phase transition and thus the yield of α-Al$_2$O$_3$. In order to locate this point we conducted a series of irradiations covering the intensity range from 400 to 700 J/cm^2. Results are illustrated in Fig. 2.

Irradiation at 400 J/cm^2 left the surface unaffected from a morphological point of view – nanopores are still present. 500 J/cm^2 changed the surface to a cindery morphology, indicating that the melting point of alumina was exceeded. Samples irradiated at 600 J/cm^2 show micrometer sized alumina grains fused to a mosaic-pattern. At 700 J/cm^2 the mosaic-like morphology is fragmented. In conclusion it can be stated, that AAO-embedded CNTs show good absorber activity for irradiation intensities up to 600 J/cm^2. Further increase in intensity causes absorber degradation and thus deeper penetration of photons into the AAO-matrix. Photo-thermal heating of deeper regions induces mechanical stress resulting in surface wrinkling and rupture. The potential to create specific surface morphologies by variation of irradiation intensity may be interesting
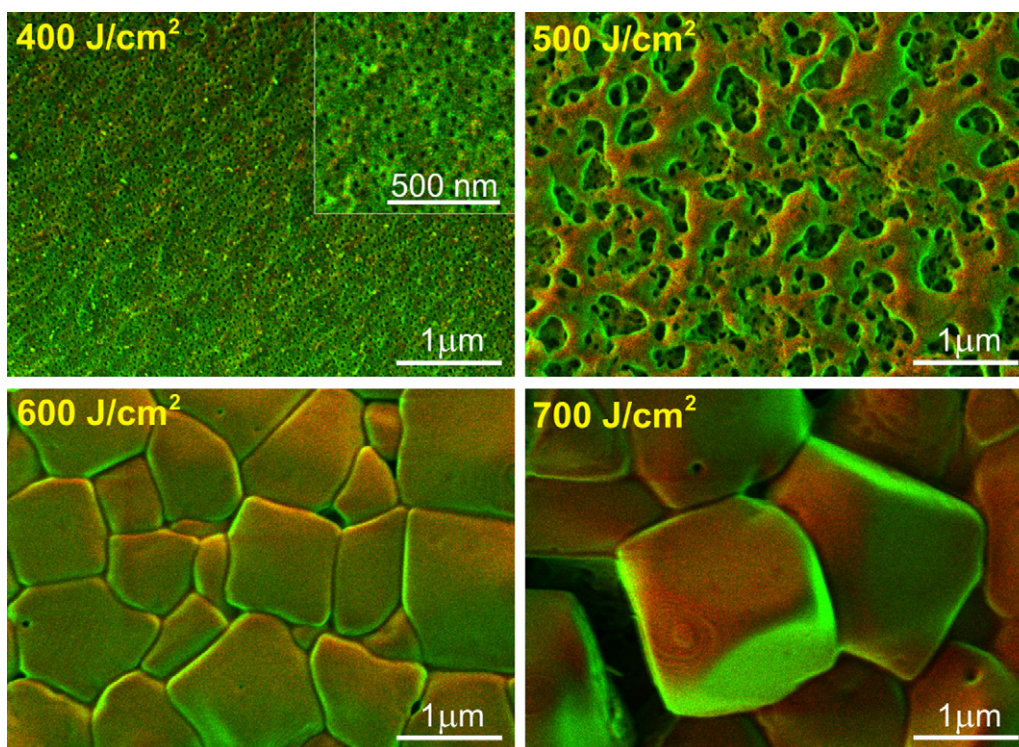

Fig. 2. Morphological effects of photo-thermal treatment. Dual-sensor SEM inspection (SEI + LEI) of AAO/CNT after photo-thermal processing. Irradiation intensities are denoted in yellow. (For interpretation of the references to color in this figure legend, the reader is referred to the web version of the article.)
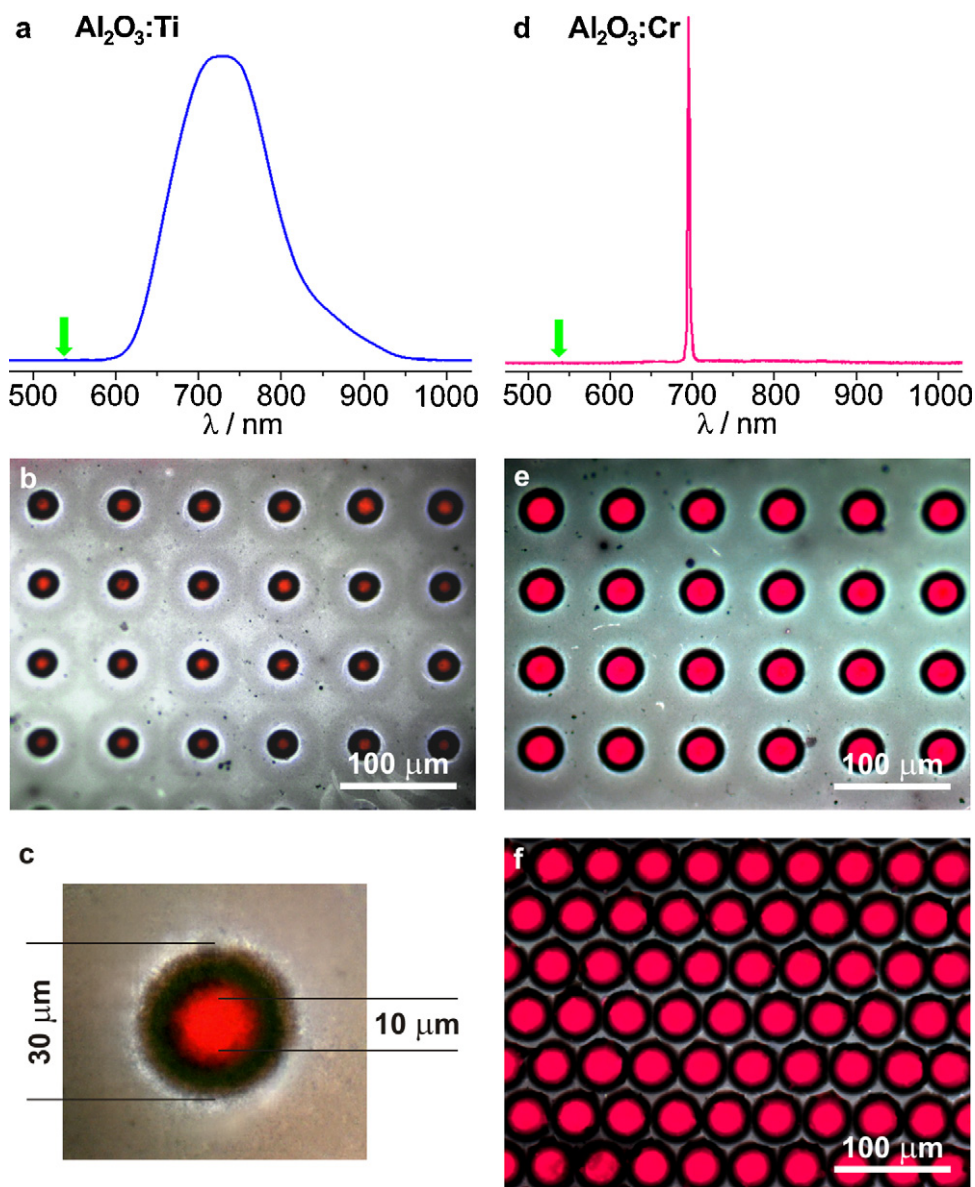
Fig. 3. Microstructure performance of photo-thermal phase transition to α-Al$_2$O$_3$. Photoluminescence spectra and micro-patterns of Al$_2$O$_3$: Ti (a–c), photoluminescence spectra and micropatterns of Al$_2$O$_3$:Cr (d–f), green arrows indicate cw-laser excitation at 532 nm wavelength. (For interpretation of the references to color in this figure legend, the reader is referred to the web version of the article.)

for, e.g., biomedical applications. However, our objective is structural transformation of AAO ideally without changing the nanoporous morphology; hence we kept irradiation intensities below 500 J/cm^2 for our studies.

α-Al$_2$O$_3$ is the host crystal for gemstones like ruby. The replacement of a few Al^{3+}-ions by Cr^{3+}-ions involves a rigorous change of its optical properties. Li et al. reported strong photoluminescence from Cr^{3+}-doped AAO after thermal transformation to α-Al$_2$O$_3$.[34] We introduced this feature to our process by soaking Cr^{3+}-ions into the nanoporous structure of AAO/CNT prior to photo-thermal treatment. After transformation to α-Al$_2$O$_3$ those samples show a sharp photoluminescence peak at 694.2 nm as shown in Fig. 3, the R1-line of Ruby.[35] Repeating the same experiment with Ti^{3+}-doping resulted in a broad photoluminescence emission band from 600 to 950 nm with

a maximum intensity at 730 nm, which is in agreement with spectra of Al$_2$O$_3$:Ti-laser-crystals.[36,37]

The photo-thermal heating of AAO/CNT proofed to be highly effective for the generation of metal-ion doped α-Al$_2$O$_3$. The photoluminescence of Al$_2$O$_3$:Cr and Al$_2$O$_3$:Ti presents also a convenient solution for microstructure inspection. Owing to high photoluminescence efficiency laser excitation is actually not necessary; instead we used fluorescence microscopy for microstructure imaging. Microdot arrays of Al$_2$O$_3$:Cr and Al$_2$O$_3$:Ti, shown in Fig. 3, demonstrate that AAO/CNT to α-Al$_2$O$_3$ transformation can be achieved with cutting-edge precision. SEM inspection of the black rings surrounding the fluorescent spots resulted in the finding that CNTs were pyrolized in this region. This heat affected rims expand about 10 μm from the fluorescent edge which is comparatively low considering the
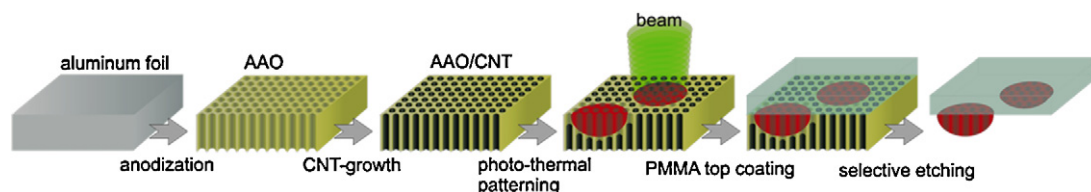
Fig. 4. Schematic representation of pattern transfer process using selective etching.
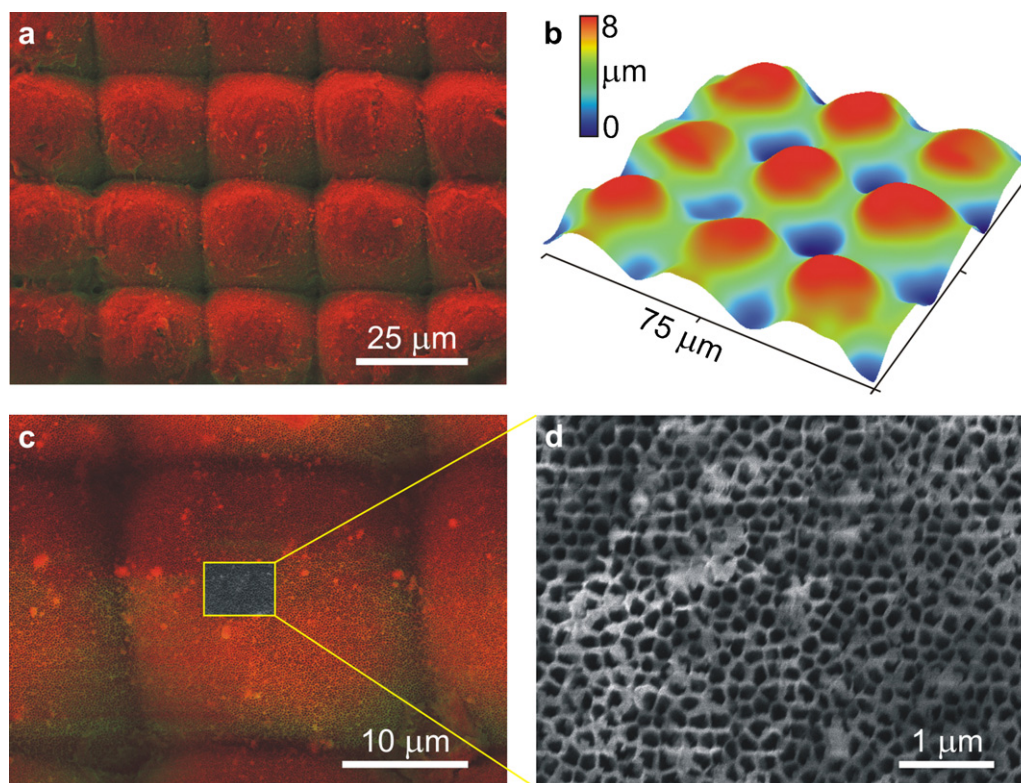

Fig. 5. Depth effect of photo-thermal α-Al$_2$O$_3$ evolution. SEM-inspection of α-Al$_2$O$_3$-micropattern obtained by pointwise heating of AAO/CNT with 25 µm dot-spacing (a, c, and d). Topographic illustration of α-Al$_2$O$_3$-micropattern by laser-scanning-microscopy (b).

high thermal gradient. On the one hand the tight confinement of photo-thermally induced heat can be explained by means of low thermal conductivity of AAO owing to its nanoporous morphology.[38,39] On the other hand it must be noticed that CNTs feature extraordinarily high thermal conductivity.[40] We assume the very combination of alumina nanopores and CNTs to be beneficial for closely localized heat confinement. Transversal heat diffusion in AAO/CNT is suppressed by the coaxial arrangement of alumina nanopores, acting as heat-diffusion barrier, and CNTs, acting as cooling pipes, which rapidly spread diffused heat in longitudinal direction. Additional to that, the simultaneous decomposition of CNTs is an energy consuming process, thus favoring heat confinement as well.[41]

Superficial conversion of AAO to α-Al$_2$O$_3$ by photo-thermal treatment was demonstrated so far. In the following section we give insights in structure formation below the surface. The sketch illustrated in Fig. 4 summarizes the entire process applied for this investigation.

In contrast to AAO, which is an amphotheric oxide, α-Al$_2$O$_3$ can neither be etched by acids nor by bases. This advanced chemical stability was utilized for selective etching of photothermally patterned AAO/CNT. α-Al$_2$O$_3$ micropatterns were fixed by a PMMA top coating prior to AAO-dissolution in aqueous NaOH-solution.

CNTs were removed by ultrasonication in an aqueous solution of sodium dodecylbenzene sulfonate followed by rinsing with distilled water.[42] SEM pictures of the residual α-Al$_2$O$_3$ micropatterns on PMMA are shown in Fig. 5. The distinct regular morphology of α-Al$_2$O$_3$-micropatterns demonstrates that photothermal transformation of AAO to α-Al$_2$O$_3$ provides very sharp depth resolution. Pointwise laser-heating in close proximity produced interconnected humps with 8 µm peak-to-valley height. Moreover the nanoporous morphology of AAO is maintained as a substructure in these micro-humps.

4. Conclusion

Laser controlled photo-thermal phase transformation of AAO/CNT is an efficient method for the generation of hierarchically structured α-Al$_2$O$_3$ patterns. CNTs feature perfect

absorber performance enabling the AAO to α-Al$_2$O$_3$ transformation under maintenance of the nanoporous AAO structure. CNTs act as sacrificial absorbers providing α-Al$_2$O$_3$ free of contaminants. This is absolutely mandatory to enable specific α-Al$_2$O$_3$-doping by soaking e.g., Cr or Ti ions into the AAO/CNT precursor and receiving the characteristic ruby- and Ti-sapphire photoluminescence emissions. Potential applications for the presented systems encompass e.g., fluorescent imaging in biomedical arrays, microlasers, microlens-arrays and many more.

Acknowledgment

Appendix A. Supplementary data

Supplementary data associated with this article can be found, in the online version, at http://dx.doi.org/10.1016/j.jeurceramsoc.2013.01.005.

References

1. Masuda H, Fukuda K. Ordered metal nanohole arrays made by a two-step replication of honeycomb structures of anodic alumina. *Science* 1995;**268**:1466–8.

2. Masuda H, Yasui K, Nishio K. Fabrication of ordered arrays of multiple nanodots using anodic porous alumina as an evaporation mask. *Adv Mater* 2000;**12**:1031–3.

3. Gao X, Liu L, Birajdar B, Ziese M, Lee W, Alexe M, Hesse D. High-density periodically ordered magnetic cobalt ferrite nanodot arrays by template-assisted pulsed laser deposition. *Adv Funct Mater* 2009;**19**:3450–5.

4. Wu M, Wen L, Lei Y, Ostendorp S, Chen K, Wilde G. Ultrathin alumina membranes for surface nanopatterning in fabricating quantum-sized nanodots. *Small* 2010;**6**:695–9.

5. Banerjee P, Perez I, Henn-Lecordier L, Lee LB, Rubloff GW. Nanotubular metal–insulator–metal capacitor arrays for energy storage. *Nat Nanotechnol* 2009;**4**:292–6.

6. Fan Z, Razavi H, Do J, Moriwaki A, Ergen O, Chueh Y, Leu PW, Ho JC, Takahashi T, Reichertz LA, Neale S, Yu K, Wu M, Ager JW, Javey A. Three-dimensional nanopillar-array photovoltaics on low-cost and flexible substrates. *Nat Mater* 2009;**8**:648–53.

7. Haberkorn N, Gutmann JS, Theato P. Template-assisted fabrication of free-standing nanorod arrays of a hole-conducting cross-linked triphenylamine derivative: toward ordered bulk-heterojunction solar cells. *ACS Nano* 2009;**3**:1415–22.

8. Moreno i Codinachs L, Birkenstock C, Garma T, Zierold R, Bachmann J, Nielsch K, Schöning MJ, Fontcuberta i Morral A. A micron-sized nanoporous multifunction sensing device. *Phys Stat Sol* 2009;**206**:435–41.

9. Guo D, Fan L, Wang F, Huang S, Zou X. Porous anodic aluminum oxide Bragg stacks as chemical sensors. *J Phys Chem C* 2008;**46**:17952–6.

10. O'Carroll DM, Hofmann CE, Atwater HA. Conjugated polymer/metal nanowire heterostructure plasmonic antennas. *Adv Mater* 2010;**22**:1223–7.

11. Masuda H, Yamada M, Matsumoto F, Yokoyama S, Mashiko S, Nakao M, Nishio K. Lasing from two-dimensional photonic crystals using anodic porous alumina. *Adv Mater* 2006;**18**:213–6.

12. Chen W, Jin B, Hu Y, Lu Y, Xia X. Entrapment of protein in nanotubes formed by a nanochannel and ion-channel hybrid structure of anodic alumina. *Small* 2012;**8**:1001–5.

13. Matsui Y, Nishio K, Masuda H. Highly ordered anodic porous alumina with 13-nm hole intervals using a 2D array of monodisperse nanoparticles as a template. *Small* 2006;**2**:522–5.

14. Chen W, Wu J, Xia X. Porous anodic alumina with continuously manipulated pore/cell size. *ACS Nano* 2008;**2**:959–65.

15. Krishnan R, Thompson CV. Monodomain high-aspect-ratio 2D and 3D ordered porous alumina structures with independently controlled pore spacing and diameter. *Adv Mater* 2007;**19**:988–92.

16. Masuda H, Asoh H, Watanabe M, Nishio K, Nakao M, Tamamur T. *Adv Mater* 2001;**13**:189–92.

17. Lee W, Ji R, Gösele U, Nielsch K. Fast fabrication of long-range ordered porous alumina membranes by hard anodization. *Nat Mater* 2006;**5**:741–7.

18. Jha H, Kikuchi T, Sakairi M, Takahashi H. Laser micromachining of porous anodic alumina film. *Appl Phys A* 2007;**88**:617–22.

19. Jha H, Kikuchi T, Sakairi M, Takahashi H. Micro-patterning in anodic oxide film on aluminium by laser irradiation. *Electrochim Acta* 2007;**52**:4724–33.

20. Stumpf HC, Russell AS, Newsome JW, Tucker CM. Thermal transformations of aluminas and alumina hydrates – reaction with 44% technical acid. *Ind Eng Chem* 1950;**42**:1398–403.

21. Sirota NN, Shokhina GN. Kinetics of polymorphous transformation of anodic alumina. *Krist Techn* 1974;**9**:913–9.

22. Lee C, Kang H, Chang Y, Hahm Y. Thermotreatment and chemical resistance of porous alumina membrane prepared by anodic oxidation. *Korean J Chem Eng* 2000;**17**:266–72.

23. Fernández-Romero L, Montero-Moreno JM, Pellicer E, Peiró F, Cornet A, Morante JR, Sarret M, Müller C. Assessment of the thermal stability of anodic alumina membranes at high temperatures. *Mater Chem Phys* 2008;**111**:542–7.

24. Choudhari KS, Sudheendra P, Udayashankar NK. Fabrication and high-temperature structural characterization study of porous anodic alumina membranes. *J Porous Mater* 2012, http://dx.doi.org/10.1007/s10934-012-9568-z.

25. Marsal LF, Vojkuvka L, Formentin P, Pallarés J, Ferré-Borrull J. Fabrication and optical characterization of nanoporous alumina films annealed at different temperatures. *Opt Mater* 2009;**31**:860–4.

26. McQuaig MK, Toro A, Van Geertruyden W, Misiolek WZ. The effect of high temperature heat treatment on the structure and properties of anodic aluminum oxide. *J Mater Sci* 2011;**46**:243–53.

27. Chu S, Wada K, Inoue S, Isogai M, Yasumori A. Fabrication of ideally ordered nanoporous alumina films and integrated alumina nanotubule arrays by high-field anodization. *Adv Mater* 2005;**17**:2115–9.

28. Yang C, Chen C, Shieh J. Characterization and field-emission properties of carbon nanotube arrays in nanoporous alumina template and on blank Si substrate. *J Appl Phys* 2006;**100**:104302.

29. French RH, Müllejans H, Jones DJ. Optical properties of aluminum oxide: determined from vacuum ultraviolet and electron energy-loss spectroscopies. *J Am Ceram Soc* 1998;**81**:2549–57.

30. Kyotani T, Tsai L, Tomita A. Formation of ultrafine carbon tubes by using an anodic aluminum-oxide film as a template. *Chem Mater* 1995;**7**:1427–8.

31. Kirchner A, MacKenzie KJD, Brown IWM, Kemmitt T, Bowden ME. Structural characterisation of heat-treated anodic alumina membranes prepared using a simplified fabrication process. *J Membr Sci* 2007;**287**:264–70.

32. Liew KM, Wong CH, He XQ, Tan MJ. Thermal stability of single and multi-walled carbon nanotubes. *Phys Rev B* 2005;**71**:075424.

33. Thostenson ET, Li C, Chou T. Nanocomposites in context. *Compos Sci Technol* 2005;**65**:491–516.

34. Li T, Yang S, Huang L, Zhang J, Gu B, Du Y. Strong photoluminescence from Cr^{3+} doped porous anodic alumina. *J Phys: Condens Matter* 2004;**16**:2463–9.

35. Maiman TH. Stimulated optical radiation in ruby. *Nature* 1960;**187**:493–4.

36. Moulton PF. Ti-doped sapphire: tunable solid-state laser. *Opt News* 1982;**8**:9–13.

37. Moulton PF. Spectroscopic and laser characteristics of Ti:Al$_2$O$_3$. *Opt Soc Am B* 1986;**3**:125–33.

38. Borca-Tasciuc DA, Chen GJ. Anisotropic thermal properties of nanochanneled alumina templates. *Appl Phys* 2005;**97**:084303.

39. Cai A, Yang L, Chen J, Xi T, Xin S, Wu W. Thermal conductivity of anodic alumina film at (220 to 480) K by laser flash technique. *J Chem Eng Data* 2010;**55**:4840–3.

40. Kim P, Shi L, Majumdar A, Mc Euen PL. Thermal transport measurement of individual multiwalled nanotubes. *Phys Rev Lett* 2001;**87**: 215502.

41. Chang C, Tseng J, Horng J, Shu C. Thermal decomposition of carbon nanotube/Al_2O_3 powders by DSC testing. *Compos Sci Technol* 2008;**68**:2954–9.

42. Islam MF, Rojas E, Bergey DM, Johnson AT, Yodh AG. High weight fraction surfactant solubilization of single-wall carbon nanotubes in water. *Nano Lett* 2003;**3**:269–73.

Wissenschaftlicher Werdegang

Oktober 2002   Immatrikulation an der Philipps-Universität Marburg, Studiengang Chemie

Oktober 2007   Diplom in Chemie – Abschlussnote 1,4
Titel der Diplomarbeit:
„Lasergestützte Colorierung von Edelstahl"

2008 – 2013   Promotion in physikalischer Chemie/Biophysik
Titel der Doktorarbeit:
"Laser-directed Self-Organization and Reaction Control in Complex Systems"